Properties of Excited Hadrons from Lattice QCD

Dissertation

zur Erlangung des akademischen Grades
Doktor der Naturwissenschaften.

Angefertigt am Institut für Physik,
Karl-Franzens-Universität Graz.

Eingereicht von:
Daniel Mohler

Betreuung:
Prof. Dr. C. Gattringer

Präambel

Ich, Daniel Mohler, bestätige, dass es sich bei der hier vorgelegten Dissertation um eine Originalarbeit handelt, die von mir selbständig angefertigt und abgefasst wurde.

To Julianna

Summary

Within the Standard Model of particle physics, *Quantum Chromodynamics* (QCD) describes the strong interaction between particles carrying color charge. The basic constituents of the theory are quarks and gluons. From these fundamental degrees of freedom, color-neutral composite particles are formed. In a simple quark model view, these are *mesons*, which are bound states of a quark and an antiquark, and *baryons*, which consist of one quark of each of the three colors. In the relativistic quantum field theory, these *hadrons* may also contain gluonic excitations or additional quark-antiquark pairs. In this thesis, we study hadrons from an *ab initio* calculation in a discrete, four-dimensional Euclidean space-time. A discrete lattice is introduced to regularize the theory of Quantum Chromodynamics which enables us to calculate observables using numerical techniques developed in the context of statistical mechanics.

The parameters of the theory are the inverse gauge coupling β and the masses for each quark flavor. For practical calculations, only the light quarks are treated dynamically and one either uses two mass-degenerate light quarks (up and down quarks) or includes the somewhat heavier strange quark in the simulations and works with 2+1 flavors of quarks. In general, lattice calculations involving light quarks are computationally demanding. Therefore, current simulations are performed at unphysically large quark masses. While the lightest mesons, the pions, which are also the pseudo-Goldstone bosons of the theory, have a physical mass of roughly 140 MeV, most lattice simulations are performed with pion masses of 300 MeV or larger. In addition to an extrapolation to the continuum and infinite volume limits, this necessitates an extrapolation to the physical quark masses.

Lattice QCD is the method of choice for calculations of strong-interaction properties. In particular, the calculation of the ground state spectrum of hadrons improved considerably over the years and in some cases, an impressive agreement between theory and experiment can already be reached. While these states are a good benchmark for lattice calculations, a large number of hadron excitations are known from experiment and calculating their properties from first principles would be desirable. Unfortunately, extracting information about excited states from lattice calculations is not straight-forward. In general, excited states only contribute as sub-leading exponentials to Euclidean space correlation functions. The isolation of these small contributions is the topic of this thesis.

In Chapter 1 we provide some general information and briefly introduce the reader to this topic. The basics of both Quantum Chromodynamics and its lattice discretization are briefly reviewed in Chapter 2. We introduce the *gauge links* and identify their counterpart in the continuum. We then proceed to present the *plaquette gauge action* and, after a short discussion of problems associated with a naïve discretization, the *Wilson action*. As this action lacks *chiral symmetry*, an important symmetry of the (massless) continuum theory, we also briefly review chiral fermion actions and introduce *Chirally Improved* fermions with which we work throughout the larger part of this thesis. For the remainder of the chapter, we discuss the calculation of observables on the lattice and the extrapolations needed to obtain results that can be compared to experiment.

In Chapter 3 we explain why lattice calculations of excited state properties are a challenge and we discuss methods for excited state spectroscopy. In particular, we introduce our method of choice, the variational method [1, 2]. For this method a suitable basis of interpolating field operators has to be constructed. Complications due to the loss of continuous rotational symmetry are discussed and we introduce two distinct ways of constructing suitable interpolating fields. Towards the end of the chapter, we briefly point out some other recent methods which are computationally expensive but promising.

The first three chapters serve to introduce the basic concepts, which are applied to compute observables in the remaining chapters of this thesis. Many of the results presented here have already been published with my co-authorship. In this summary, I will refer to those publications.

In Chapter 4 results from light-quark meson spectroscopy are presented. We start with results from a study of mesons in quenched QCD. Here, so-called derivative quark sources are used to increase the overlap with both ground and excited meson states of spins 0 and 1. Most of our findings have previously been published in [3] and preliminary results can be found in [4]. After demonstrating the benefits of this construction, we move on and apply the same methods to a larger number of channels using the dynamical lattices created within the BGR collaboration's dynamical fermion project. An overview of the current status of these simulations has been provided in [5]. Previous results with a direct connection to this thesis have also been discussed in [6, 7] and we use some of the results presented in [8]. We also compare the results from dynamical QCD to older quenched results and comment on possible improvements. In the last section, we introduce an alternative *tetraquark* interpretation for some of the experimental states and study the spectrum of scalar mesons with an appropriate basis. This last section is work done in collaboration with Sasa Prelovsek and published in [9]. In addition, Appendix A provides tables of interpolating fields and Appendix C collects source and run parameters for our CI simulations.

In Chapter 5 we use similar methods for the spectroscopy of charmonium states on the lattice. This exploratory study has been done in collaboration with Carleton DeTar, Tommy Burch and Ludmila Levkova from the Fermilab-MILC collaboration. The MILC collaboration provided the gauge configurations for this study and Carleton DeTar modified existing code to be used for our purposes. We motivate our approach by briefly commenting on the experimental situation concerning charmonium excitations. We then modify the method described in Chapter 3 to be more suitable for our purpose. Tables of the interpolating fields we use can be found in Appendix B. First results from one ensemble of gauge configurations are presented and we comment in detail which of the physics objectives outlined previously can realistically be achieved in a larger scale study. In a short outlook, we comment on the steps needed for a more thorough investigation. Such an investigation is already planned for the near future.

Chapter 6 provides a brief overview of results from ground state spectroscopy of baryon states using CI lattices. These results will be needed for the study of baryon axial charges presented in Chapter 7. For this part of the thesis, we change the point of view and use the methods developed for the spectroscopy of excited states to suppress exited state contaminations to baryon three-point functions. We outline our approach for the calculation of *sequential propagators*, which are needed for a lattice evaluation of axial charges. We briefly comment on the renormalization constants which relate the lattice results to values in the $\overline{MS}$ renormalization scheme. We then present preliminary results for the axial charges of the nucleon and the Σ and Ξ hyperons. We conclude this chapter with a brief outlook. Appendix D provides additional details about the Krylov

subspace solver we used for the calculation of sequential propagators. We are currently extending our calculations for the axial charges and plan to report more details in a forthcoming publication. A first presentation will also appear in [10].

To conclude, we summarize our main findings and outline possibilities for further research in Chapter 8. For this, we focus on the general achievements from the previous chapters and point out possible extensions of existing calculations.

Contents

List of Figures

List of Tables

Chapter 1

Introduction

While Quantum Chromodynamics (QCD) is established as the theory of the strong interaction, computing observables from first principles has proven to be a rather non-trivial task. At short distances or large momenta, QCD exhibits the phenomenon of *asymptotic freedom* enabling a perturbative expansion in the coupling constant. At a certain energy scale, this expansion breaks down and non-perturbative effects have to be taken into consideration.

Lattice QCD, as introduced by K. Wilson [11], provides a regularization of QCD by a grid in four-dimensional Euclidean space time. This regularization enables an *ab-initio* calculation of strong interaction properties in the non-perturbative regime. For the calculations one applies the path integral quantization and obtains integrals similar to those in statistical mechanics. One then exploits this formal equivalence to apply Markov-chain Monte Carlo methods, which have been used for a long time in the context of statistical physics. Monte Carlo simulations involving light dynamical fermions on the lattice are computationally demanding, and therefore, simulations are usually performed at unphysically heavy quark masses. In recent years, calculations with quark masses corresponding to pions of approximately 300 MeV have been performed by multiple collaborations using a variety of fermion discretizations [12]. First attempts of lattice QCD simulations directly at physical quark masses have also been made [13].

In this thesis the focus will be on *hadrons*, the QCD bound states of quarks and gluons. Such states have to be color neutral and there are two basic types: *Mesons* and *baryons*. In the naïve quark model, mesons consist of a quark and an antiquark and baryons consist of one quark of each of the three colors. In QCD, more general states may exist which contain gluonic excitations or additional quark-antiquark pairs. For lattice QCD, the spectrum of hadronic states is interesting in several ways. For one, it can be viewed as a benchmark calculation, as there are a large number of experimental states which are known to a good accuracy. At the same time, lattice QCD also predicts states that are so far not observed and may help to shed some light on the structure of known hadronic states. Over the years, calculations of the ground state meson and baryon spectrum have been refined and an impressive agreement with the experimentally observed ground state spectrum has recently been achieved [14]. Taking a look at the experimental situation, which is periodically documented in the *Review of particle physics* [15], one however realizes, that ground states are only a small part of the observed spectrum. In addition, there are a large number of well known hadronic excitations. Lattice QCD calculations of excited state properties are more difficult. In Euclidean correlation functions, which are measured on the lattice, contributions from excited states appear as sub-leading exponentials. This necessitates more elaborate methods to reliably extract

such states. Moreover, most excitations are not stable states but rather resonances and ultimately, one would like to also extract their width. As an additional challenge, lattice artifacts from the breaking of continuum rotational symmetry complicate the analysis of the excited state spectrum.

The topic of this thesis is the calculation of excited state properties from Lattice QCD. As such, it is part of the larger effort pursued by the *Bern-Graz-Regensburg (BGR) collaboration*. Within this collaboration, gauge configurations containing two flavors of light dynamical sea quarks are generated. This thesis is organized as follow: In Chapter 2, some basics of the lattice approach to Quantum Chromodynamics are presented along with a short account of the methods used for simulations with Chirally Improved (CI) quarks. Chapter 3 focuses on the techniques for extracting excited state properties from the variational method. In Chapter 4, we apply these methods to light-quark mesons and calculate the spectrum of ground and excited states on both quenched and dynamical CI configurations. Similar methods are subsequently used in Chapter 5 to study the spectrum of meson states containing heavy *charm* quarks and antiquarks. In Chapter 6 we briefly present some of the results for the ground state spectrum of baryons. These will be used in Chapter 7 for the calculation of the axial charge G_a of some of the octet baryons. Finally, we present our concluding remarks in Chapter 8. In addition, the appendices provide more details about our simulations and some reference tables.

Chapter 2

Quantum Chromodynamics on the lattice

In this chapter, we review some basics of the lattice discretization of Quantum Chromodynamics. First, we take a short look at the classical theory and its discretization. After a discussion of the Wilson-action, we briefly describe the construction of lattice actions with chiral symmetry. We proceed with a short outline of the steps involved in calculating hadronic observables on the lattice, including the Hybrid Monte Carlo [16] algorithm used to generate the gauge configurations. We finish this chapter by discussing the extrapolations needed to compare lattice results to experiment and the continuum theory. Where appropriate, we focus on the example of Chirally Improved (CI) fermions (see Section 2.5) which will be used for most of the calculations in subsequent chapters.

2.1 The classical theory

In a 4-dimensional Euclidean space, the action of QCD can be written as

$$\begin{aligned} S_{QCD}[\psi,\bar{\psi},A] &= S_F + S_G \\ &= \sum_{f=1}^{N_f} \int \mathrm{d}^4x \left(\bar{\psi}^{(f)}(x) \left(\gamma_\mu D_\mu + m^{(f)} \right) \psi^{(f)}(x) \right. \\ &\qquad \left. + \frac{1}{2g^2} \mathrm{tr}[F_{\mu\nu}(x) F_{\mu\nu}(x)] \right) \ , \end{aligned} \tag{2.1}$$

with the field-strength tensor $F_{\mu\nu}$ given by

$$F_{\mu\nu}(x) = \partial_\mu A_\nu(x) - \partial_\nu A_\mu(x) + \imath [A_\mu(x), A_\nu(x)] \ .$$

Here, A_μ is an algebra-valued non-abelian gauge field and ψ, $\bar{\psi}$ are Dirac spinors representing the quark fields. S_F stands for the fermionic part of the action, while S_G denotes the purely gluonic part. The sum runs over all quark flavors and the mass m is in general different for all six species of quarks occuring in Nature[1].

The field strength tensor $F_{\mu\nu}$ and the covariant derivative $D_\mu = \partial_\mu + \imath A_\mu(x)$ are defined such that the total action is invariant under local $SU(3)$ gauge transformations.

[1]For most of our lattice simulations, we will restrict ourselves to two mass-degenerate flavors of sea quarks and 2+1 flavors of valence quarks. In Chapter 5 we use 2+1 light flavors of sea quarks and heavy valence charm quarks.

Notice that A_μ is a non-abelian field and that the resulting self-interactions of the gluon fields give rise to the complex nonlinear behavior which leads to confinement.

This theory can be quantized using the *Path Integral* method of quantization. For details of this method, we refer the reader to standard textbooks of quantum field theory (for a nice account see for example [17]).

2.2 Euclidean correlation functions

For the calculation of observables in subsequent chapters, the main objects of interest will be correlation functions in Euclidean space-time. Here, we motivate the lattice calculation of Euclidean correlators of some general Hilbert-space operators $\hat{O}_1$ and $\hat{O}_2$. We summarize the most important formulas and refer the reader to [18] for more details. Using standard time evolution, a correlator of two Hilbert-space operators can be written as

$$\left\langle \hat{O}_2(t)\hat{O}_1(0)\right\rangle_T = \frac{1}{Z_T}\mathrm{tr}\left(e^{-T\hat{H}}e^{t\hat{H}}\hat{O}_2e^{-t\hat{H}}\hat{O}_1\right) \ .$$

Taking the formal limit $T\to\infty$ of this expression we obtain

$$\lim_{T\to\infty}\left\langle \hat{O}_2(t)\hat{O}_1(0)\right\rangle_T = \sum_n e^{-t\Delta E_n}\left\langle 0|\hat{O}_2|n\right\rangle\left\langle n|\hat{O}_1|0\right\rangle \ , \tag{2.2}$$

where $\Delta E_n = E_n - E_0$ is the energy difference relative to the energy of the vacuum. The same correlator can also be expressed as a path integral

$$\begin{aligned}\left\langle \hat{O}_2(t)\hat{O}_1(0)\right\rangle_T &= \frac{1}{Z_T}\int \mathcal{D}[\psi,\bar{\psi},U]e^{-S_E}O_2[\psi,\bar{\psi},U]O_1[\psi,\bar{\psi},U], \\ Z_T &= \int \mathcal{D}[\psi,\bar{\psi},U]e^{-S_E}.\end{aligned} \tag{2.3}$$

Here Z_T ensures the proper normalization and the fields U will be introduced in the next section. To regularize QCD, we will discretize it on a space-time grid - the lattice - and exploit the formal equivalence to expressions from statistical mechanics to evaluate the path integral using some sort of (importance sampling) Markov chain Monte-Carlo.

2.3 A simple formulation of Lattice QCD

We discretize space-time on a four dimensional (hyper)cubic lattice Λ, which serves as an ultraviolet regulator. In the following, we present the simplest formulation of a lattice action for QCD, which has been suggested by K. G. Wilson in 1974 [11]. Wilson's approach is to define a lattice theory with an action that is explicitly gauge invariant at any lattice spacing a. The other important demand is, that the lattice action approaches the continuum form in the limit $a\to 0$. In a naïve discretization of the Dirac field [11], terms involving fermion fields at different space-time points arise. As an example, terms of the type $\bar{\psi}(n)\psi(n+\hat{\mu})$, where $n+\hat{\mu}$ is the neighbor of site n in the positive μ-direction, occur. These terms are not gauge invariant. To obtain gauge invariant expressions, we will need objects that take the role of the *gauge-transporter* $G(x,y)$ from the continuum theory. In the continuum, it is defined as

$$G(x,y) = P\mathrm{exp}\left(\int_C \imath g A \mathrm{d}s\right) \ , \tag{2.4}$$

where P stands for the path ordered expression, the fields A are the usual gauge fields from the continuum theory and the integral is along a curve C connecting the space-time points x and y. To construct such an object on the lattice, it is sufficient if we recover the continuum expression in the limit $a \to 0$. We therefore define *link variables* U_μ which live on the links between adjacent lattice sites n and $n + \hat{\mu}$:

$$U_\mu(n) = \exp\left(\imath a A_\mu\left(n + \frac{\hat{\mu}}{2}\right)\right) \ . \tag{2.5}$$

Here the A_μ are algebra-valued lattice fields and the link variables U_μ are elements of the gauge group SU(3). It is straight-forward to show [18], that this construction approximates the continuum gauge transporter up to terms of order a:

$$U_\mu(n) = G(n, n + \hat{\mu}) + \mathcal{O}(a) \ .$$

Therefore, the quark fields ψ and $\bar{\psi}$ live on the lattice sites and, in analogy to the gauge transporter of the continuum quantum field theory, the link variables live on the links between two adjacent lattice sites.

2.3.1 The Wilson gauge action

It is now straight forward to discretize the gauge part of the action, as the trace over closed loops of link variables. Any such trace over closed loops is a gauge invariant quantity as required for Wilson's construction. Counting each loop only once, the gauge part of the action S_G can then be written as

$$S_G[U] = \frac{2}{g^2} \sum_{n \in \Lambda} \sum_{\mu < \nu} \mathrm{Re}\,\mathrm{tr}(\mathbb{1} - U_{\mu\nu}(n)) \ , \tag{2.6}$$

where the so called *plaquettes* $U_{\mu\nu}$ are the smallest possible loops given by the product of four link variables

$$U_{\mu\nu}(n) = U_\mu(n) U_\nu(n + \hat{\mu}) U_{-\mu}(n + \hat{\mu} + \hat{\nu}) U_{-\nu}(n + \hat{\nu}) \ ,$$

and $U_{-\mu}(n) = U^\dagger(n - \hat{\mu})$. Instead of the coupling g, one usually uses the inverse gauge coupling β

$$\beta = \frac{6}{g^2} \ .$$

In general, it is advantageous to replace this simplest type of gauge action by an *improved action* displaying less discretization errors. For generating the gauge configurations used in this thesis, the *Lüscher-Weisz* gauge action [19, 20] has been used instead of the simple Wilson *plaquette action*.

2.3.2 Naïve fermions and the doubling problem

The discussion in this section follows closely the account in [18]. A naïve discretization of the fermionic part of the action using central differences for the derivatives is given by Equation 2.7,

$$S_F[\psi, \bar{\psi}, U] = a^4 \sum_{f=1}^{N_f} \sum_{n \in \Lambda} \Bigg(\bar{\psi}^f(n) \sum_{\mu=1}^{4} \gamma_\mu \frac{U_\mu(n)\psi^f(n + \hat{\mu}) - U_{-\mu}(n)\psi^f(n - \hat{\mu})}{2a} + m^f \bar{\psi}^f(n)\psi(n) \Bigg) \ . \tag{2.7}$$

Here the index f runs over all quark flavors, ψ and $\bar{\psi}$ are fermion fields and the link variables U are defined as in the previous section. Taking a look at the free theory (this corresponds to setting all link variables to 1: $U_\mu(n) \equiv 1 \,\forall\, n$) with massless fermions, one can obtain an analytic expression for the Dirac operator and for its inverse, the *quark propagator*. In momentum space we obtain

$$\tilde{D}(p) = \frac{\imath}{a} \sum_{\mu=1}^{4} \gamma_\mu \sin(a p_\mu) \ , \tag{2.8}$$

$$\tilde{D}(p)^{-1}\Big|_{m_q=0} = \frac{-\imath a^{-1} \sum_\mu \gamma_\mu \sin(p_\mu a)}{a^{-2} \sum_\mu \sin(p_\mu a)^2} \ . \tag{2.9}$$

At any finite lattice spacing, this expression has a pole not only at $p = (0,0,0,0)$, but also whenever $p_\mu a = \frac{\pi}{a}$, which is also the case for a whole set of points

$$\left\{ \left(\frac{\pi}{a}, 0, 0, 0\right), \left(0, \frac{\pi}{a}, 0, 0\right), \ldots, \left(\frac{\pi}{a}, \frac{\pi}{a}, \frac{\pi}{a}, \frac{\pi}{a}\right) \right\} \ .$$

These fifteen unwanted poles are called *doublers*. To solve this problem, a so-called *Wilson term* can be added to the lattice Dirac operator. In momentum space this additional term reads

$$\tilde{W}(p) = \mathbb{1} \frac{1}{a} \sum_{\mu=1}^{4} (1 - \cos(a p_\mu))$$

and the whole momentum space Dirac operator including the Wilson term is given by

$$\begin{aligned} \tilde{D}_W &= \tilde{D} + \tilde{W} \\ &= \mathbb{1} m + \frac{i}{a} \sum_{\mu=1}^{4} \gamma_\mu \sin(a p_\mu) + \mathbb{1} \frac{1}{a} \sum_{\mu=1}^{4} (1 - \cos(a p_\mu)) \ . \end{aligned}$$

We therefore obtain for the full Wilson Dirac operator in position space

$$D^{(f)}(n|m)^{\alpha\beta}_{ab} = -\frac{1}{2a} \sum_{\mu=\pm 1}^{\pm 4} (1 - \gamma_\mu)_{\alpha\beta} U_\mu(n)_{ab} \delta_{n+\hat{\mu},m} + \left(m^{(f)} + \frac{4}{a} \right) \delta_{\alpha\beta} \delta_{ab} \delta_{mn} \ . \tag{2.10}$$

The Wilson term is a lattice discretization of a second derivative and gives an additional mass to all doublers, such that they decouple from the theory in the continuum limit. Notice that, just like a quark mass term, such a term also breaks chiral symmetry explicitly. We will talk about lattice fermions preserving this important symmetry in the next two sections.

2.4 Chiral symmetry and the Ginsparg Wilson relation

In the limit of vanishing quark masses, the QCD action 2.1 is symmetric under $SU(N_F)_L \times SU(N_F)_R$ *chiral symmetry*. The Dirac-Operator for such a chirally symmetric theory fulfills the equation

$$\{D, \gamma_5\} = 0 \ . \tag{2.11}$$

As the Wilson term introduced in Section 2.3.2 breaks this symmetry, the task was to find a lattice implementation of chiral symmetry that would be free of doublers. It turns

out that relation 2.11 has to be relaxed to achieve this, as the *Nielsen-Niomiya Theorem* [21, 22] states, that a Dirac operator which is free of doublers cannot simultaneously be local, translation invariant, chirally symmetric in the sense of 2.11 and give rise to a hermitian Hamiltonian.

The way out is to replace 2.11 with the milder condition [23]

$$\{D, \gamma_5\} = a\frac{1}{2} D \left(\gamma_5 R + R\gamma_5\right) D \ , \tag{2.12}$$

where R is a local operator on the lattice. This enables us to implement chiral symmetry on the lattice [24]. In the next section, we present an overview of Dirac operators fulfilling this so-called *Ginsparg-Wilson relation* either exactly or approximately.

2.5 Implementations of chiral fermions

In this section, we will briefly introduce the Overlap solution to the Ginsparg-Wilson relation 2.12. We then focus on a particular type of approximate solution used within the Bern-Graz-Regensburg (BGR) Collaboration, the Chirally Improved (CI) Dirac operator. For completeness we also would like to briefly mention two other approximate solutions of the Ginsparg-Wilson relation which we will not discuss in detail:

- **Domain wall fermions**
  Domain wall fermions [25, 26] approach the overlap operator in the limit of infinite extent of an additional 5th dimension. In practical calculations, a finite extent for this fifth dimension has to be chosen. For recent simulations with 2+1 flavors of domain wall fermions please refer to [27] and references therein.

- **Fixed point fermions**
  The fixed point operator [28, 29] has an Ansatz similar to the CI (see below), but its coefficients are chosen from a saddle-point approximation of the renormalization group equation [30].

2.5.1 Overlap fermions

The Overlap Dirac operator [31, 32] fulfills the Ginsparg-Wilson relation with $R = \mathbb{1}$. The massless version is given by

$$D_O^{(0)} = \mathbb{1} + \gamma_5 \mathrm{sign}(\gamma_5 D_k) \ , \tag{2.13}$$

where D_k is a suitable, doubler-free kernel operator. For computational reasons, the Wilson Dirac operator 2.10 is usually used. To simulate massive fermions,

$$D_O(m_0) = 1 + m_0 + (1 - m_0)\gamma_5 \mathrm{sign}(\gamma_5 D_k) \tag{2.14}$$

with mass parameter $m_0 \in [0, 1]$ can be used (see for example [33]). In addition to this solution, more general versions can be found and we refer the reader to [34] for their construction. We would also like to point out, that, while simulations with Overlap fermions are desirable and are being pursued by several groups [35, 36, 37, 38, 39, 40, 41, 42, 43, 44, 45], the evaluation of the matrix sign function appearing in 2.13 makes implementations of Overlap fermions extremely costly in terms of computing power. For our calculations, we therefore opt for an approximate solution to 2.12 which we will now introduce.

2.5.2 Chirally Improved fermions – An approximate solution of the Ginsparg-Wilson relation

The Chirally Improved (CI) lattice Dirac operator [46, 47] uses the general Ansatz

$$D_{mn} = \sum_{\alpha=1}^{16} \Gamma_\alpha \sum_{p \in \mathcal{P}^\alpha_{m,n}} c_p^\alpha \prod_{l \in p} U_l \, \delta_{n,m+p} \tag{2.15}$$

to express the Dirac operator as a sum over all elements of the Clifford algebra Γ_α times paths of links weighted by coefficients c_p^α. The number of non-vanishing coefficients can be restricted by symmetry arguments. One then inserts this Ansatz into the Ginsparg-Wilson relation 2.12 and truncates the length of possible paths occuring in 2.15. This leads to a set of algebraic equations which can be solved by norm minimization to obtain an approximate solution of the Ginsparg-Wilson relation. For our simulations, the length of the paths contributing to the construction of the CI has been limited to length four.

For full-QCD simulations with CI fermions, the approach described in [5] has been used. The coefficients for the CI are fixed for one simulation and the same coefficients are used for all other simulations. This implies an additive mass renormalization. For a list of CI parameters please refer to [5]. In addition, a list of current ensembles and run parameters can be found in Appendix C.

2.6 Calculating hadronic observables on the lattice

Starting with a discretization of the path integral from Equation 2.3, we can integrate out the fermion degrees of freedom and obtain integrals of the type

$$\left\langle \hat{O}_2(t)\hat{O}_1(0) \right\rangle = \frac{1}{Z} \int \mathcal{D}[U] e^{-S_G[U]} \mathrm{det}D_{f1} \mathrm{det}D_{f2} \ldots \mathrm{det}D_{fN} \, (\ldots) \tag{2.16}$$

for a number N of flavors where $\mathrm{det}D_{f1}$ stands for the fermion determinant of flavor 1 as obtained from the Grassmann integration over the fermion fields and $(\ldots)$ stands for the omitted part which depends on the observables. The *partition function* Z which normalizes this expression is given by

$$Z = \int \mathcal{D}[U] e^{-S_G} \mathrm{det}D_{f1} \mathrm{det}D_{f2} \ldots \mathrm{det}D_{fN} \; .$$

One then includes the fermion determinants as a weight factor into the Monte-Carlo simulation of the gauge fields. For dynamical simulations with mass-degenerate pairs of quark flavors and a γ_5-hermitian Dirac operator, this weight factor will be a positive real number

$$\det[D] \det[D] = \det[D] \det[D^\dagger] = \det[D \, D^\dagger] \geq 0 \; .$$

To calculate this determinant, one introduces one or more complex *pseudofermion fields* ϕ [48] and rewrites the product of determinants as an integral over these fields

$$\det \left[D \, D^\dagger \right] = \pi^{-N} \int \mathcal{D}[\phi_{Re}] \mathcal{D}[\phi_{Im}] \mathrm{e}^{-\phi^\dagger (D \, D^\dagger)^{-1} \phi} \; .$$

This integral can subsequently be performed numerically, which is the topic of the next section.

Neglecting the fermion determinants in integrals of type 2.16 is known as the *quenched approximation*. This is equivalent to neglecting the creation of quarks from and the annihilation of quarks into the vacuum (there are no quark loops in quenched QCD). While this is clearly an uncontrolled approximation which has mainly been motivated by considerations about computing time, it is surprising how well this approximation works for calculations of the mass spectrum. Some of the results in Chapter 4 have been obtained in the quenched approximation and we will clearly indicate this. In 4.2.4, we will also point out some of the artifacts arising from the quenched approximation.

2.6.1 Generating gauge field configurations using the Hybrid Monte-Carlo algorithm

In this section, we will briefly describe the generation of gauge fields with the so-called Hybrid Monte-Carlo or HMC algorithm [16] (see also [18] for a nice description of the ideas). The algorithm combines a *molecular dynamics* evolution of the gauge fields with a Metropolis-type accept/reject step. For the molecular dynamics part, one introduces hermitian matrices $P_{j,\mu}$ as *conjugate momenta* to the gauge links $U_{j,\mu}$. To ensure that the gauge links remain in $SU(3)$ [49] the derivative with respect to the *molecular dynamics time* $\dot{U}_{j,\mu}$ is defined by

$$\dot{U}_{j,\mu} := \imath P_{j,\mu} U_{j,\mu} \ ,$$

which is the equation of motion for $U_{j,\mu}$. To obtain the equation of motion for the conjugate momenta P, we demand that the derivative of the HMC Hamiltonian

$$H = \frac{1}{2} \sum_{j,\mu} \mathrm{tr} \left(P_{j,\mu}^2 \right) + S_G + \phi^\dagger (D\, D^\dagger)^{-1} \phi$$

with respect to the HMC time vanishes, $\dot{H} = 0$. For the CI Dirac operator, the equation of motion for the conjugate momenta is rather involved and details can be found in [50]. As the molecular dynamics evolution is only approximate, an accept/reject step is needed to correct this.

The current HMC implementation for CI fermions described in detail in [50, 5] features Hasenbusch mass preconditioning [51] with two pairs of pseudofermions, and a chronological [52] mixed precision [53] inverter. More recently, a new version of the algorithm employing a higher order Omelyan integrator [54] (instead of the Leap-Frog scheme used previously) and multiple timescale integration [55, 56] has been tested.

2.6.2 Quark propagators

To determine hadronic observables, we will have to calculate quark propagators resulting from the Wick-contractions of the fermion fields. Those propagators need to be computed on each gauge configuration within our ensemble. It however turns out, that the calculation of full quark propagators from all sites of a lattice to all other sites of a lattice would not be feasible, both from the point of view of the computations involved and from the point of view of computer storage. As an example, for one full propagator on a typical 4-dimensional lattice of size $16^3 \times 32$

$$\left(16^3 \times 32 \times 3 \times 4\right)^2 \tag{2.17}$$

complex doubles would have to be kept in storage. On standard computer systems, one single matrix of this size would therefore require roughly 36 Terabytes of storage, which is clearly too much.

The usual way of circumventing this problem is to create some sort of *quark source* and just store the result of applying a propagator to this quark source. In the simplest case, the quark source is just a point in space, color-space and Dirac-space and the result is known as a *point-to-all propagator*[2]. Quark smearing, as detailed in Section 3.6.2, will lead to more general quark sources.

Once we have constructed our quark sources b_i, the source-to-all propagators are obtained by finding the solutions x_i to the Matrix equation

$$Ax_i = b_i \ , \tag{2.18}$$

where A is the Dirac matrix. In general, this system of linear equations is solved by iterative methods such as Conjugate Gradient (CG) for symmetric positive definite matrices, the MINRES-method for symmetric non-definite matrices or some sort of Bi-Conjugate-Gradient (BiCG) method for non-symmetric matrices. For some applications, the linear system of equations 2.18 needs to be solved for many different sources (also referred to as *right-hand sides*) b_i. In this case so called *deflation algorithms* are a useful tool. In Appendix D we present a more elaborate method for solving linear systems of equations with many right-hand sides. This method is used in Chapter 7 for the calculation of sequential propagators.

2.6.3 Calculating observables

Once both the gauge fields and the quark propagators have been calculated, the same propagators can be used to calculate various observables on the given ensemble of gauge configurations. In Chapter 4, we will discuss in some detail how this is done on the example of general meson correlators.

2.7 The threefold of lattice extrapolations

In this section, we discuss the extrapolations necessary to obtain results that can be compared quantitatively to experiment. Any given lattice simulation is performed at some value of the bare mass parameter (or the mass parameters in case of simulations including the strange or even the charm quark) and at a certain inverse gauge coupling β. To obtain dimensionful quantities such as masses, one then uses a physical observable to set the lattice scale a. Possible scale-setting methods are summarized in Section 2.8. In the following we briefly outline the basic strategy for extrapolation of lattice results to the continuum, infinite volume and chiral limits.

2.7.1 Continuum limit

Observables measured on the lattice contain lattice spacing dependent discretization errors. For the example of masses M measured as M_{lat} on the lattice we have [18]

$$M_{lat} = M\left(1 + \mathcal{O}(a^{\alpha})\right) \tag{2.19}$$

with some positive integer power α. In general, α depends on the details of the lattice action used for the simulation as well as on the observable in question. To compare with experiment, one needs to perform a continuum extrapolation of lattice results, which corresponds to the limit $a(g, m_q) \to 0$. The usual strategy for this is to calculate

[2] Another common practice is to fix the gauge and use so-called *wall sources*.

the observables, whose scaling behavior is to be investigated, on lattices with the same physical size and multiple different lattice spacings. For a given observable, one can then determine the leading error term in Equation 2.19 and fit the data to obtain the values in the continuum limit.

This procedure is a delicate business with dynamical fermion simulations, as an extrapolation to the continuum should be performed along lines of constant physics. In [53], simulations at several values of the inverse gauge coupling β and at several quark masses are performed and interpolations are used to obtain masses of several hadrons along constant lines of physics. The volume is then, in general, not the same for each ensemble, but the authors of [53] keep the box size large to ensure that effects from the finite volume on the masses of stable particles are negligible.

For quenched simulations with CI fermions, the scaling behavior of masses has been studied in [30], and discretization effects have been found to be small even on rather coarse lattices. For simulations with dynamical CI lattices the current runs (see Table C.1 in the appendix) all have a similar lattice spacing and such a study is not possible with the current data.

2.7.2 Infinite volume limit

At any given volume, interactions due to the periodicity of the lattice lead to finite volume effects which, for large enough lattices, cause exponentially small corrections to the mass spectrum of hadrons [57]. The leading corrections come from the exchange of pions and are of the order $\exp(-m_\pi L)$. One often assumes that these corrections are small for $m_\pi L > 4$. In Chapter 7 we will present some data for an observable where this might not be the case. For resonances, the situation is more complicated and the method developed by Lüscher [58, 59] should be used to obtain the masses of resonances.

To estimate the size of these corrections and to correct the measured observables the usual approach would be to use lattices of varying box size while keeping all other parameters fixed. In practical calculations, one has to make sure that one stays far away from any phase transitions associated with a finite time extent and therefore with effects of finite temperature. In addition, for a fit to a form obtained from theory, one also has to make sure that the range of applicability of the theory is respected[3]. While the ground states of most hadrons show small effects from finite volume in the range of quark masses commonly used, the effect from squeezing excited states in a small box may be more severe.

2.7.3 Chiral limit

For lattice QCD, the values of the current quark masses are parameters of the simulation. Depending on the action, the mass parameter m_0 does not give the quark mass directly. In general one therefore first calculates the so-called axial Ward identity (AWI) quark mass, defined through

$$m_{AWI} = \frac{\langle \partial_t A_4(\vec{p}=0,t) P(0) \rangle}{\langle P(\vec{p}=0,t) P(0) \rangle} \ . \tag{2.20}$$

By themselves, the quark masses are not observables. At the same time, the quark masses determine the mass of the pion, the nucleon and other hadrons. The famous

[3] See for example Colangelo et al. [60] for a discussion of the range of box sizes for which the corresponding χPT formulae are expected to produce the correct result.

Gell-Mann - Oakes - Renner (GMOR) relation [61]

$$f_\pi^2 m_\pi^2 = -2 m_q \Sigma \ , \tag{2.21}$$

where f_π is the pion decay constant and Σ is the chiral condensate, relates (to leading order in the quark mass) the quark mass m_q and the pion mass m_π.

Compared to the typical hadronic scale, the pions (as the pseudo-Goldstone bosons of the theory) are rather light (approximately 140MeV), and so are the up and down quarks ($\frac{m_u+m_d}{2} \approx 2.5-5\,\mathrm{MeV}$ [15] in the $\overline{MS}$ scheme at $\mu = 2GeV$). For such light quark masses, lattice QCD calculations get prohibitively expensive and numerical calculations may even break down completely due to small eigenvalues of the Dirac operator caused by discretization and finite volume effects. Therefore most current lattice QCD calculations are performed at pion masses substantially higher than in Nature[4], necessitating some sort of extrapolation when comparing results to experiment. In addition, the light quarks are usually assumed to be mass-degenerate, even though experimental data indicates a small mass-splitting between the up and the down quarks.

To guide extrapolations to the physical pion mass, the low energy effective theory of QCD, called *Chiral Perturbation Theory* or χPT [63, 64] is often used. At a given order, a certain number of low energy constants appear and have to be fixed from experiments or lattice data in order for the theory to be predictive. Order by order, more such low energy constants appear in the chiral expansion as the effective theory is not renormalizable with a finite number of counterterms. Comparison between lattice QCD and χPT is therefore of mutual benefit, as Chiral Perturbation Theory can be used for extrapolating lattice results while we may learn something about the range of applicability of the effective theory and determine the low energy constants from lattice data. As an example, it is not *a priori* clear if SU(2) Chiral Perturbation Theory or SU(3) Chiral Perturbation Theory should be used for an analysis of the pseudoscalar meson sector. In the real world, the kaon mass is not really heavy compared to the pion mass and, at the same time, the strange quark mass is heavy enough to doubt that SU(3) is a good symmetry. Recent next-to-leading order calculations [13, 65] suggest that SU(2) χPT may in fact be more suitable.

From a theorists point of view, varying the pion mass can be regarded as another tool in the toolbox to understand QCD. There are reasons to assume that calculations at light-quark masses corresponding to the physical pion mass will be feasible in the near future and, as mentioned previously, first attempts have been made [13]. This progress is mainly due to the continuous increase in computing power and due to algorithmic improvements.

2.8 Setting the scale

There are various possibilities for the determination of the lattice scale. Before we describe the method used for simulations with dynamical CI fermions, we comment on some other possibilities and point out some of the issues associated with these choices. As pointed out in [14], it is desirable to choose a quantity for the scale setting, which can be measured on the lattice to a high accuracy and is precisely determined experimentally. At the same time the systematic errors in the determination of the quantity should be well under control. This last requirement makes masses of unstable particles like the ρ

[4] Although the PACS-CS collaboration is working at pion masses as low as 156 MeV [13], which is close to the physical point. Using reweighting techniques [62], they may be able to translate these into results at the physical point.

meson mass, which in the past has often been used to set the scale, a bad choice, as the ρ is a resonance rather than a stable bound state and therefore extrapolation to the chiral limit (see also 2.7.3) is a rather non-trivial task. On the other hand, the mass of the Ω baryon has only minimal ambiguities from the chiral extrapolation [27], and several groups [14, 27, 65, 13] use the mass of the Ω (or in [14] alternatively the Ξ) baryon to set the lattice scale. All above groups determine the light and strange quark masses from a chiral extrapolation [27, 13] of the mass or from an extrapolation of the ratio of the pion mass over the omega mass and the kaon mass over the omega mass [14] respectively. As pointed out in [27], the determination of the quark masses and the lattice spacing is a coupled problem.

Another choice for the setting of the scale has been adopted by the European Twisted Mass Collaboration [66, 67]. The pion decay constant f_π is used as a physical input and three different forms are used for the chiral extrapolations. They find that the systematic uncertainties from the choice of extrapolation are not negligible and therefore work with different values of the lattice spacing and quote this as a systematic error for quantities determined consistently within the same approach.

We instead use the Sommer parameter [68] to determine the lattice scale for the dynamic CI simulations [5]. This has been a popular choice for many quenched simulations and has also been used for other dynamical simulations [37]. In this approach, one extracts the static quark potential $V(r)$ from linear fits to the logarithm of the $r \times t$ *Wilson loops* $\ln(W(r,t))$. The potential can then be fit to the form

$$V(r) = A + \frac{B}{r} + \sigma r + C\Delta V(r) \ ,$$
$$\Delta V(r) = \left[\frac{1}{r}\right] - \frac{1}{r} \ ,$$

where the perturbative lattice Coulomb potential for our case can be found in [5]. The Sommer parameter r_0 is then given by

$$r_{0,lat} = \sqrt{\frac{1.65 + B}{\sigma}} = \frac{r_0}{a} \ .$$

We use $r_0 = 0.48\,\mathrm{fm}$ to set the lattice scale. As the value of r_0 is not determined precisely from experiment, other groups use different values. In [37] a Sommer parameter of $0.49\,\mathrm{fm}$ is used. The MILC Collaboration [69] uses mass differences in the Υ spectrum and the static quark potential to determine the Sommer scale. They obtain a value of $r_0 = 0.462(11)(4)\,\mathrm{fm}$ after a continuum extrapolation. After first setting the scale using hadronic observables, the authors of [13] try to determine the Sommer parameter r_0 at the physical point and obtain a value of $0.4921(64)(+74)(-2)\,\mathrm{fm}$. Using the method described above, Boucaud et al. [66] obtain the value of $r_0 = 0.454(7)\,\mathrm{fm}$. As a word of caution, one should note that, depending on the method and the data available, systematic errors from setting the lattice scale may be substantial and in some cases even larger than the statistical errors stemming from the finite number of configurations.

Chapter 3

Excited state spectroscopy

In this chapter, we describe how to obtain information about the mass spectrum of QCD from a lattice approach. While ground states are rather straightforward to extract, excited hadrons are difficult to study on the lattice. In the first part of this chapter, we revisit the Euclidean correlation functions introduced in Chapter 2 and explain why excited states are more difficult to extract. We proceed in Section 3.2 with a short overview of methods that have been successfully used for lattice spectroscopy of excited states and describe one of these approaches, the variational method [1, 2], in more detail in Section 3.3. There, we also outline how the variational method can be used to calculate quantities other than the mass spectrum. After having described our method of choice for excited state spectroscopy, we briefly outline our procedure for analyzing and fitting data from the variational method in Section 3.4.

For the variational method, a suitable basis of interpolating fields is needed. On a discrete space-time lattice, the construction of such a basis is complicated as the continuous rotational symmetry is broken. In Section 3.5 we describe how this affects the construction of a suitable basis and we proceed to explain how this problem can be attacked. Once those technical obstacles are out of the way, we introduce (see 3.6) two different approaches commonly used in the literature along with the techniques needed for their implementation. We conclude the chapter by briefly mentioning some new developments which may be of importance for future studies.

3.1 Euclidean correlators revisited

In Section 2.2, we sketched how Euclidean-space correlation functions $C(t)$ can be expressed as a path integral which can be computed on the lattice. From Equation 2.2, we see

$$C(t) \sim \sum_n a_n \mathrm{e}^{-tE_n} \ . \tag{3.1}$$

Therefore, to a given correlator, a whole tower of states with different energies E_n contributes. If there is a large enough gap between the ground state and the excitations, a clean signal for the ground state can be extracted by fitting the correlator to a single exponential at large Euclidean time separations.

To visualize the behavior of single correlators, one often plots so called *effective masses* defined by

$$a\, M_{\text{eff}} \left(t + \frac{1}{2} \right) = \ln \left(\frac{C(t)}{C(t+1)} \right) \ , \tag{3.2}$$

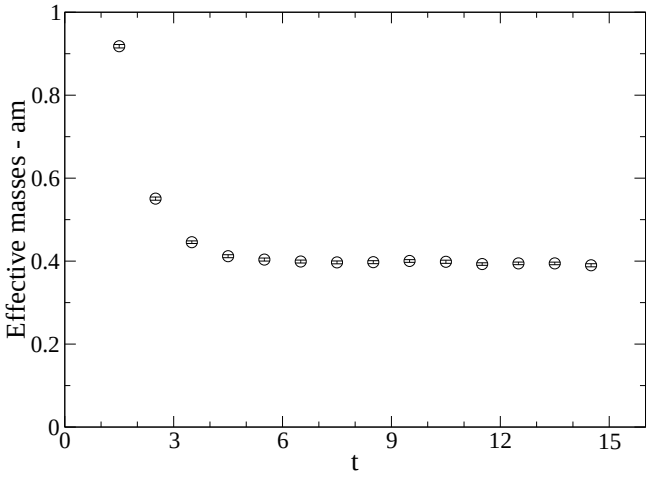

Figure 3.1: Effective mass from a single pseudoscalar meson correlator at intermediate quark mass. At small timeslices contributions from excited states are clearly visible. At large Euclidean times, the data is described well by a single exponential.

instead of the correlators themselves. Figure 3.1 shows an example of an effective mass plateau for a meson correlator in the pion channel.

While the extraction of ground states with above method is straightforward in a number of channels, excited states appear only as sub-leading exponentials in Euclidean two-point functions. With the intrinsically noisy data on a finite number of gauge configurations, extracting those sub-leading exponentials reliably is not straightforward: Simple multi-exponential fits are usually unstable. At the same time, contaminations from excited states may severely limit the fit ranges for observables associated with the ground state. In the next section, we will introduce a method to extract excited states which can also be used to obtain a cleaner signal for ground states in channels with significant excited state contributions.

3.2 Methods for excited state spectroscopy

Over the years a variety of approaches have been pursued to extract excited states on the lattice. While we focus on our method of choice in the rest of the chapter, we want to briefly mention other methods. We provide some references for each method, but this account is surely incomplete.

- **Bayesian methods:** In the context of the *maximum entropy method*, this approach has been discussed in [70] and such an approach has been used in [71, 72, 73]. Another approach is the so-called *Sequential empirical Bayes method* from [74]. This method has been used for various studies [75, 76]. Bayesian methods have also been used in [77].

- **NMR-inspired black-box method:** This method has been suggested in [78] and been applied in [79, 80].

- **Evolutionary fitting techniques:** Recently, evolutionary fitting techniques have been proposed [81] to extract excited states from lattice data. In [82], this method has been applied successfully to a study of the light meson spectrum.

- **The variational method:** The variational method [1, 2] described in detail below has been used extensively [83, 84, 85, 3, 86, 87, 88, 89, 90, 9, 91, 92, 93] by various collaborations. So far it is the most established method for the extraction of excited state properties from lattice QCD.

In the next section and for the rest of our discussion in this chapter, we focus on the variational method, which is used throughout this thesis.

3.3 The variational method

The basic idea is to use several different interpolators O_i, $i = 1, \dots N$ with the quantum numbers of the desired state and to compute the full matrix of cross-correlators[1],

$$C(t)_{ij} = \langle O_i(t) O_j^\dagger(0) \rangle. \tag{3.3}$$

These correlators have the Hilbert-space decomposition

$$\begin{aligned} C(t)_{ij} &= \sum_n \langle 0|O_i|n\rangle\langle n|O_j^\dagger|0\rangle \mathrm{e}^{-tE_n} \\ &= \sum_n v_i^{(n)} v_j^{(n)\star} \mathrm{e}^{-tE_n} \ . \end{aligned} \tag{3.4}$$

It can be shown [2], that the eigenvalues of the generalized eigenvalue problem

$$C(t)\vec{\psi}^{(k)} = \lambda^{(k)}(t) C(t_0) \vec{\psi}^{(k)} \tag{3.5}$$

behave as

$$\lambda^{(k)}(t) \propto \mathrm{e}^{-tE_k} \left(1 + \mathcal{O}\left(\mathrm{e}^{-t\Delta E_k}\right)\right) \ . \tag{3.6}$$

At fixed t_0, ΔE_k is given by

$$\Delta E_k = \min|E_m - E_n|, \qquad m \neq n \ , \tag{3.7}$$

while for the special case of $t \leq 2t_0$ and a basis of N correlators [94] ΔE_k is given by

$$\Delta E_k = E_{N+1} - E_n. \tag{3.8}$$

Therefore, at large time separations, each eigenvalue is dominated by a single state, allowing for stable two parameter fits to the eigenvalues. Consequently, the largest eigenvalue decays with the mass of the ground state, the second largest eigenvalue with the mass of the first excited state, and so on. In practice one first calculates the correlation matrix for a given set of interpolators. This matrix will have real eigenvalues provided that the matrix $C(t)$ is hermitian for all Euclidean times t and provided $C(t_0)$ is positive definite. One then simply diagonalizes the correlation matrix at each time slice and sorts the eigenvalues according to their magnitude. For the analysis, truncating the matrix to a suitable sub-matrix of interpolators may be favorable as it may lead to results with a smaller statistical uncertainty. We will come back to this when discussing results in Chapters 4 and 5.

[1] Unless mentioned otherwise, we will assume a projection to zero momentum for the following discussion.

In addition, the time independence of the eigenvector components can serve as a "fingerprint" for the physical state. To deal with orthogonal eigenvectors $\vec{\psi}^{(k)\prime}$, it is useful to switch to the regular eigenvalue problem,

$$C(t_0)^{-\frac{1}{2}} C(t) C(t_0)^{-\frac{1}{2}} \vec{\psi}^{(k)\prime} = \lambda_k(t) \vec{\psi}^{(k)\prime} \ . \tag{3.9}$$

In plots of eigenvector components we always plot $\vec{\psi}^{(k)\prime} = C_0^{\frac{1}{2}} \vec{\psi}^{(k)}$.

In the analysis, one is not limited to energy levels alone. Following [91], one can also extract the overlap factors v_i which are related to decay constants[2] for the case of point interpolators. With the definition of the $v_i^{(n)}$ from Equation 3.4

$$C(t) = \sum_{n=1}^{\infty} v_i^{(n)} v_i^{(n)\star} \mathrm{e}^{-tE^{(n)}} \ ,$$

we can calculate ratios

$$R(t)_i^{(k)} = \frac{|\sum_j C(t)_{ij} \psi_j^{(k)}|^2}{\sum_k \sum_l \psi_k^{(k)\star} C(t)_{kl} \psi_l^{(k)}} \approx v_i^{(k)} v_i^{(k)\star} \mathrm{e}^{-tE^{(k)}} \ ,$$

to extract the overlap of the i-th operator with the k-th state.

For the simulations in Chapter 7, we will also need to calculate three-point functions between baryon states. To isolate and suppress contaminations from excited states, we follow the approach outlined in [91]. More specifically, we calculate ratios of three point functions $T_1(t,t')$ and $T_2(t,t')$

$$R^{(k)} = \frac{\sum_i \sum_j \psi_i^{(k)} T_1(t,t')_{ij} \psi_j^{(k)}}{\sum_l \sum_m \psi_l^{(k)} T_2(t,t')_{lm} \psi_m^{(k)}} \ , \tag{3.10}$$

as well as at ratios of three-point functions over two-point functions $C(t)$

$$R^{(k)} = \frac{\sum_i \sum_j \psi_i^{(k)} T_1(t,t')_{ij} \psi_j^{(k)}}{\sum_l \sum_m \psi_l^{(k)} C(t)_{lm} \psi_m^{(k)}} \ .$$

Notice that we are using the simplified version from Equation (27) of [91]. We will describe this approach in more detail in Chapter 7. For now, we just want to state that the choice assumes translation invariance and time reflection symmetry which should both be manifest in an ensemble average.

3.4 Data analysis and fitting methodology

Just like in Equation 3.2 we can now define effective masses

$$a\, M_{\text{eff}} \left(t + \frac{1}{2} \right) = \ln \left(\frac{\lambda^{(k)}(t)}{\lambda^{(k)}(t+1)} \right) \ , \tag{3.11}$$

where $\lambda^{(k)}$ is the eigenvalue corresponding to the k-th state, as obtained from the generalized eigenvalue problem. Figure 3.2 shows a plot of typical eigenvalues and the corresponding effective masses. The effective masses are used to visually determine the fit ranges, while all fits will always be performed directly to the eigenvalues. In addition,

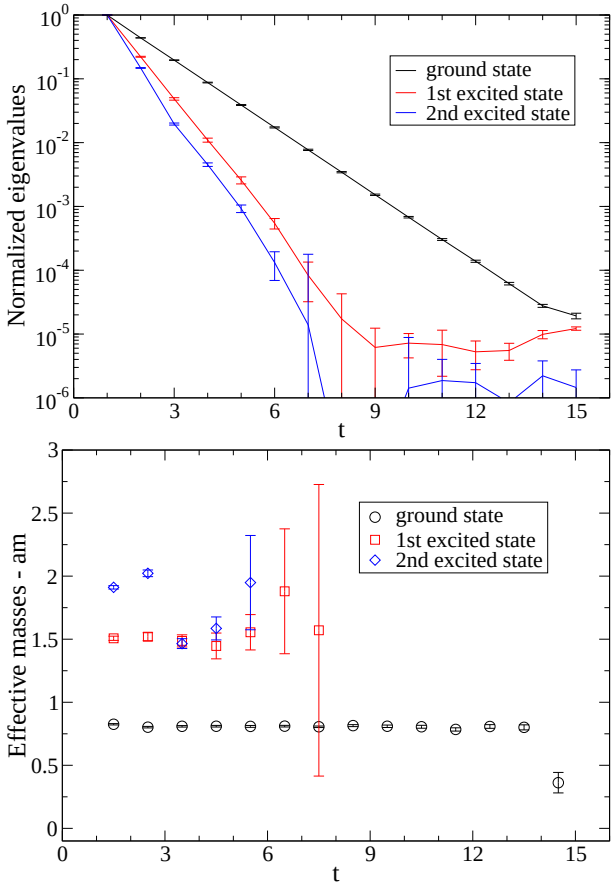

Figure 3.2: Upper plot: The three smallest eigenvalues from a 4×4 matrix of vector meson correlators. Lower plot: Corresponding effective masses. The plateaus for the excited states are clearly visible but rather short. The data is taken from the quenched simulations of Section 4.2.

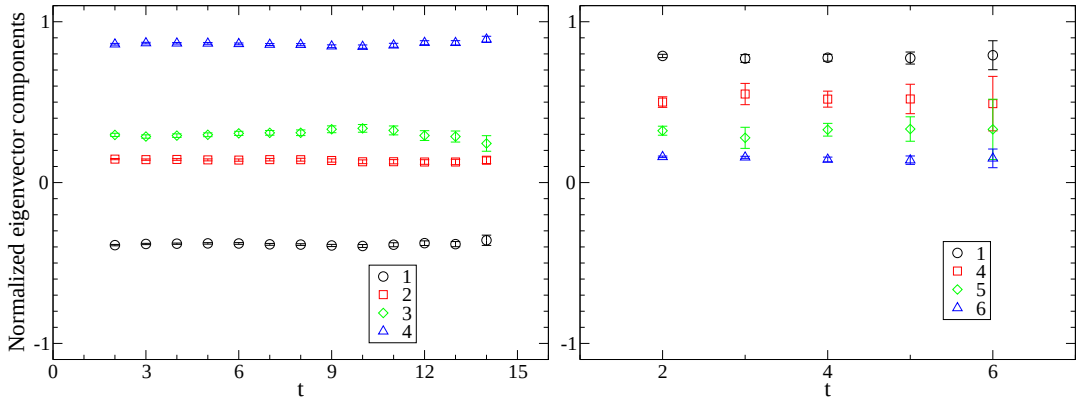

Figure 3.3: Eigenvector components corresponding to the ground state (left-hand side) and to the second excited state (right-hand side) from Figure 3.2. Clear plateaus can be observed in the range of the mass plateaus. The eigenvector components at $t_0 = 1$ are omitted as they are arbitrary.

one should also observe a plateau in the components of the eigenvectors $\psi^{(k)}$. To illustrate this, we plot the eigenvector components of the ground and second excited state corresponding to the data from Figure 3.2 in Figure 3.3. We now describe the fitting techniques employed in subsequent chapters for fits to the eigenvalues. The simplest type of fits are two parameter fits $Ce^{-(t-t_0)m}$ to the eigenvalues of the generalized eigenvalue problem, where m is the resulting energy and C is a pre-factor. To obtain an estimate of the statistical errors we follow two approaches.

- **Uncorrelated fits:** We perform simple two parameter fits to the eigenvalues, weighting each point by its error as determined from a single-elimination jackknife procedure.
- **Correlated fits:** For these fits we take into account autocorrelation[3] in Euclidean time t. The method we usually use has been described as "*Jackknife reuse*" in reference [95][4]. To estimate the covariance matrix we use the following Jackknife-estimate:

$$\mathrm{Cov}(t,t') = \frac{N-1}{N}\sum_{i=1}^{N}\left(\bar{\lambda}^{(i)}(t)-\bar{\lambda}(t)\right)\left(\bar{\lambda}^{(i)}(t')-\bar{\lambda}(t')\right) \ ,$$

  where (i) denotes the i-th jackknife block and the bars denote averages. For noisy data the covariance matrix may have artificially small eigenvalues and the correlated fits may break down. We usually restrict the covariance matrix to the region between t_0 and the end of the fit range.

When stable correlated fits are possible, the χ^2/d.o.f. can be used as another criterion to determine suitable fit ranges. For larger data sets, this is much more reliable than a simple visual inspection of effective masses and eigenvector components. In addition to these fits, a more complicated functional form has been used in [9], where scattering states are present. Some of these results will be presented in Section 4.4.

3.5 Angular momentum on the lattice

While it is simple to write down lattice expressions with the desired behavior under parity transformation and charge conjugation, the lattice breaks the continuous rotational symmetry explicitly and we will have to work with the symmetry group of the lattice. In this section, we will briefly discuss this issue on the example of meson interpolators. For a more detailed account, the reader is referred to [82] and for the group theory basics to [96].

For mesons we deal with the octahedral group O and therefore with five irreducible representations A_1, A_2, T_1, T_2 and E, each of them containing an infinite number of continuum spins. Table 3.1 lists the lowest few continuum spins in each irreducible representation along with the dimensionality of the lattice representations. Notice that spins 0 and 1 only occur in the A_1 and T_1 representations while the higher spins listed occur in multiple representations. The last column of the table also lists the Dirac structures belonging to the A_1 and T_1 representations.

[2] A similar prescription can be extracted from [94].

[3] The autocorrelation we take into account is due to correlations within each configuration and is not to be confused with autocorrelation resulting from Monte-Carlo simulations, which we will comment on in Chapter 4.

[4] Notice that all methods described in [95] should agree for large enough sample sizes. For small samples one may correct the error from the method of choice using the formulas provided in the reference.

Irrep of O	Dimension	J	Spinors in irrep
A_1	1	0,4,...	$\mathbb{1}$,γ_t,γ_5,$\gamma_t\gamma_5$
A_2	1	3,6,...	
E	2	2,4,5,...	
T_1	3	1,3,4,5,...	γ_i,$\gamma_t\gamma_i$, $\gamma_5\gamma_i$,$\gamma_t\gamma_5\gamma_i$
T_2	3	2,3,4,5,...	

Table 3.1: Irreducible representations of the octahedral group and lowest continuum spins in each irreducible representation.

One possible approach to disentangle contributions of different continuum spin J to the same interpolators consists of identifying degeneracies in different irreducible representations. As an example, degenerate states in the E and T_2 representations would be an indication for a spin 2 state, but not for a spin 3 state. Considering that a lot of experimental states are almost degenerate themselves (especially when one looks at high excitations) this is not a straightforward task in many cases. In dynamical simulations, the situation is even worse, as scattering states may be present. Therefore degenerate states alone are not a suitable criterion for the spectroscopy of excited states. It will therefore be crucial to look at the overlap between certain correlators and the respective state at different values of the lattice spacing or to identify common couplings in the continuum limit [86]. A comparison with quenched studies may be helpful, as all observed mesons are stable in quenched simulations.

To extend this discussion to baryon interpolators one has to consider the double valued representations of the octahedral group O^D [97]. For details and the construction of specific baryon interpolators please refer to [97, 98].

3.6 A suitable basis for the variational method

To obtain a suitable basis for the variational method, we have to construct interpolating operators which create and destroy particles with definite quantum numbers and have an improved overlap with the physical states of interest. In this section, we focus on possible ways to construct meson interpolators with the correct quantum numbers. Relevant literature for baryons is also discussed briefly.

3.6.1 Construction from displaced quarks

In this approach one uses quark sources placed at different lattice sites which are then connected in a gauge invariant way by suitable paths of links. The paths are chosen to obtain both a definite irreducible representation and a definite behavior under parity transformations and charge conjugation. For simplicity, we will again focus on mesons in our examples. In addition to straight paths, one can use L- and U-shaped paths [99] as well as closed path consisting of full plaquettes [82]. While this last approach [82] may not be the most realistic (both quarks sit essentially at the same point), it has the advantage that only one set of quark propagators is needed to access all irreducible representations. One then proceeds to combine these paths with suitable Dirac matrices into bilinears belonging to a specific lattice representation. Notice that multiple representations can

be reached with a certain combination of path and Dirac matrix. Consider for example

$$T_1 \otimes T_1 = A_1 \oplus E \oplus T_1 \oplus T_2 \ .$$

Therefore, with similar Dirac structures and the same sort of displacements one can create meson interpolators of various continuum spins. A similar approach has also been used to classify baryon interpolators [98, 97] and has subsequently been applied to baryons by the LHP Collaboration [87, 88, 89, 90]. In general this approach is also combined with *quark smearing*, which plays an essential role in the second approach described below.

3.6.2 Construction with smeared quark sources

In the second approach, extended sources are created by quark smearing of point sources. Such smeared sources have been widely used in the literature to minimize the contributions of excited states to the ground state. In the context of excited state spectroscopy, quark smearing is used to construct sources which have good overlap with the ground state but also with the lowest excitations. In [83, 84, 85] Jacobi-smearing [100, 101] is used to create Gaussians of different widths for meson and baryon spectroscopy involving light quarks. One starts with a point source

$$S_0^{(\alpha,a)}(\vec{y},t)_{\rho,c} = \delta(\vec{y},\vec{0}\,)\delta(t,0)\delta_{\rho\alpha}\delta_{ca} \ , \tag{3.12}$$

and applies N iterations of the smearing operator H

$$\begin{aligned} S^{(\alpha,a)} &= \sum_{n=0}^{N} \kappa^n H^n S_0^{(\alpha,a)} \ , \\ H(\vec{x},\vec{y}) &= \sum_{i=1}^{3} \Big(U_i(\vec{x},0)\delta(\vec{x}+\hat{i},\vec{y}\,) + U_i(\vec{x}-\hat{i},0)^\dagger \delta(\vec{x}-\hat{i},\vec{y}\,) \Big) \ , \end{aligned} \tag{3.13}$$

with a suitable weight κ. This type of smearing has two parameters, κ and N, and leads to gauge covariant, approximately Gaussian shaped sources. The parameters used for the runs with dynamical CI fermions are listed in Table C.2 in the appendix. A slightly different type of Gaussian smearing has been used in [86] and will be used in Chapter 5. More recently, a similar approach has been used in [93] to study the Roper resonance[5].

One can extend this approach by applying covariant lattice derivatives to Gaussian smeared sources to construct smearings belonging to different irreducible representations. This approach has been pursued for charmonium in [102, 86] and has also been applied to light-quark spectroscopy of $J = 0, 1$ states in [3]. More recently, results for higher spin mesons have been presented in [92] and some of our results will appear in [8]. The covariant derivative is usually implemented with a symmetric nearest neighbor construction:

$$P_i(\vec{x},\vec{y}) = \frac{U_i(\vec{x},t)\delta(\vec{x}+\hat{i},\vec{y}\,) - U_i(\vec{x}-\hat{i},t)^\dagger \delta(\vec{x}-\hat{i},\vec{y}\,)}{2} \ . \tag{3.14}$$

In Chapter 4 we apply such covariant derivatives P_i to our wide Gaussian sources S_w to obtain derivative quark sources

$$W_{\partial_i} = P_i S_w \ . \tag{3.15}$$

[5] We briefly review the current status of the Roper resonance on the lattice in Chapter 6.

Once a quark smearing which leads to a certain irreducible representation is defined, one proceeds similar to the first approach by combining quarks with the given smearing with combinations of Dirac matrices to obtain interpolators of a given PC transforming according to the representation of choice. In Appendix A.1 we list interpolators of various irreducible representations R containing quantum numbers R^{PC} which are used for meson spectroscopy in Chapters 4 and 5.

3.6.3 Gauge link smearing

For both methods of constructing interpolators, it is advisable to use smeared links when constructing hadron sources and sinks. Once the quark sources are generated, the unsmeared gauge fields are used for the calculation of quark propagators. In the case of CI simulations with dynamical quarks, the Chirally Improved Dirac operator is defined with one level of stout smearing [103] in the action. Our ground state results presented in [5] have been obtained with no additional link smearing. For more recent results, we also use a three-dimensional smearing prescription to create the sources and sinks. To keep the smearing local, we opted for 3-dimensional HYP-smearing [104]. As observed previously by other authors [89], this considerably reduces the statistical uncertainty on a given number of configurations [105]. Therefore, three levels of hypercubic smearing with the parameters listed in Appendix C are used for the results presented in Section 4.3 and in Chapters 6 and 7.

3.7 All-to-all propagators and new developments

For the calculation of *disconnected diagrams*, which play a role for isoscalar quantities, different methods have to be used. Here, the full propagators have to be estimated using so called *all-to-all* techniques. In addition, we will briefly describe a recent new proposal [106] for constructing quark sources which may lead to smaller statistical errors in some cases and which is in general more versatile.

3.7.1 All-to-all propagators

While an exact calculation of all-to-all propagators is not possible, stochastic estimation techniques can be used to estimate the full quark propagator which are needed for the calculation of disconnected diagrams. A state-of-the art approach for all-to-all propagators can be found in [107]. For completeness, we describe this method briefly. For the details please refer to [107] and references therein.

The method consists of multiple parts. The first part is given by a standard noisy estimator technique. The Dirac operator is inverted on a set of noise vectors $\eta_{(r)}$ to obtain an estimate for the full propagator

$$D^{-1}(x,y)^{ij}_{\alpha\beta} = \lim_{N\to\infty} \frac{1}{N} \sum_{r=1}^{N} \psi^{i\alpha}_{(r)}(x) \eta^{j\beta}_{(r)}(y)^{\dagger} \ , \tag{3.16}$$

where $\psi_{(r)}$ are the solutions corresponding to the source vectors $\eta_{(r)}$. This method is further improved by working with *diluted* noise vectors which have support on only part of the lattice. In [107], color, spin, time and even/odd dilution are suggested. The second part of the method consists of an exact treatment of the low-lying modes of the four-dimensional Dirac operator. After calculating these eigenmodes, only the remaining part of the quark propagator is estimated using above noisy estimator techniques with diluted noise vectors.

3.7.2 A new type of quark sources

Recently, the Lattice Hadron Physics Collaboration suggested a new and promising method [106] for creating smeared quark fields. The basic observation is that only a small number of lowest eigenmodes of the lattice Laplace operator ∇^2 contributes significantly to their construction of sources J, which are defined to obey

$$\lim_{N\to\infty} J_{\sigma,N}(t) = \exp\left(\frac{\sigma^2\nabla^2(t)}{4}\right) \ . \tag{3.17}$$

They therefore use a truncation of the lattice Laplacian to the lowest few modes to approximate the smearing operators. They proceed to define the *distillation operator*

$$\Box(t) = V(t)V^\dagger(t) \tag{3.18}$$

where $V(t)$ is the matrix of lowest eigenmodes of the lattice Laplace operator. This distillation operator is used to create the quark sources. To construct arbitrary isovector two-point functions, the quantities

$$\tau_{\alpha\beta}(t',t) = V^\dagger(t')D^{-1}_{\alpha\beta}(t',t)V(t) \ , \tag{3.19}$$

need to be calculated. This requires $4 \times N$ inversions of the Dirac matrix, where N is the number of modes used for the construction of the distillation operator. Let us summarize the merits of this approach:

- The sources created with the help of the distillation operators $\Box(t)$ have support in the whole timeslice. This has two benefits: First, a momentum projection is possible not only at the sink but also at the source. Secondly, the links in the immediate vicinity of the source location strongly influence the shape of the final quark sources in the conventional approach. This problem should not exist for this new method.

- The choice of source and sink operators is independent of the calculation of $\tau_{\alpha\beta}(t',t)$. Once the whole set has been calculated, it can be used for various different interpolator constructions. The width of the sources can also be varied by introducing weight factors in the definition of the distillation operators.

- Three-point functions can be constructed by calculating two sets of propagators, one set from the source-location and one set from the sink location. This construction merely doubles the effort needed for the two-point functions. All propagators calculated for the two-point functions can be recycled and any momentum transfer should remain accessible.

- For small lattices, a small number of eigenmodes (i.e. roughly 32) of the three dimensional Laplace operator seems to be sufficient [106]. The resulting number of inversions is then of the same magnitude as it is for usual calculations of excited states.

While the advantages of this new approach are clear, detailed comparisons of both methods should be performed. One potential problem is that the number of eigenmodes needed grows linearly with the number of lattice points in the three-volume. While a direct calculation of disconnected diagrams within this method would require one set of propagators on *each* timeslice, a method similar to the all-to-all method described in the

previous section can be used to estimate the contributions that are not treated exactly with the distillation method.

As a last comment, we would like to point out, that the Incremental EigCG-Inverter [108] described in Appendix D is especially well suited for practical calculations with the methods described in this section, as the Dirac matrix D needs to be inverted for many right-hand sides.

Chapter 4

The spectrum of light-quark mesons

In this chapter we give an overview of light meson spectroscopy with Chirally Improved valence quarks on both quenched and dynamical CI lattices. In the first section, we discuss a basis of meson interpolators containing derivative quark sources. We then present results from a quenched study for ground and excited state mesons in 4.2. In Section 4.3, we take a look at the meson spectrum using both Gaussian smeared and derivative quark sources on lattices with dynamical sea quarks. For the dynamical lattices, we also present some results for higher spin and exotic states. We attempt a naïve chiral extrapolation of some of the results and compare these to a previous quenched study and to experimental meson states. Finally, in Section 4.4, we present an alternative basis of tetraquark interpolators and study the spectrum of scalar tetraquarks.

Ignoring the possibility of tetraquark states for now, a general meson correlator can be written as

$$O = \bar{q}_s \Gamma q_s \ , \tag{4.1}$$

where Γ is a single Dirac matrix or a combination of Dirac matrices, the quarks q can in general be different quarks and the index s indicates a general smearing as introduced in 3.6.2. Neglecting the smearing indices s for a moment, isotriplet correlators built from such interpolators are given by[1] (see for example [18])

$$\begin{aligned} \left\langle O(n)\bar{O}(m)\right\rangle_F &= \left\langle \bar{d}(n)\Gamma u(n)\bar{u}(m)\Gamma d(n)\right\rangle_F \\ &= \Gamma_{\alpha_1\beta_1}\Gamma_{\alpha_2\beta_2}\left\langle \bar{d}(n)_{\alpha_1,c_1}u(n)_{\beta_1,c_1}\bar{u}(m)_{\alpha_2,c_2}d(m)_{\beta_2,c_2}\right\rangle_F \\ &= -\Gamma_{\alpha_1\beta_1}\Gamma_{\alpha_2\beta_2}\left\langle u(n)_{\beta_1,c_1}\bar{u}(m)_{\alpha_2,c_2}\right\rangle_u \left\langle d(m)_{\beta_2,c_2}\bar{d}(n)_{\alpha_1,c_1}\right\rangle_d \\ &= -\Gamma_{\alpha_1\beta_1}\Gamma_{\alpha_2\beta_2}D_u^{-1}(n|m)^{\beta_1\alpha_2}_{c_1c_2}D_d^{-1}(m|n)^{\beta_2\alpha_1}_{c_2c_1} \\ &= -\mathrm{tr}[\Gamma D_u^{-1}(n|m)\Gamma D_d^{-1}(m|n)] \ . \end{aligned} \tag{4.2}$$

Here D_q^{-1} stands for the quark propagator of a quark with flavor q. To see that it is sufficient to calculate only one set of propagators for each source smearing, one can use the γ_5-hermiticity of the Dirac operator

$$D_q^{-1}(m|n) = \gamma_5 D_q^{-1\star}(n|m)\gamma_5 \ ,$$

thereby getting rid of the backwards running propagator. This computational trick enables us to sum over all sites at the sink timeslice, performing a momentum projection to momentum zero as needed for meson spectroscopy.

[1] For concreteness we use u and d for the quark flavors in this example.

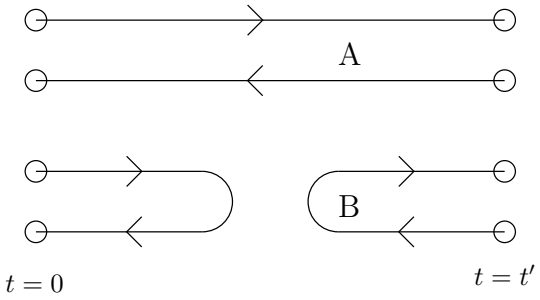

Figure 4.1: This figure illustrates the quark lines for connected (A) and disconnected (B) contributions.

While this is the simplest case, additional *disconnected* contractions of the type $\mathrm{tr}[\Gamma D_u^{-1}(n|n)]\mathrm{tr}[\Gamma D_d^{-1}(m|m)]$ occur for isosinglet mesons. These terms are very hard to compute and all-to-all methods (for a short introduction see Section 3.7) are needed to compute such disconnected contributions. We therefore restrict ourselves to the calculation of isovector quantities for most of our calculations. Figure 4.1 shows an illustration of connected and disconnected contributions. As the mass splitting between up and down quarks is small compared to the quark masses employed in our calculations, we consider up and down quarks to be mass-degenerate, $m_u = m_d$.

4.1 Light-quark spectroscopy with derivative quark sources

For the Variational Method described in Section 3.3, it is crucial to use a basis of interpolators which have good overlap with the ground and lowest excited states in the given channel. One possibility to construct a basis consists of using Gaussian sources of different width [84]. As described in Section 3.6.2, this approach can be extended with sources containing derivatives [3]. In the following, we use a basis of both Gaussian and derivative sources for the spectroscopy of light-quark mesons.

Tables A.1 and A.2 in Appendix A.1 show the interpolators used[2] in [3]. For consistency, the interpolators are not numbered consecutively but according to their structure. Numbers 1-6 denote the Jacobi-smeared interpolators of [84], while all other interpolators contain at least one derivative. For all of our plots in this chapter we will refer to these numbers in combination with the quantum numbers of the channel to uniquely identify the correlators.

For non-strange mesons, an anti-symmetrization of the interpolators is used to obtain a definite behavior under charge conjugation. While we make this symmetrization explicit in Tables A.1 and A.2, we will sometimes omit it later on. Nevertheless, interpolators containing a single derivative denoted as $\bar{u}_{\partial_i}\Gamma d_{n/w}$ should always be read as $\bar{u}_{\partial_i}\Gamma d_{n/w} - \bar{u}_{n/w}\Gamma d_{\partial_i}$. In Chapter 5 we discuss why a symmetrization is needed even at zero momentum and present a way to avoid this symmetrization. Similar interpolators will be used in Section 4.3 on configurations with dynamical CI quarks, where we further extend the basis and also take a look at strange-light mesons.

All interpolators have been classified with regard to continuum quantum numbers $I\ J^{PC}$. In [3], the quantum numbers in the chiral limit are also discussed. As usual, P denotes the spatial parity, J is the total continuum spin, I is the isospin and C denotes

[2]The tables also contain additional interpolators which will be used in 4.3.

the behavior under charge conjugation of the neutral $\bar{q}q$ system. As detailed in Section 3.5, the lattice interpolators in A.1 will in general also couple to continuum states with higher J due to the loss of rotational symmetry [99, 86]. We will point out where such an admixture may play a role in the identification of states. For the case of spin 2 mesons on dynamical lattices we explicitly construct correlators belonging to distinct irreducible representations.

4.2 Results from quenched QCD

In [3] derivative quark sources were used for a study of the light-quark meson spectrum. In particular, the pseudoscalar, scalar, vector and pseudovector channels were investigated. In this section, we summarize the most important findings of [3] and provide an overview of the method.

4.2.1 Technicalities

We work on a set of 99 uncorrelated quenched gauge configurations generated with the Lüscher-Weisz gauge action [20, 109]. We use a $16^3 \times 32$ lattice with a lattice spacing of 0.148 fm, determined [110] from the Sommer parameter (using $r_0 = 0.5$ fm). We study several valence quark masses ranging from $am_q = 0.02$ to $am_q = 0.2$. We fold the data obtained from propagation in positive and negative Euclidean time and subsequently determine the errors with a single elimination jackknife procedure. In addition to the purely statistical error, we also provide a rough estimate of the systematic error from varying the fit range and from altering the choice of interpolating field operators. This systematical error is indicated by a shaded area in the plots. The horizontal error bars in the plots over the pion mass squared m_π^2 are from the uncertainty in the determination of m_π. For most of the results in this section, we use uncorrelated fits (see Chapter 3), which usually leads to an unrealistically small χ^2/d.o.f. (for tables see [110]) and an overestimation of the statistical error.

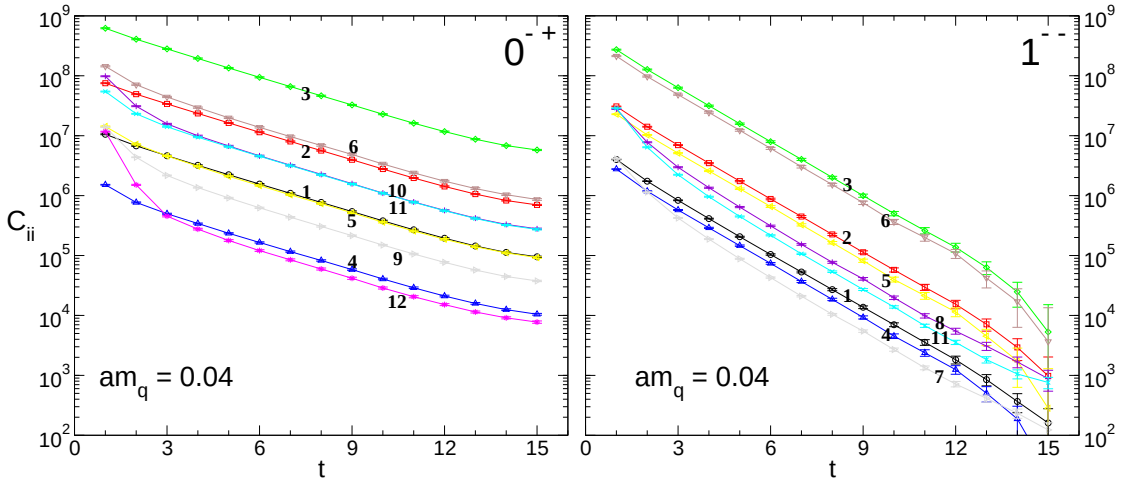

Figure 4.2: Diagonal entries of the correlation matrix as a function of Euclidean time t. The data are for bare quark mass $am_q = 0.04$. The 0^{-+} (left-hand side plot) and 1^{--} (right-hand side) channels are shown. The numbers next to the correlators are according to Tables A.1 and A.2 respectively.

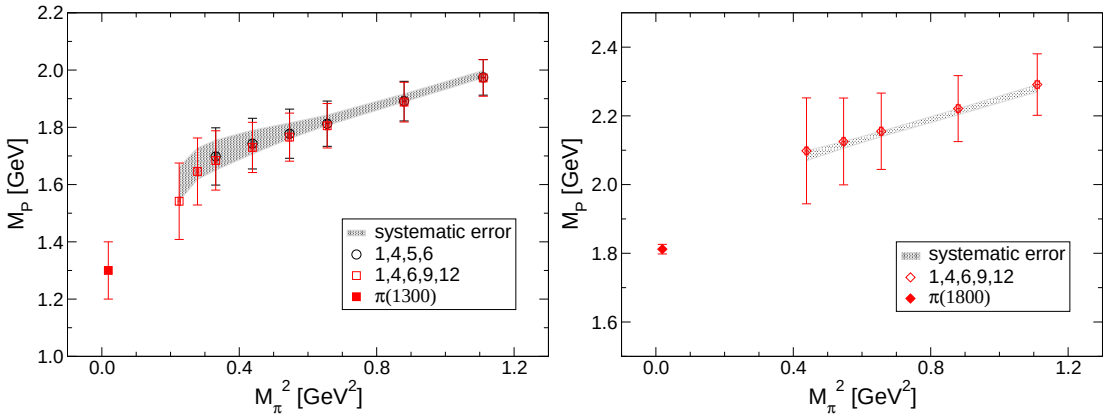

Figure 4.3: Left-hand side: First excited state of the pseudoscalars for two different sets of interpolators. Right-hand side: Second excited state for the pseudoscalars. The error bars are statistical only and the shaded regions indicate the additional systematic errors. The filled symbols correspond to the experimentally measured resonances $\pi(1300)$ and $\pi(1800)$.

4.2.2 A first look at our quark sources

To illustrate the effect of using derivative sources, we show the diagonal correlators for the 0^{-+} and 1^{--} channels in Figure 4.2. Compared to Gaussian sources, the interpolators with derivative sources show stronger contributions from excited states, which can be deduced from the steeper slope at small timeslices. At large Euclidean time t, it can nevertheless be clearly seen that all diagonal correlators are eventually dominated by the respective ground states.

4.2.3 The 0^{-+} channel

In Figure 4.3, we display the results for the first and second excited states of the pion. On the left-hand side the first excitation is extracted from two different sets of interpolators. Circles are used for the combination of Gaussian interpolators 1, 4, 5, 6, while the squares correspond to the choice 1, 4, 6, 9, 12 of Gaussian and derivative interpolators. The latter allow for fits at slightly lighter quark masses. At the same time, the interpolators with derivative sources couple weaker to the ground state. The systematical uncertainty (shaded region in the figure) from the choice of interpolators is consistent with statistical effects as reasonable combinations of four or more interpolators always lead to comparable results. While there is no significant improvement, the new results with the enlarged basis nicely confirm the existence of the measured state and the statistical error for the first excited state shrinks as the derivative interpolators are added to the basis.

It is also worth mentioning, that contributions from the ground state propagating back in time spoil the signal of the first excited state at small quark masses and limit the usefulness of the variational method for fits of the ground state pion [3]. We will illustrate this effect in Section 4.3, where it turns out to be a severe limitation for the extraction of excited pion states. Similar effects have also been observed previously in [89].

On the right-hand side of Figure 4.3, we display our results for the second excitation of the pion. Unlike with Gaussian sources alone, it is possible to obtain fits for this

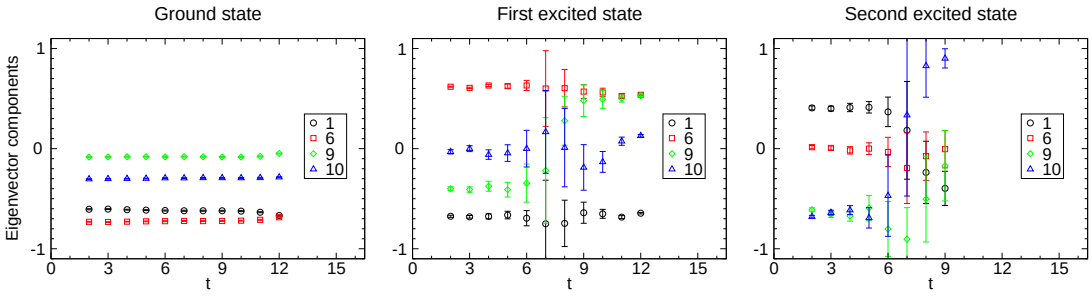

Figure 4.4: Eigenvector components from the standard eigenvalue problem (Equation 3.9) as a function of t. The eigenvectors correspond to the pion ground state (left-hand side plot), the first and second excited states (center and right-hand side plots) and are obtained from a 4×4 matrix of the interpolators 1, 6, 9, 10, at quark mass $am_q = 0.12$.

second excitation with a combination of Gaussian and derivative interpolators. In the chiral limit, this state can most likely be identified with the $\pi(1800)$. Fits with various different combinations of interpolators lead to the same results, which all show stable eigenvector entries. We would like to stress that a correlation matrix of the same size consisting solely of non-derivative operators does not enable us to see this excitation.

It is instructive to look at the components of the eigenvectors for all three states observed in the pseudoscalar channel. Figure 4.4 shows such a plot for the case of interpolators 1, 6, 9 and 10. While the derivative interpolators 9 and 10 do neither contribute significantly to the ground state nor to the first excited state, they are most important for obtaining the newly observed second excited state. The good overlap of the derivative sources with the second excitation explains why we could not observe it with Gaussian sources alone. This behavior is qualitatively the same for all possible combinations of interpolators, for which the second excited state can be seen.

4.2.4 The 0^{++} channel

In the 0^{++} channel, contributions from so-called *ghost states* [111, 112, 113, 114, 115, 75] complicate the analysis. For light quarks, these unphysical quenching artifacts dominate the correlators at small Euclidean time separation and lead to correlators becoming negative at intermediate time separations. This effect is demonstrated in Figure 4.5, where diagonal correlators for the 0^{++} channel are shown. The contributions from ghost states seem to vary greatly, depending on the structure of the interpolator. In general, they seem to be much milder for interpolators containing derivative quark sources. From the analysis of the dynamical CI data presented in Section 4.3, we will see that interpolators 7 and 8, which lead to a good signal in the quenched case, show only a very weak signal in the case of dynamical mesons. While, for a pure $\bar{q}q$ system, these interpolators should not couple to scalar mesons in the chiral limit [3], this is a puzzle we do not fully understand.

Most of the ghost contributions can be separated by the variational method [113]. Nevertheless the signal becomes very noisy when these ghost contributions set in and a reliable fit is no longer possible.

In Figure 4.6 we present our results for the ground state of the isovector scalar a_0. Compared to a basis of Gaussian sources alone, we are able to perform fits at smaller quark masses and with increased statistical accuracy (for the intermediate and larger

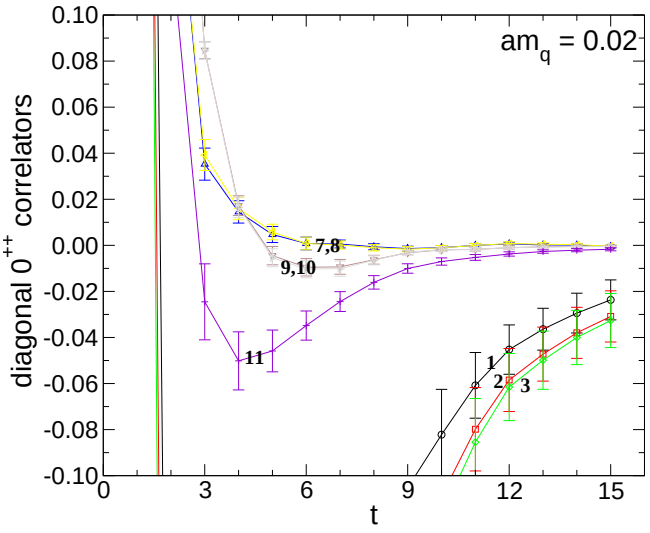

Figure 4.5: Diagonal entries of the correlation matrix for the scalar channel at $am_q = 0.02$. The numbers next to the data label the correlators according to Table A.1. There are clear contributions of ghost states for some interpolators (i.e., negative values), while other interpolators seem to be almost free of them.

quark masses). An extrapolation of the quenched data to the chiral limit[3] is difficult, as there is a large dependence of the results on the interpolators used. While interpolators with large ghost contributions suggest an extrapolation to the $a_0(1450)$, some of the derivative interpolators lead to values in the lower part of the shaded region. As we will see in Section 4.3, some of this ambiguity will persist even in the case of dynamical simulations. Nevertheless, there are some arguments speaking for an extrapolation to the $a_0(980)$ which we will discuss in 4.3.

For a general description of the puzzles associated with low lying scalar mesons, see Section 4.4 and references [116, 117].

4.2.5 The 1^{--} channel

The ground state in the vector meson channel is given by the $\rho(770)$. While this state can be fit from single correlators the results improve quite drastically when a matrix of interpolators is used. Figure 4.7 shows the ground state, which is of good quality in the quenched approximation where decays are absent. As usual the grey error band indicates the systematic uncertainties from the choice of different interpolators and fit ranges. In this case, the error is dominated by the statistical error. A naïve linear (in m_π^2) extrapolation leads to masses somewhat higher than the ground state. We will revisit this issue when analyzing data from dynamical configurations.

In addition to the ground state, two more energy levels can be extracted whose interpretation in terms of physical particles is less obvious. While there are multiple known excitations with $J = 1$ below 2 GeV (most notably the $\rho(1450)$ and the $\rho(1700)$) there is also at least one excitation with $J = 3$ (the $\rho_3(1690)$) in this mass range. As mentioned in 3.5, the loss of continuous Lorentz symmetry implies that lattice interpolators may also couple to higher spins. More specifically, at any finite lattice spacing coupling to

[3] We refer to the limit of the pion mass going to the physical pion mass as the chiral limit, even though the real chiral limit is given by a massless pion.

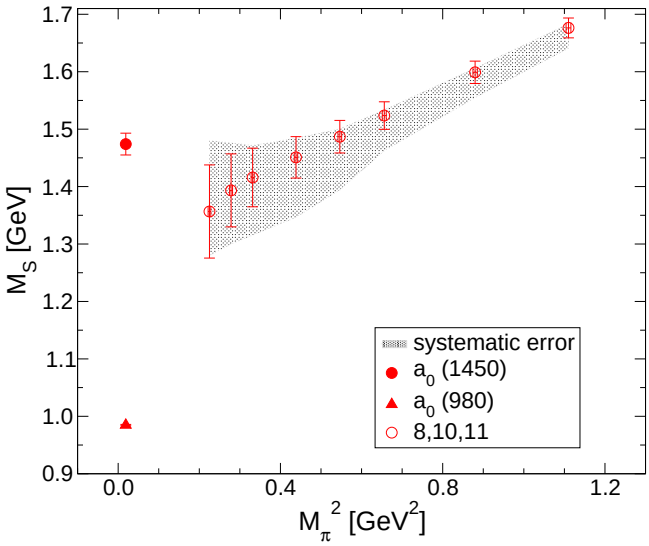

Figure 4.6: Ground state mass of the isovector scalar (a_0). The error bars are statistical only and the shaded region indicates the additional systematic error described in the text. The black circle shows the (experimentally) measured $a_0(1450)$ and the triangle indicates the $a_0(980)$.

states with $J = 3$ is not excluded for interpolators in the T_1 irreducible representation.

Figure 4.8 shows the results for the first and second excited states in the 1^{--} channel. Overall, results from a combined basis of Gaussian and derivative interpolators agree qualitatively with results obtained from just Gaussian interpolators alone. At the same time, the larger basis leads to smaller error bars and more stable plateaus enabling us to perform fits at slightly lower valence quark masses. The observed excitations are rather close together and are both consistent with the $\rho(1700)$. In [3] this has been attributed to discretization effects, as data from a finer $20^3 \times 32$ lattice with $a = 0.119\,\mathrm{fm}$ leads to two distinct excitations. This argument was supported by similar eigenvector

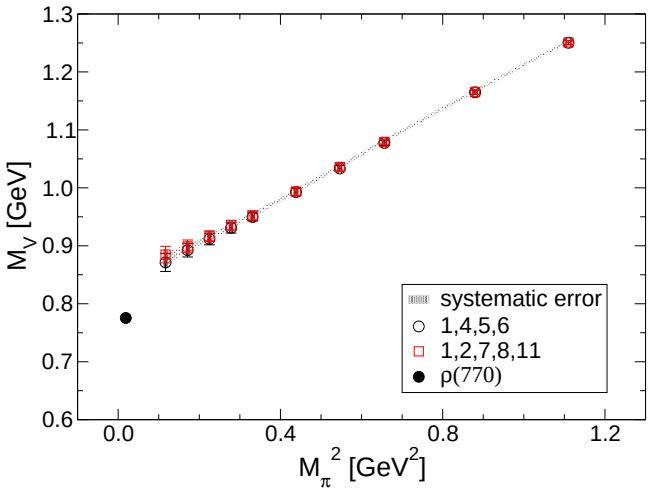

Figure 4.7: Ground state for the $\rho(770)$ meson.

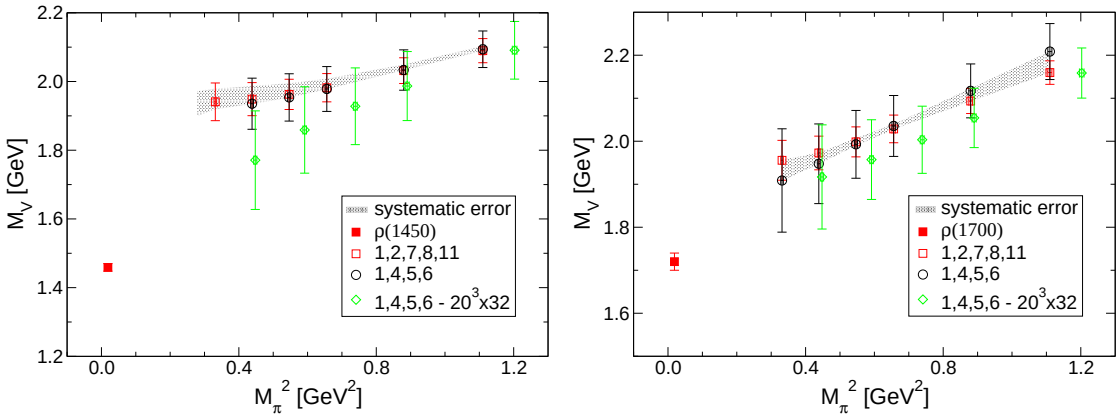

Figure 4.8: First (left-hand side) and second (right-hand side) excited states of the vector mesons compared to the experimental spin 1 resonances $\rho 1450$ and $\rho(1700)$. To illustrate possible discretization effects we also display data from [84] for a finer lattice of the same volume ($20^3 \times 32$, $a = 0.119$ fm).

components for both the coarse $16^3 \times 32$ and the fine $20^3 \times 32$ lattice. Newer data from configurations created with dynamical CI quarks [5, 8] (see Section 4.3) indicates that an unambiguous interpretation may require higher statistics as runs with the same lattice spacing at different quark masses reveal similar problems for the excitations of the ρ meson. This may be seen as a reminder that data obtained at different valence quark masses in a quenched simulation is highly correlated. Naïve extrapolations assuming an uncorrelated sample may therefore be dangerous. To settle these issues, more data points from dynamical simulations, preferably also at a finer lattice spacing, will be needed.

4.2.6 The 1^{++} channel

For the 1^{++} channel, there is only one interpolator containing derivative quark sources. Figure 4.9 shows data obtained from different combinations of Gaussian interpolators and the one containing derivatives. An indication of error bands, as shown for the other channels, has been omitted here, since the two combinations plotted already show the extremes.

For the 1^{++} pseudovectors, derivative sources drastically improve the signal for the ground state. While the results from the Gaussian and the full sets agree qualitatively, the statistical errors towards smaller quark masses are significantly reduced. The reason for this are longer, more stable effective mass plateaus allowing for larger fit ranges. At larger quark masses there is a slight deviation of the order of two standard deviations.

The excited state previously observed [84] stays the same if one includes the new interpolator in the analysis. Looking at the components of the modified eigenvalue problem we see that this interpolator contributes only weakly to the excited state. A matrix analysis therefore combines the advantages of both types of interpolators.

In Section 4.3 an enlarged basis of interpolators will be used for both the 1^{++} (or a_1) pseudovectors as well as the 1^{+-} (or b_1) pseudovectors. These results confirm the usefulness of derivative sources for spectroscopy of pseudovector mesons.

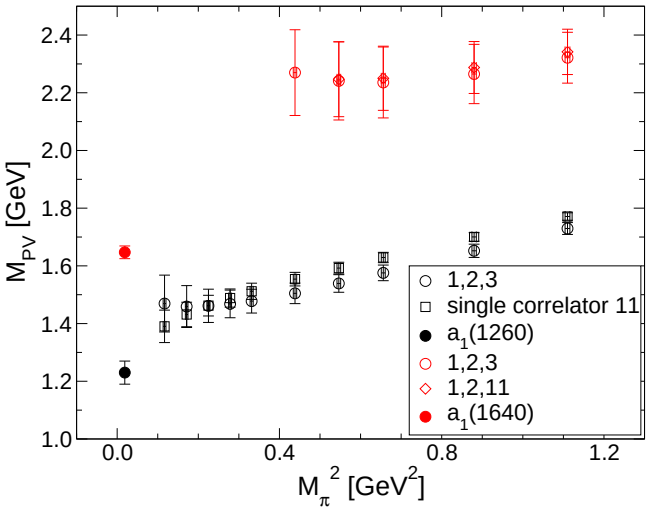

Figure 4.9: Ground- and first excited state of the pseudovector mesons (a_1). The filled circles indicate the physical states.

4.2.7 Summary of results from the quenched simulation

We explored the use of an enlarged basis of meson interpolators containing both Gaussian as well as derivative quark sources in light-quark meson spectroscopy. Depending on the channel, the determination of both ground and excited states may be improved by the use of derivative interpolators. For the 0^{-+} channel, a second excited state can be extracted that was not seen with a basis of similar size consisting of Gaussian sources alone. In the case of scalar mesons, interpolators with derivatives showed a reduced contamination from ghost states which enabled us to obtain fits at smaller quark masses. The results for the 1^{--} channel are fully consistent with previous results, while a larger basis can serve to reduce the statistical uncertainty. The most drastic improvement has been observed in the 1^{++} channel, where the ground state pseudovector a_1 could be extracted more reliably. In the next section, we will apply the same methods to data from dynamical CI simulations, where we will also explore additional channels including mesons with $J = 2$.

4.3 Results from dynamical CI simulations

Within the Bern-Graz-Regensburg Collaboration, lattices with dynamical CI quarks have been generated [5]. Currently, there are three ensembles on lattices with $16^3 \times 32$ lattice points with a volume of approximately $2.4\,\mathrm{fm}^3 \times 4.8\,\mathrm{fm}$. The pion masses range from 525 MeV (which we call "run A") down to 322 MeV ("run C"), which corresponds to quark masses m_{AWI} in a range $42 - 15\,\mathrm{MeV}$. For more details about ensembles with dynamical CI quarks please refer to Appendix C and to reference [5].

In this section, we will discuss results for meson spectroscopy on dynamical CI configurations. Our main focus will be on the derivative sources of [3], which we apply to the dynamical ensembles A-C. Selected results for the ground state masses employing standard Gaussian sources without additional gauge link smearing[4] have already been

[4]The Chirally Improved Dirac operator already contains one level of stout-link smearing. For more details refer to Section 3.6.3 and references therein.

presented in [5]. Here we mostly use results obtained from sources constructed with three levels of HYP-smearing [104]. We will indicate when we use results already presented in [5] instead. More recently, results for both ground and excited states have been reported in [8]. In addition, preliminary results have been presented in [6, 7].

For our spectroscopy calculations, propagators have been calculated on every fifth configuration. To further reduce the autocorrelation between subsequently analyzed configurations, we shift the sources through the lattice in a periodic fashion. For estimates of autocorrelation times in measurements of simple observables please refer to [5]. A reliable estimate of autocorrelation times for hadron masses would require a larger ensemble size. We therefore treat the chosen configurations as uncorrelated and determine the statistical errors with a single-elimination jackknife procedure.

4.3.1 Results for light-quark mesons

For the dynamical CI ensembles listed in Appendix C, we use a slightly enlarged basis of interpolators compared to the quenched case. We now use the full set of interpolators presented in Tables A.1 and A.2 for spin 0 and spin 1 mesons. Details on the quark smearing parameters for the dynamical configurations can be found in Table C.2.

Chiral extrapolations

Unfortunately, there are no results from Chiral Perturbation Theory to guide the chiral extrapolations for excited states. The same is true for most of the ground states considered in this section. In the absence of a better understanding, we will have to resort to phenomenological fits motivated from the fact that some states seem to exhibit a linear behavior in m_π^2 at low enough pion masses. We therefore use the form

$$m_H = c + b m_\pi^2 \tag{4.3}$$

for most of our chiral fits. Such fits have been used in the past for quenched results [84] and more recently also for the extrapolation of dynamical data [92].

The results obtained in this way should mainly serve to guide the eye as we currently do not have enough data points for reliable fits. In addition, the statistical errors associated with our limited data are large and a higher statistics would be beneficial to better constrain the fit parameters. In the future, we hope to add more data points and increase the statistics for some of our runs. Overall it is quite surprising how well the results of these simple extrapolations agree with the experimental data, especially if one considers that continuum and finite volume extrapolations are still lacking. We will discuss some of these shortcomings in the outlook presented in Chapter 8.

The 0^{-+} channel

We would like to start the discussion with the pion channel, where, for the ground state, the best signal can be extracted. Figure 4.10 shows the two largest eigenvalues as obtained from the variational method using the generalized eigenvalue problem compared to a single diagonal correlator $(\bar{q}_w \gamma_5 q_w)$ normalized at timeslice $t_0 = 1$. Neglecting wrap-around effects from the finite time extent of the lattice, these eigenvalues should correspond to the ground state and first excited state of the pion. As we work with a periodic lattice, this simple picture does not hold. For all three runs, the backwards running ground state is clearly visible in the data, starting between timeslice 5 and 8 depending on the pion mass. This backwards running ground state severely limits the fit

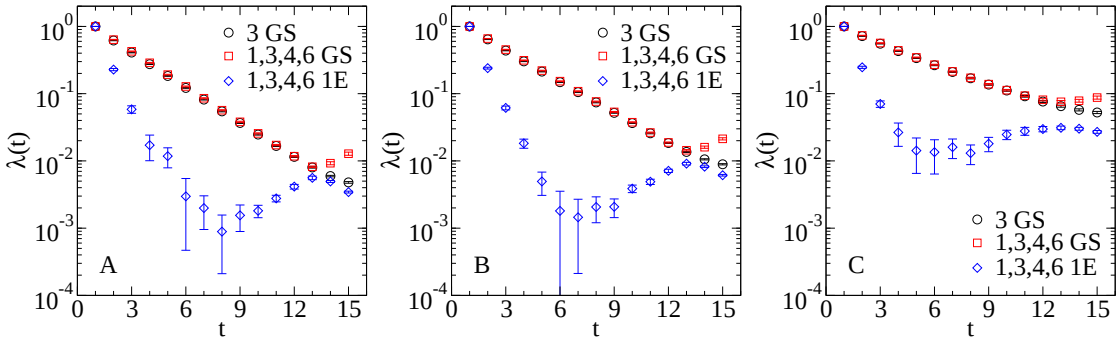

Figure 4.10: Eigenvalues for the ground and first excited states in the pseudoscalar channel. The open circles show a single diagonal correlator which exhibits the typical cosh type behavior expected for a periodic lattice. The eigenvalues from the generalized eigenvalue problem show a large contamination from the backwards-running ground state which is discussed in the text. The figure is taken from [5].

range for the first excitation. Notice that this can be remedied by a larger time extent of the lattice. Similar artifacts from the periodicity of the lattice have also been observed in channels where particles scattering back-to-back may be present [118]. These artifacts are discussed in detail in reference [9] and this effect may be an additional complication for dynamical simulations at light quark masses. We will come back to this observation when discussing the results for scalar mesons.

Figure 4.11 shows the results for the first excitation in the pion channel obtained from sources constructed with smeared links. The filled symbols are the results at the unitary points, where sea and valence quark masses are equal. The open symbols show partially quenched data with valence quark masses that are larger than the sea quark masses.

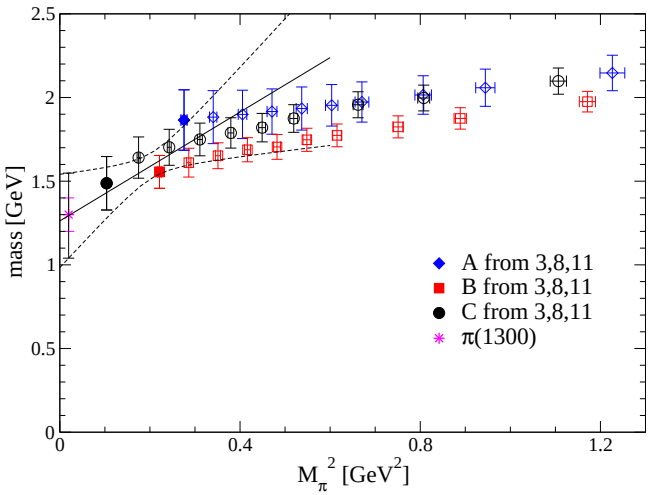

Figure 4.11: First excited state in the pion channel compared to the experimental $\pi(1300)$. The filled symbols are the dynamical points, while the open symbols are partially quenched results. The solid line denotes the fit to the three dynamical points and the dashed lines indicate the error of the fit. The data is taken from the talk corresponding to [8].

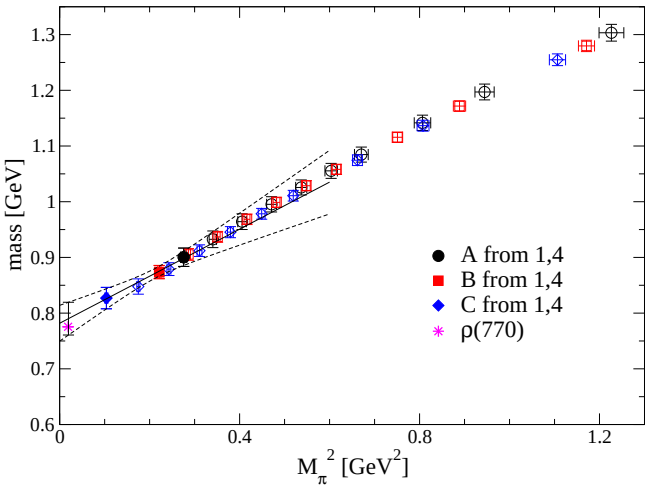

Figure 4.12: Ground state of the ρ meson. The filled symbols are the dynamical points, while the open symbols are partially quenched results. The solid line denotes the fit to the three dynamical points and the dashed lines indicate the error of the fit. The data is taken from the talk corresponding to [8].

Compared to the quenched case, the signal seems to be somewhat noisier, especially at larger quark masses. Notice also that runs B and C corresponding to the lightest two pion masses are from simulations on 200 configurations, while only 99 independent configurations have been used for the quenched results in Section 4.2. While our results have a large statistical uncertainty, we are able to extract the first excited state at pion masses which are lower than in the quenched case. For the larger masses, the quenched results agree nicely with the dynamical results and there is no indication for larger quenching errors. Notice also that the lattice spacing and volume are comparable to the quenched simulations.

In addition to the lattice data, we show the results of a naïve linear fit (see 4.3.1 for a short discussion) which is the solid line in Figure 4.11. The dashed lines indicate the associated error bars. As can be seen, the results agree with experiment but the remaining statistical and systematical errors are quite large.

At the light dynamical quark masses used for our simulations we are not able to obtain a signal for the second excitation which we saw in quenched calculations at large quark masses [3].

The 1^{--} channel

Let us now proceed with the ground state in the vector meson channel, which can be identified with the ρ meson. Figure 4.12 shows data for the ground state in the 1^{--} channel, the $\rho(770)$. At larger partially quenched quark masses the data from the three different runs falls on one curve. In this regime all data agrees well with the quenched results (not shown in the figure), although the error bars are larger for the dynamical data. While a linear fit to the quenched data from Figure 4.7 describes the data well in the whole range of quark masses, the resulting mass of 825 MeV turns out to be roughly 50 MeV larger than the experimental value. The data from dynamical simulations deviates from a purely linear behavior. A fit using just the three dynamical points is shown in the plot and the results agree with experiment within large error

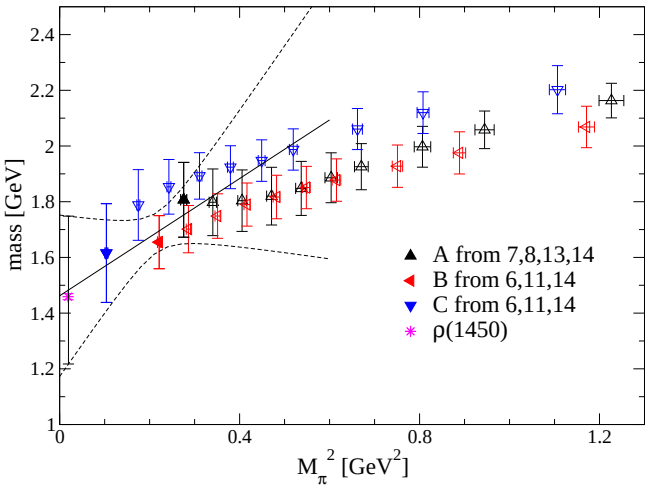

Figure 4.13: First excited state of the ρ meson. The symbols are the same as in Figure 4.12. The data is taken from the talk corresponding to [8].

bars. This is surprising, as the physical ρ meson is a resonance which can decay into two pions at small pion masses. This decay is a p-wave decay and we expect the ρ to be lattice-stabilized in a small volume, where the threshold for a decay at rest is given by $2\sqrt{m_\pi^2 + \left(\frac{2\pi}{L}\right)^2}$ [117], with the lattice size L.

Figure 4.13 shows the first excited state in the 1^{--} channel. Again the linear extrapolation leads to results compatible with the first known excitation, the $\rho(1450)$. In the quenched case, the data on the coarse lattice extrapolated to a value significantly above the physical resonance. This was attributed to discretization effects in [3]. The dynamical data on a similar lattice spacing and in a similar volume does not exhibit this behavior, but the statistical errors are large. More data would be needed to make a stronger statement.

The 1^{++} and 1^{+-} pseudovectors

In the pseudovector channels the situation is less clear. While the interpolators with Gaussian sources alone show a very weak signal, some of the derivative interpolators exhibit short but clear plateaus. At the same time, there is a large systematic uncertainty associated with the choice of interpolators. We therefore present two different fits in each channel to illustrate this error. For a more detailed analysis, more precisely to see if these systematic uncertainties persist with increased statistical accuracy, a larger number of configurations would be desirable.

Figure 4.14 shows the masses in the 1^{++} channel, which corresponds to the pseudovector meson $a_1(1260)$. We provide results for two different combinations of interpolators built from derivative sources. The left-hand side of Figure 4.14 shows results for interpolator 8 alone, while the right-hand side shows results from a matrix of interpolators 9 and 10. While the former extrapolate to a lower value which is more consistent with the experimental state, the latter extrapolate to slightly higher values. Nevertheless the final results agree within the large statistical errors.

In addition to the dynamical data, the quenched results from reference [3] are also shown on the left-hand side. While the dynamical results with interpolator 8 alone show a noticeable difference compared to the quenched results, the results from the new

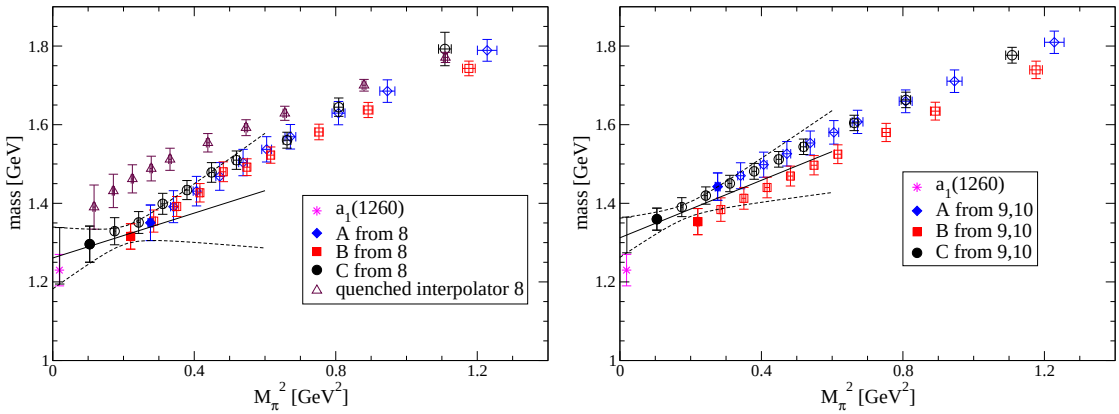

Figure 4.14: Ground state for the pseudovector mesons a_1 from two different interpolator combinations with derivative sources. For comparison we also show the physical $a_1(1260)$. While partially quenched points are denoted with open symbols, the filled symbols correspond to the unitary points (i.e. equal masses for sea and valence quarks). In addition to the data, a simple linear fit to the dynamical points is shown.

interpolators 9 and 10 agree qualitatively with the quenched results from 8. At large partially quenched masses, all sets agree within two standard deviations.

For the 1^{+-} pseudovector the situation is similar. In Figure 4.15 we again show two different sets of results, this time for interpolators 8 (left-hand side) and a matrix of interpolators 4, 5 (right-hand side) respectively. In addition the usual linear fits are shown and the results are compared to the lowest experimental state, the $b_1(1235)$. While the two sets agree qualitatively with an interpretation as the $b_1(1235)$, the results from interpolator 8 have much larger error bars. Also, when taking a matrix of all three interpolators, the results are very close to the results with just 4 and 5 alone, but the statistical errors grow. This indicates that other effects may lead to an artificially large mass for this state. Data at multiple different lattice spacings and possibly in multiple different volumes would be needed for a thorough investigation.

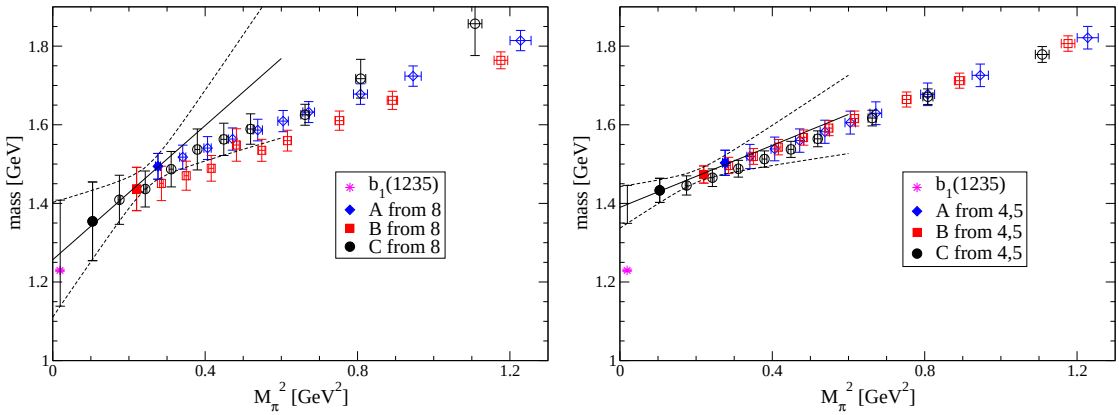

Figure 4.15: Ground state for the pseudovector mesons b_1 from different interpolator combinations with derivative sources. In addition to the lattice data, the experimental value for the $b_1(1235)$ is shown.

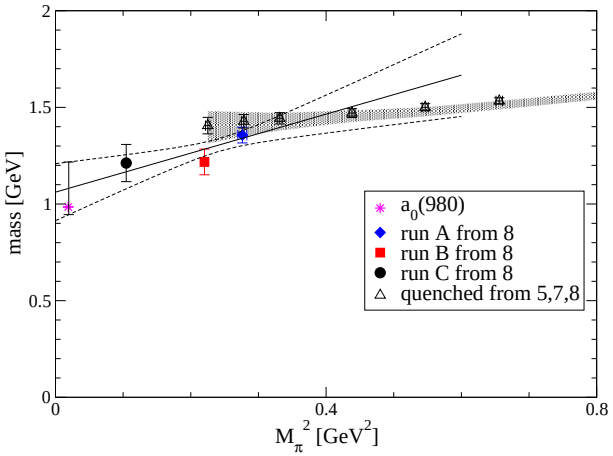

Figure 4.16: Ground state in the 0^{++} channel. The data points are from fits to the single interpolator 8. Most other interpolators either show no plateaus at all or produce inconsistent results. The linear fit seems to indicate an interpretation of the scalar ground state as the $a_0(980)$ which is shown for comparison.

We also want to point out, that the results from standard interpolators without derivatives agree qualitatively with the results for the b_1 while reliable fits for the a_1 were impossible. In general the associated mass plateaus were shorter and usually more noisy. Notice that the a_1 is a very broad resonance (with a width of 250 to 500 MeV [15]) and scattering states may influence the picture considerably.

The 0^{++} channel

Low-lying scalar resonances have been an active topic of research for a while [119, 111, 112, 114, 115, 75, 120, 121, 116]. In the isovector channel, the quenched analysis has been complicated by artifacts of the quenched approximation, so called *ghosts*. (For a discussion see Section 4.2.4.) Most of those results lead to masses for the scalar ground state which were more consistent with the $a_0(1450)$ than with the lowest experimental resonance, the $a_0(980)$. As there are other puzzles surrounding a $\bar{q}q$ interpretation of the $a_0(980)$, some of which we will summarize in Section 4.4, this can be seen as a supporting argument for a tetraquark interpretation of this state. In dynamical calculations ghost states are absent and the inclusion of sea-quark loops may alter the coupling of $\bar{q}q$ interpolators to a resonance with a strong four quark component. At the same time, scattering states, which were not present in the quenched calculations, make the picture more difficult. We now take a look at the results for the isovector scalar channel using our basis of smeared interpolators.

Figure 4.16 shows our results for the ground state in the a_0 channel using just interpolator 8 alone. We are forced to adapt this choice, as most other interpolators (and most matrices of multiple interpolators) lead to very poor plateaus for either run B or run C. To illustrate the quality of the plateaus for interpolator 8, we show effective masses for the two lightest pion masses in Figure 4.17. One possible cause for the very short plateaus in some interpolators may be the presence of scattering states with one particle propagating forward in time while the other propagates backwards in time. Such contributions have been found to play a role in other simulations [122]. In addition, we plot both our best fit and the systematic uncertainty (from fit ranges and choice of in-

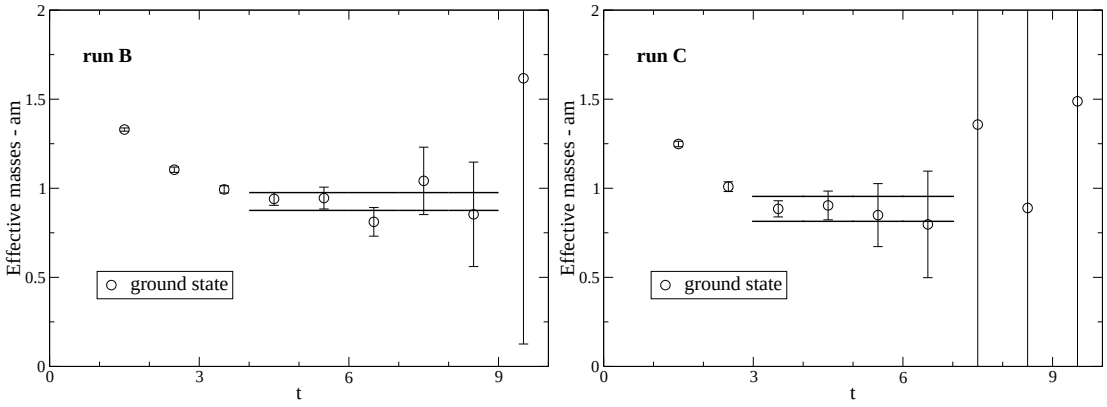

Figure 4.17: Effective masses from interpolator 8 in the 0^{++} channel for run B (left-hand side) and run C (right-hand side). In addition to the effective masses the results of simple uncorrelated two-parameter fits are shown.

terpolators alone) as determined from the quenched data in [3]. While the error bars are large and the linear extrapolation should not be taken too seriously, all of the dynamical data shows a trend towards smaller masses for the ground state of the a_0, making the results more compatible with the $a_0(980)$ than with the $a_0(1450)$. Notice that we refrain from displaying partially quenched results in the a_0 channel as they contain remnants of the quenched ghosts mentioned above. For a description of such partially quenching artifacts, please refer to [115]. In our case, we gained no significant insight from the partially quenched data and we do not discuss it here.

In [120, 117], the authors focus on the mass difference between the lowest state in the 0^{++} and 1^{+-} channels to identify the lightest scalar meson state with an experimental resonance. While the error bars from such an analysis are rather large, the results suggest that the lightest scalar meson may indeed correspond to the experimental $a_0(980)$. We would like to mention that our results from derivative sources qualitatively agree with this assessment and, for the central values, we obtain a mass difference $m_{1^{+-}} - m_{o^{++}}$ ranging from approximately 140 MeV to 220 MeV depending on our choice of interpolators for the b_1.

To understand the role of scattering states better, it would be useful to work with several volumes and to include scattering states in a variational analysis. There are currently several efforts to investigate such multiparticle states using lattice QCD. For an unambiguous determination of the ground state in the a_0 channel, the possibility of the ground state being a scattering state has to be excluded.

4.3.2 Derivative quark sources for higher spin mesons and exotics

So far, we applied derivative quark sources to mesons of spin 0 and 1. Using only one derivative, we can also access the non-exotic spin 2 channels. For a list of interpolators used in this section, please refer to Tables A.3 and A.4 in the appendix. In addition to these channels, we also take a brief look at interpolators with exotic quantum numbers (see Table A.5).

Similar interpolators have been used by Burch et al. for a study on $N_f = 2$ Clover-Wilson lattices [92]. We will compare some of their results with our results in Section 4.3.3.

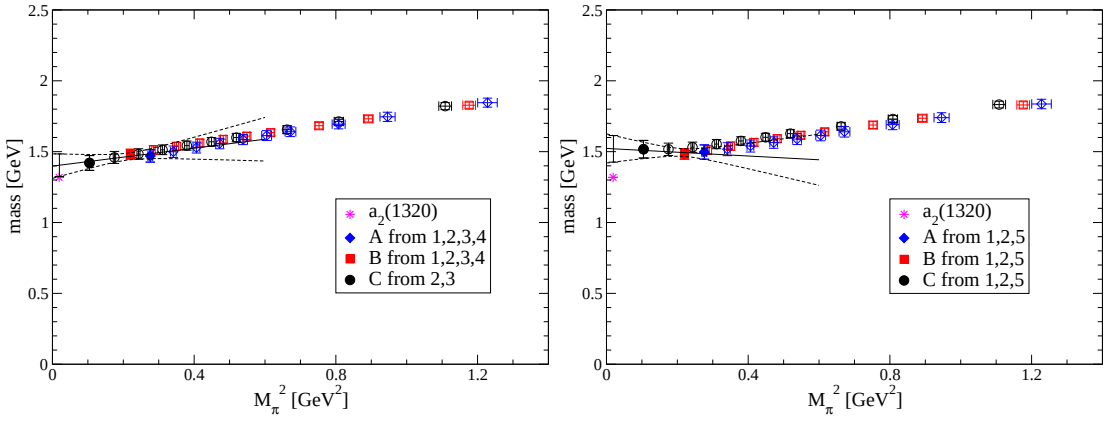

Figure 4.18: Ground state of the a_2 from both the T_2 (left-hand side) and E (right-hand side) irreducible representations. The experimental $a_2(1320)$ is shown for comparison.

The 2^{++} channel

Figure 4.18 shows our results for the 2^{++} channel in both the T_2 (left-hand side) and E (right-hand side) irreducible representations. While the data from the latter extrapolates to slightly larger values, both lead to consistent results which confirms that the ground state in both channels can safely be identified with an a_2 state.

In the E representation, the data from run C turns out rather high which gives a negative slope to our linear fits. We are confident that results from further dynamic ensembles and better statistics would remedy this problem, thereby making the fits from the two different lattice representations more consistent.

The 2^{--} channel

A somewhat weaker signal can also be extracted for the 2^{--} channel, using interpolators in both the E and the T_2 representations. In both cases, the mass plateaus for the fits are very short and a fit has to be performed at rather small Euclidean time separations. The results of such fits can be seen in Figure 4.19. Again, both representations agree and are consistent with an interpretation as the ground state in the respective spin 2 channel, the $\rho_2(1940)$. Notably, there is no sign of a lower-lying spin 3 state (i.e. the $\rho_3(1690)$) which could appear in the T_2 representation as a lattice artifact. As a word of caution, we again stress that the fit ranges for the determination of the mass are very short and that higher statistics would be desirable to make the fits less ambiguous.

The 2^{-+} channel

Finally, Figure 4.20 shows the results for the 2^{-+} channel, where the lowest experimental state is the $\pi_2(1670)$ [15]. Here, the statistical errors are even larger and systematic uncertainties from different interpolators make an extrapolation less reliable. Still, results from both sets of interpolators and for all three ensembles are consistent within two σ. Extrapolations of the lattice data would be consistent with both the $\pi_2(1670)$ and the $\pi_2(1880)$. Similar to the other spin 2 channels, higher statistics would be desirable.

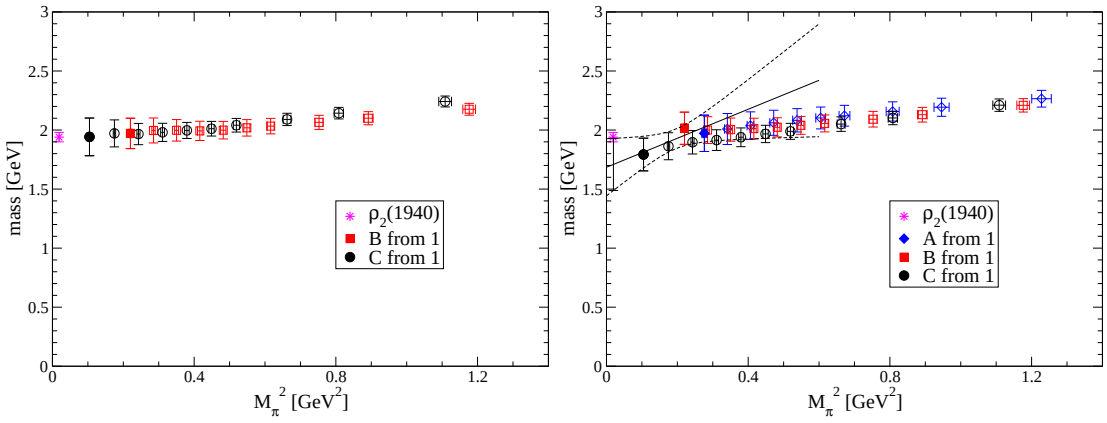

Figure 4.19: Ground state of the ρ_2 from both the T_2 (left-hand side) and E (right-hand side) irreducible representations. The experimental $\rho_2(1940)$ is shown for comparison. In the T_2 representation, more statistics for run A would be needed to obtain an unambiguous fit of the signal. With only two points we therefore refrain from a chiral extrapolation in the T_2 representation.

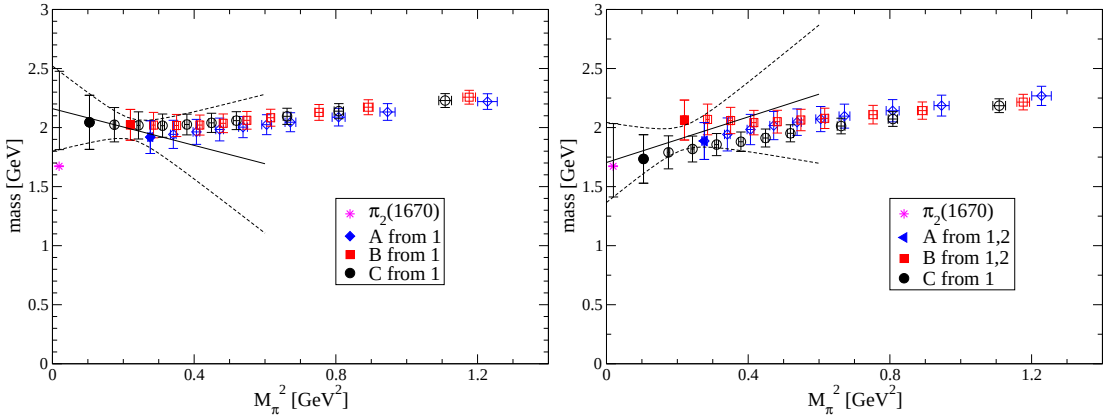

Figure 4.20: Ground state of the π_2 from both the T_2 (left-hand side) and E (right-hand side) irreducible representations. The experimental $\pi_2(1670)$ is shown for comparison. The results of linear extrapolations are also shown.

A look at correlators in exotic channels

In addition to the data described so far, we also took a look at so called *exotic* quantum numbers, for which simple $\bar{q}q$ states do not exist in the naïve quark model. If these states exist, most of them are expected to be rather heavy. Nevertheless, there are two known exotic particles below 2 GeV, the $\pi_1(1400)$ and the $\pi_1(1600)$. They have quantum numbers 1^{-+} which can be constructed using lattice interpolators with derivative quark sources. In addition to this channel, we also calculated correlation matrices in the exotic 0^{--} and 0^{+-} channels. Table A.5 shows the interpolators we used.

Unfortunately all those interpolators lead to very noisy data and we are unable to report any masses for the 1^{-+} channel. To illustrate the typical quality of data we show the lowest two eigenvalues from a matrix analysis of all four interpolators in the π_1 channel in Figure 4.21.

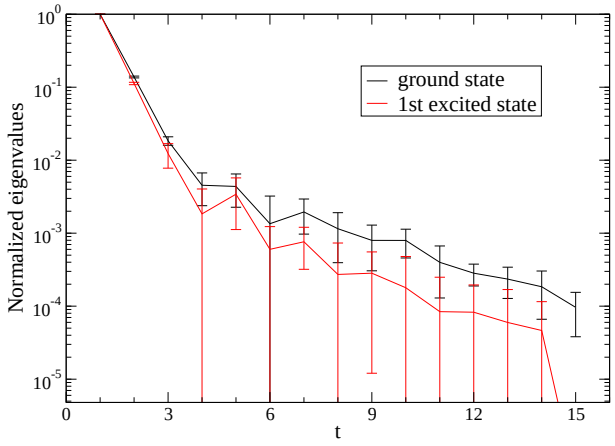

Figure 4.21: The largest two eigenvalues in the exotic 1^{-+} channel. While there is a very weak signal, considerable improvements of our method are needed for a reliable determination of the associated energy levels.

Clearly a much larger number of configurations or better interpolators are needed to obtain a reliable signal. As there is considerable interest in these states, from both theorists and experimentalists, this will be a task for the future.

We would like to point out that results from dynamical lattices for the 1^{-+} channel using different interpolators have been presented in [92]. There are also previous results from quenched QCD [73, 123].

4.3.3 Overview and comparison to previous work

We now want to compare the results of our naïve chiral extrapolations to similar results obtained with quenched CI quarks [84]. In the case of spin 2 mesons, we instead compare to the results from dynamical Clover-Wilson lattices as obtained in [92]. For this purpose, we plot the results of our chiral extrapolations compared to the physical meson excitations. Figure 4.22 shows such a plot. To illustrate nearby experimental states, more experimental states than lattice results are shown. While the errors are rather large, the extrapolated results agree well with the observed spectrum, which is depicted by grey shaded areas or (where the grey areas would only be one line thin) solid black lines. For the pseudovector mesons, results from different interpolators are shown. For an explanation please refer to 4.3.1.

Let us now compare these results with a similar plot from [84]. For light-quark spectroscopy, the results from quenched QCD agree already surprisingly well with experiment in a number of channels. While the errors are too large for strong statements, comparing our results to those of Figure 4.23 indicates that the biggest differences can be seen for the ground state in the 1^{--} channel, the $\rho(770)$, and for the ground state in the a_0 channel.

While the quenched data from a similar volume and lattice spacing leads to a value for the $\rho(770)$ that is about 6% larger than the experimental value, the result obtained from linear extrapolations of our dynamical data is consistent with the experimental value. For the $\rho(770)$ calculations in χPT are available which predict a more complicated fit form [124]. As of now, we lack the number of data points needed to constrain such a fit and therefore only fit to the leading behavior in m_π.

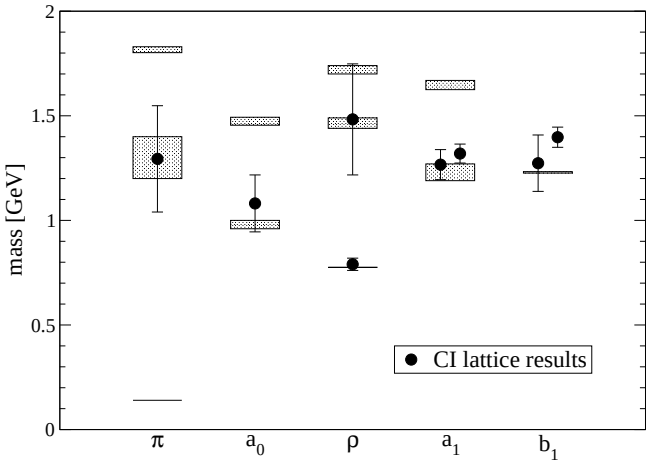

Figure 4.22: Overview of the results from our chiral extrapolations of the dynamical data for spin 0 and spin 1 mesons compared to experimental results from [15]. The experimental results including the errors are depicted as shaded grey areas or solid black lines. The results of our extrapolations are the black circles and the error bars are statistical only. In the pseudovector a_1 and b_1 channels, we display two different results corresponding to Figures 4.14 and 4.15.

For the isovector scalar a_0, the linear fits to our dynamical data from interpolator 8 indicate an extrapolation to masses consistent with the $a_0(980)$. Unfortunately, this interpretation remains somewhat ambiguous as the systematics from the choice of interpolating fields are large and as the data in this channel is very noisy. To settle this issue, high statistics simulations in multiple volumes or a basis which explicitly contains scattering (and possibly also tetraquark states) may be needed. In Section 4.4 we will briefly revisit this channel to present a different point of view.

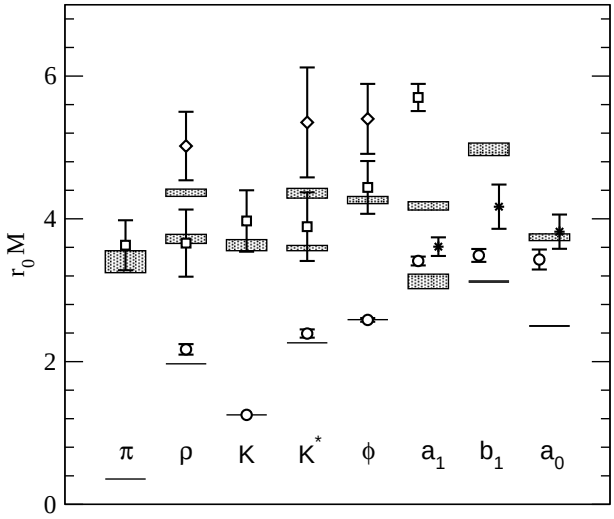

Figure 4.23: Results for the spectrum of light-quark mesons from quenched CI simulations. The shaded areas indicate the experimental data. The plot has been taken from [84].

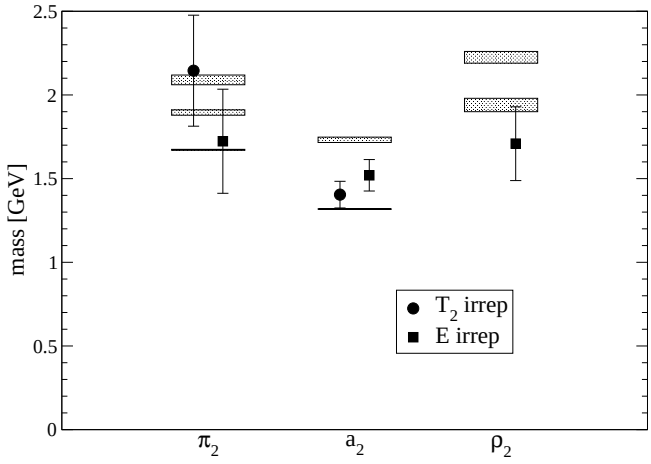

Figure 4.24: Overview of the results from our chiral extrapolations of the dynamical data for spin 2 mesons from both the T_2 and E irreducible representations compared to experimental results from [15]. The experimental results including the errors are depicted as shaded grey areas surrounded by solid black lines. The results of our extrapolations are the black circles and the error bars are statistical only. In the ρ_2 channel a fit was not possible for the T_2 representation. We therefore omit this point.

As a general remark, we would like to point out that the method for setting the lattice scale (see Section 2.8 for a brief discussion) is an overall source of error that will shift the results for the whole spectrum either up or down, depending on the physical value of the Sommer parameter.

Let us now switch to the results we obtained for spin 2 mesons in Section 4.3.2. Here, we have no quenched results from Chirally Improved fermions to compare to. Instead we compare to experiment and to a recent $N_f = 2$ dynamical simulation on Clover-Wilson lattices generated by the CP-PACS collaboration [92]. Figure 4.24 shows our dynamical results compared to experimental results.

As mentioned in Section 4.3.2 all of our results have rather large statistical errors and are obtained from short plateaus at small Euclidean time separations. We first take a look at the channel with the most stable mass plateaus, which is the 2^{++} channel. For the a_2, Burch et al. use interpolators in the T_2 representation, while we use interpolators in both the T_2 and the E representations. The approach in [92] leads to a slightly higher energy of the ground state, but systematic effects can probably account for this small difference. Just like in [92], our results for the a_2 mesons come out slightly higher than the experimental results.

The results in the ρ_2 channel have very large statistical uncertainties and are consistent with experiment. While we use a slightly different basis than [92], there again is a nice agreement between the results obtained from different lattice actions. Notice however that the results from the fine lattice in [92] have considerably smaller errors in this case. For the π_2 channel on the other hand, we use interpolators with a different structure and obtain somewhat smaller errors. To constrain the linear extrapolations better, more data points and increased statistics will be useful. As we are working on rather coarse lattices, cutoff effects may be important for states in this mass region. This will have to be investigated in the future.

4.4 Light scalar mesons from tetraquark interpolators

It has been conjectured [125, 126] that scalar mesons below 1 GeV may be tetraquark states rather than conventional $\bar{q}q$ states. In [9] we provided some of the empirical arguments for such an interpretation and studied light scalar mesons on the lattice using a variational basis of tetraquark interpolators. In this section, we briefly summarize the main arguments for a tetraquark interpretation of light scalar mesons, introduce our interpolating fields and present the most important results. For more details, the reader is referred to [9]. Similar studies restricted to the isospin 0 and 2 cases have been performed by other authors [127, 75, 72, 128]. Our findings are in general agreement with these results.

4.4.1 Arguments for a tetraquark interpretation of light scalar mesons

There are several arguments from phenomenology suggesting that light scalar mesons are given by tetraquark states rather than conventional $\bar{q}q$ states:

- The pattern of observed states below 1 GeV resembles the pattern expected from a tetraquark nonet, rather than the pattern expected from $\bar{q}q$ states.
- The observed $K_0^\star$ or κ resonance, which would be identified with a $\bar{u}s$ state or a $[ud]\left[\bar{d}\bar{s}\right]$ tetraquark respectively, is observed at a mass much lower than the $a_0(980)$, which should either be a $\bar{u}d$ state or a $[us]\left[\bar{d}\bar{s}\right]$ tetraquark. This would be natural in the tetraquark picture, while it cannot be reconciled with a naïve $\bar{q}q$ picture.
- Quark model calculations lead to masses well above 1GeV for the isovector scalar a_0, while correctly describing the levels of the a_1 and b_1 pseudovector mesons.
- The fact that the $a_0(980)$ couples strongly with $K\bar{K}$ also suggests a tetraquark nature of this state [129].

4.4.2 Tetraquark interpolators

For our variational analysis we use diquark-antidiquark interpolators composed of a scalar diquark

$$[qQ]_a \equiv \epsilon_{abc}[q_b^T C\gamma_5 Q_c - Q_b^T C\gamma_5 q_c] \ ,$$

in the color anti-triplet, and a scalar-antidiquark in the color-triplet

$$[\bar{q}\bar{Q}]_a \equiv \epsilon_{abc}[\bar{q}_b C\gamma_5 \bar{Q}_c^T - \bar{Q}_b C\gamma_5 \bar{q}_c^T] \ .$$

We then simulate the following combinations

$$\begin{aligned} \mathcal{O}^{I=0} &= [ud][\bar{u}\bar{d}] \ , \\ \mathcal{O}^{I=1/2} &= [ud][\bar{d}\bar{s}] \ , \\ \mathcal{O}^{I=1} &= [us][\bar{d}\bar{s}] \ , \end{aligned}$$

where all quarks are Gaussian smeared quarks with the smearing parameters of [84] as described in Section 3.6.2. When calculating the Wick-contractions contributing to correlation functions, we neglect single and double annihilation diagrams.

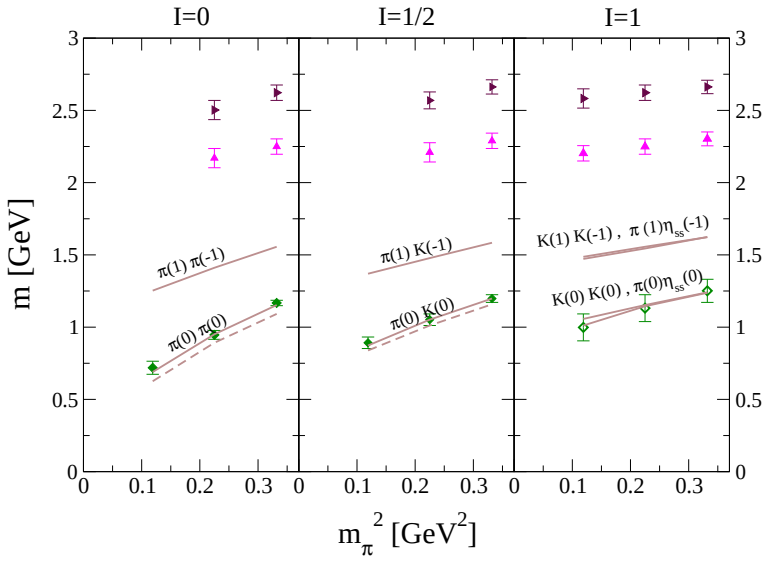

Figure 4.25: Energies from tetraquark correlators in the isospin 0, $\frac{1}{2}$ and 1 channels as presented in [9]. The symbols show the lattice data, while the lines represent analytic energy levels for scattering states: solid lines display the non-interacting energies, while the dashed lines include tree-level energy shifts. For an explanation why the scattering state with relative momentum is missing please refer to [9].

4.4.3 Results and discussion

For the simulations in [9], lattices of size $12^3 \times 24$ and $16^3 \times 32$ have been used. For both lattices, the lattice spacing $a = 0.148\,\text{fm}$ has been determined from the Sommer parameter in [110]. The pion masses used for the analysis range from 344 MeV to 576 MeV.

For scattering states, contributions from states wrapping around the temporal extent of the lattice play an important role. Specifically, these are contributions where one of the particles propagates forward in time, while the other particle propagates backward in time (and vice-versa) [118]. For the eigenvalues corresponding to the ground states we obtain

$$\lambda^{P_1(0)P_2(0)} = C\left(\mathrm{e}^{-E_0 t} + \mathrm{e}^{-E_0(T-t)}\right) + A\left(\mathrm{e}^{-m_1 t}\mathrm{e}^{-m_2(T-t)} + \mathrm{e}^{-m_1(T-t)}\mathrm{e}^{-m_2 t}\right) \quad , \tag{4.4}$$

where $P_1(0)P_2(0)$ stands for the scattering state involving particles P_1 and P_2 with masses m_1 and m_2 and vanishing momentum $p = 0$. Using the single hadron masses obtained from regular meson correlators, we can perform a three parameter fit to this form. In the case of particles with equal mass, the second term on the right-hand side of Equation 4.4 reduces to a constant.

Figure 4.25 shows the results in the larger volume for all three isospin channels. In each case the observed ground states are compatible with the energy levels for the respective scattering states. In addition to the expected scattering states, no other low-lying states are observed[5]. While we refrain from an interpretation of the higher-lying observed states, we want to stress that with the basis we used, we did not see any evidence of tetraquark states below 1 GeV in our range of pion masses. We also want

[5]For an explanation why the scattering states with momenta are not seen please refer to [9].

to emphasize that this is not in contradiction with the results in [75], where evidence for a tetraquark assignment of the σ-meson has been found. More recently, Prelovsek et al. used a larger basis of tetraquark interpolators on dynamical CI configurations. Preliminary results have been reported in [130].

Chapter 5

Excited charmonium on the lattice

The methods introduced in Chapter 3 to deal with excited states on the lattice can also be applied to systems involving heavy quarks. In this chapter, we will present preliminary results of an exploratory study of the charmonium spectrum. For this purpose, we use gauge field configurations created by the MILC-collaboration (for a description of the ensembles see [131, 69, 132]) using 2+1 flavors of Asqtad staggered quarks. For the heavy valence quarks, we use Clover-Wilson type quarks and employ the *Fermilab Method* [133]. Previous results from this approach by the Fermilab-MILC collaboration have been presented in [134, 135, 136], where the main focus has been on ground states. In addition, the effects of disconnected diagrams on the hyperfine splittings in charmonium have been investigated in [137, 138]. For an overview of general results from 2+1 flavors of Asqtad staggered quarks including previous results for charmonium, we refer the reader to [132].

Here our approach will be different. After briefly discussing the physics of interest in 5.1, we will present our basis of interpolators for the spectroscopy of excited charmonium in Section 5.2. We will proceed by presenting preliminary results from a single dynamical ensemble. We compare these results to the previous literature in 5.3.4 and conclude with a short outlook.

5.1 Physics of interest

Charmonium physics is both a challenging and promising topic for lattice QCD simulations. On the one hand, there are very accurate experimental results that can serve as a precision test for lattice calculations, provided all systematic errors are under control. On the other hand, there is quite a vivid dispute about the nature of some excitations observed by experiments. In particular, there is renewed interest in *exotics* (states with quantum numbers that do not exist in a simple quark model) and in *hybrid mesons* (states with some sort of gluonic excitation). Notice that we will refer to all of those as charmonium, even though there is a possibility that some observed states may be tetraquark states. We will now take a brief look at possible states of interest.

More specifically, we will focus on channels which should be accessible with our basis of both conventional and hybrid charmonium interpolators. We now discuss some states where our approach might be promising. For a more comprehensive overview of the experimental situation we refer to [139, 140].

- **Exotics:** With our interpolators constructed from derivative sources, we can access the 0^{--}, 0^{+-} ,1^{-+} and 2^{+-} exotic channels. For all of these quantum numbers, already the ground state is of interest.

- **X(3872):** The X(3872) most likely has quantum numbers 1^{++}. If this is the case, it will be the first excitation in this channel. Based on either phenomenological arguments or lattice calculations, there are speculations about the nature of this state. On the lattice there have been two studies, one of them concluding that the state is probably the first radial excitation of the χ_{c1} [141], while the other finds indications for a tetraquark nature of the state [142]. For the arguments from phenomenology we refer the reader to [139, 140].

- **Z(3920):** The Z(3920) is now commonly viewed as the χ'_{c2}, the first radial excitation in the 2^{++} channel. If this is the case, this state should be accessible with our method.

- **X(3940):** There is evidence that this state is either a scalar or, more likely, a pseudoscalar meson state [140]. This would suggest an interpretation of this state as the η''_c. If this is the case, a reliable extraction of this state on the lattice could be feasible.

- **Y(4260):** The Y(4260) with quantum numbers 1^{--} is of special interest as there are many states in this channel which are well known. While most interpretations agree that this state is not a radial charmonium excitation, there are arguments for both an interpretation as a hybrid meson as well as an interpretation as a tetraquark or molecular state. On the lattice, the authors of [143] calculate both molecular as well as diquark-antidiquark states and come to the conclusion that the Y(4260) might be a tetraquark state. The authors of [144] take a look at hybrid interpolators and find masses in the vicinity of the Y(4260). At the same time, their ground states in the 1^{--} channel show a significant deviation from the J/Ψ when compared to traditional charmonium interpolators. To extract the $Y(4260)$ unambiguously, one should work with a combined basis of regular and hybrid interpolators (or tetraquark states) and try to extract both the $Y(4260)$ as well as all lower excitations. Currently, extracting this state will probably be too difficult of a task as many lower excitations will have to be identified without ambiguities as well.

In addition to those states, there are many well established charmonium states which can serve as a benchmark for our calculation. Apart from the ground states, these include the η'_c and the Ψ' excitations, which should both lie below the respective two particle thresholds. For higher excitations, the situation might be complicated by scattering states. In [145], an analysis with a basis including multi-particle states has been performed to identify possible mixing with those states.

5.2 A variational basis for our goals

To reach our objective, we will need a diverse basis which covers all quantum numbers and all irreducible representations. We opt for a basis built from interpolators with derivatives and use interpolating operators similar to those suggested by Liao and Manke [102], which have also been used by Dudek *et al.* [86]. Like in [86], we use a large set of interpolating operators and apply the variational method as detailed in Section 3.3.

In addition to point sources S_0 we use Gaussian-smeared sources, which are implemented by acting with a smearing operator M on point sources S_0 to obtain Gaussian sources

$$G = MS_0 = A\,(1+\kappa H)^N\,S_0\ , \tag{5.1}$$
$$H(\vec{x},\vec{y}) = \sum_{i=1}^{3}\Big(U_i(\vec{x},0)\delta(\vec{x}+\hat{i},\vec{y}\,) + U_i(\vec{x}-\hat{i},0)^\dagger\delta(\vec{x}-\hat{i}\ ,\vec{y}\,)\Big)\ ,$$

where A is just a normalization and κ and N have been chosen such that this approximates a Gaussian (in coordinate space) with standard deviation σ. This is the case for

$$\kappa = \frac{\frac{\sigma^2}{4N}}{A}\ ,$$

and by $\exp(a) \approx (1+\frac{a}{N})^N$ we obtain for $N\to\infty$

$$\lim_{N\to\infty} S_G = \mathrm{e}^{\sigma^2\nabla^2/4}\ .$$

Notice that this definition differs slightly from Equation 3.13 and was already mentioned in Equation 3.17. We want to stress that H is hermitian and we have $M^\dagger = M$.

Let us now discuss some technical aspects of our construction which are particular to the lattice implementation of interpolators containing derivatives. For interpolators with a single derivative P_i as presented in 3.6.2 (for a similar construction see also [86]) an anti-symmetrization is needed to ensure the correct behavior under charge conjugation at finite spatial momenta. The same symmetrization is also needed with the particular construction presented in Chapter 3. Implementing this as presented in Chapter 4, one needs n^2 source-sink combinations where n is the number of different source smearings. As we are planning to include an even larger number of source smearings, calculating all these combinations would be prohibitively expensive, regarding both CPU time and memory requirements. To understand how we can construct similar sources with less effort, let us take a look at Equation 4.2 again. For the connected part of unsmeared charmonium correlators we have

$$\big\langle O(n)\bar{O}(m)\big\rangle_F = -\mathrm{tr}\left[\Gamma_2 D_c^{-1}(m|n)\Gamma_1 D_c^{-1}(n|m)\right]\ .$$

Let us now discuss two versions of smeared quark sources:

A Smeared quark sources created by first constructing a Gaussian source and subsequently applying a covariant derivative. This is the technique used in Chapter 4. For a derivative source constructed in this way we write

$$\nabla_i^{(A)} = P_i M S_0\ .$$

B Smeared sources created by first point splitting the source with a derivative and subsequently smearing the results. Here we have

$$\nabla_i^{(B)} = M P_i S_0\ .$$

In the following, we will denote quark propagators from such sources at point m to a sink at point $n=(x,t)$ by $P_{\nabla,A}(n,m)$ and $P_{\nabla,B}(n,m)$ for derivative sources and $P_G(n,m)$

for Gaussian sources. We now take a look at different possibilities. Let us denote by $C_{BA;DC}$ a correlator with smearing A and B for the antiquark at the source and the sink and smearings C and D for the quark at source and sink. Let A-D either be Gaussian (G) or derivative type (∇) of smearings.

Let us now discuss variant **A** from above. For derivatives that always act on the antiquark we obtain (all color and Dirac indices are suppressed for clarity)

$$C_{\nabla\nabla;GG}(t,0) = \sum_x \mathrm{tr}\left[P_{\nabla,A}(m,n')\Gamma_1(\overleftarrow{P_i}\overleftarrow{M})(n',x)\overrightarrow{M}(x,n'')P_G(n'',m)\Gamma_2\right] , \qquad (5.2)$$

where we use a symbolic notation with the intermediate indices n' and n'' summed over and the final smeared propagators transport the particles from a source at m in timeslice 0 to a sink at $n = (x,t)$, where a momentum projection is performed. Γ_1 and Γ_2 are in general different for off-diagonal elements and, in our symbolic notation, the arrows indicates the direction in which the smearing is applied. Notice that we have $P_i = -P_i^\dagger$. Let us now take a look at a second term arising out of 5.2 by acting with the derivative on the quark instead of acting on the antiquark at the sink. We obtain

$$C_{G\nabla;\nabla G}(t,0) = -\sum_x \mathrm{tr}\left[P_{\nabla,A}(m,n')\Gamma_1\overleftarrow{M}(n',x)(\overrightarrow{M}\overrightarrow{P_i})(x,n'')P_G(n'',m)\Gamma_2\right] . \qquad (5.3)$$

Notice that this term arrises in addition to the first term when the operator at the sink is symmetrized. For smeared quarks these two terms are in general not the same, as P_i and M do not commute. In an anti-symmetrized operator, the part arising from the commutator gets killed while it is isolated in the symmetrized operator. This leads to an admixture of the wrong charge conjugation in naïve, unsymmetrized operators, which we verified numerically for interpolators in exotic channels. As an example one will measure an η_c in interpolators with exotic quantum numbers 0^{--}. Using the same notation we obtain for the remaining terms

$$C_{GG;\nabla\nabla}(t,0) = -\sum_x \mathrm{tr}\left[P_G(m,n')\Gamma_1\overleftarrow{M}(n',x)(\overrightarrow{M}\overrightarrow{P_i})(x,n'')P_{\nabla,A}(n'',m)\Gamma_2\right] .$$

$$C_{\nabla G;G\nabla}(t,0) = \sum_x \mathrm{tr}\left[P_G(m,n')\Gamma_1(\overleftarrow{P_i}\overleftarrow{M})(n',x)\overrightarrow{M}(x,n'')P_{\nabla,A}(n'',m)\Gamma_2\right] .$$

Let us now take a look at variant **B**, where the Gaussian-smearing and the derivative are exchanged. In this case we obtain for the terms of Equations 5.2 and 5.3:

$$C_{\nabla\nabla;GG}(t,0) = \sum_x \mathrm{tr}\left[P_{\nabla,A}(m,n')\Gamma_1(\overleftarrow{M}\overleftarrow{P_i})(n',x)\overrightarrow{M}(x,n'')P_G(n'',m)\Gamma_2\right] .$$

$$C_{G\nabla;\nabla G}(t,0) = -\sum_x \mathrm{tr}\left[P_{\nabla,A}(m,n')\Gamma_1\overleftarrow{M}(n',x)(\overrightarrow{P_i}\overrightarrow{M})(x,n'')P_G(n'',m)\Gamma_2\right] .$$

In this case there is no need for an anti-symmetrization and we can restrict ourself to one of the terms. We choose the variant where the derivative always acts on the antiquark at the source and on the quark at the sink. This choice reduces the number of propagators we need to calculate, as the antiquark propagator will be expressed as a quark propagator by making use of the γ_5-hermiticity of the Dirac operator, as mentioned in Chapter 4. Therefore, quark sources correspond to antiquark sinks.

Having discussed these issues, we can finally list the different quark smearings. In analogy to [86], we use

$$\begin{aligned} \nabla_i &= M\overrightarrow{P}_i S_0 \ , \\ \mathbb{B}_i &= \varepsilon_{ijk} M\overrightarrow{P}_j \overrightarrow{P}_k S_0 \ , \\ \mathbb{D}_i &= |\varepsilon_{ijk}| M\overrightarrow{P}_j \overrightarrow{P}_k S_0 \ . \end{aligned} \tag{5.4}$$

Notice that the continuum version of operator $\mathbb{B}_i$ has a relation to the chromomagnetic parts of the field strength tensor

$$\mathbb{B}_i^{(cont.)} = -\frac{\imath}{2}\varepsilon_{ijk}F^{jk} \ .$$

To obtain interpolators with a smearing in the A_2 irreducible representation we could use

$$\mathbb{A} = |\varepsilon_{ijk}| M\overrightarrow{P}_i \overrightarrow{P}_j \overrightarrow{P}_k S_0$$

in addition. In Appendix B we present tables of interpolators for each lattice irreducible representation along with information on some of the details of their evaluation. We also experimented with the type of derivative and the width of the smearing for the Gaussian sources. We therefore also provide information on our final parameters in the same appendix.

5.3 Preliminary results

We now want to present some preliminary results from one medium coarse ensemble on a $16^3 \times 48$ lattice with a lattice spacing of 0.15 fm. The light quark masses correspond to a pion mass of approximately 322 MeV and the strange quark mass is approximately the physical strange quark mass. The charm quark masses have been determined within the Fermilab-MILC collaboration by tuning the heavy quark hopping parameter κ to obtain the correct kinetic mass for the D_s meson. This tuning is done for a light sea quark mass and subsequently adopted for all ensembles with the same lattice spacing. For a discussion of discretization effects arising within the Fermilab interpretation of heavy quarks we refer the reader to [133]. We use 600 configurations with four time slices per configuration. For the analysis we first average the resulting four matrices and subsequently perform a single-elimination jackknife to determine the statistical errors.

5.3.1 A first look at the data

Figure 5.1 shows results for effective masses from single diagonal correlators in the η_c channel. At large Euclidean times all correlators receive a good signal from the ground state. At small times only the Gaussian smeared interpolators 1 and 3 start out almost flat, all other correlators show signs of significant contributions from excited states. While the interpolators containing the $\mathbb{B}$ operator are the noisiest ones, they also contain the strongest contributions from excited states at small Euclidean times.

Figure 5.2 shows a similar plot for the J/Ψ channel. Here the situation is more interesting as some of the interpolators from Table B seem to couple only very weakly to the ground state. At the same time the behavior of cross correlators and at large Euclidean times verifies that these interpolators also couple to the J/Ψ.

To illustrate the quality of single correlators in one of the more typical channels we also present a similar figure from the T_2^{++} channel. Here we have only 4 correlators and one of them is very noisy. We will see how this affects the number of states that can be fit in the next section.

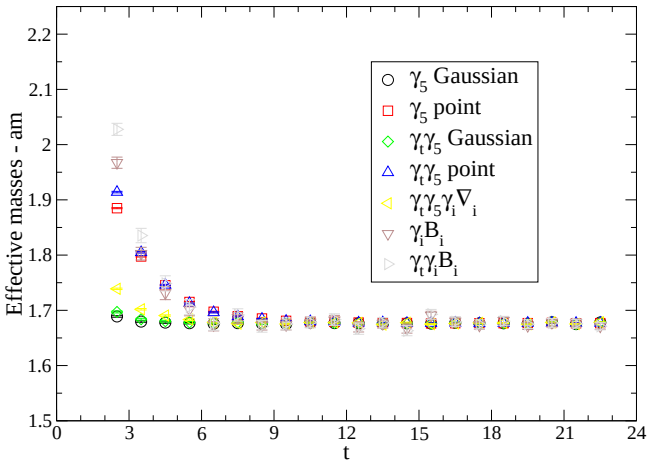

Figure 5.1: Effective masses from single diagonal correlators in the A_1^{--} channel. The ground state in this channel corresponds to the η_c. The interpolators are labeled like in the appendix.

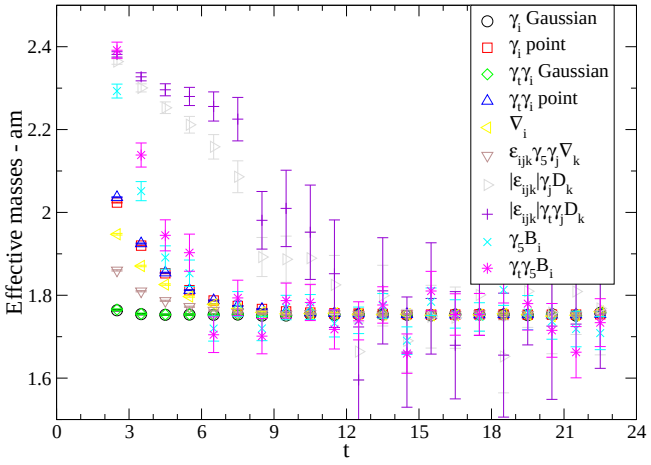

Figure 5.2: Effective masses from single diagonal correlators in the T_1^{--} channel. The ground state in this channel corresponds to the J/Ψ. The interpolators are labeled like in the appendix.

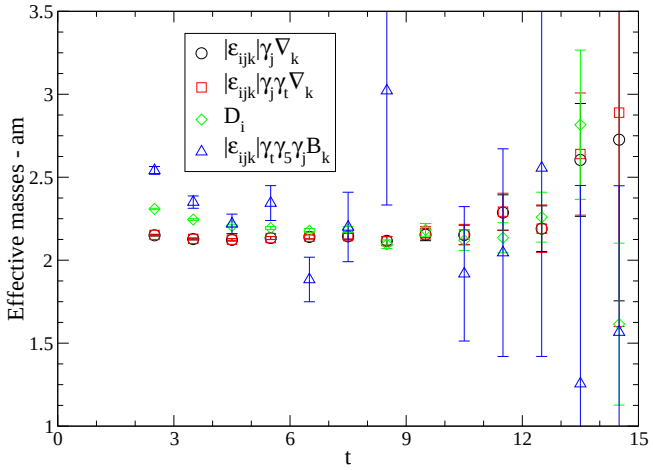

Figure 5.3: Effective masses from single diagonal correlators in the T_2^{++} channel. The ground state in this channel corresponds to the χ_{c1}. The interpolators are labeled like in the appendix.

5.3.2 Effective masses

The main goal of this exploratory study is to get an idea what kind of results we can reasonably obtain from this method. In this section, we therefore focus on the physics objectives formulated in 5.1. We also make some comments on necessary interpolator pruning and present effective mass plots for the respective ground states and lowest charmonium excitations. We compare these results with existing literature in 5.3.4. For the eigenvalue fits we use correlated fits as described in Section 3.4.

Let us start our discussion with the J/Ψ channel. In this channel, the signal is the best, our basis is the largest and there are the most experimentally known excitations. While we can use our full basis of interpolators for this channel, we obtain the best results for the combination displayed in Figure 5.4. With a basis of six interpolators we

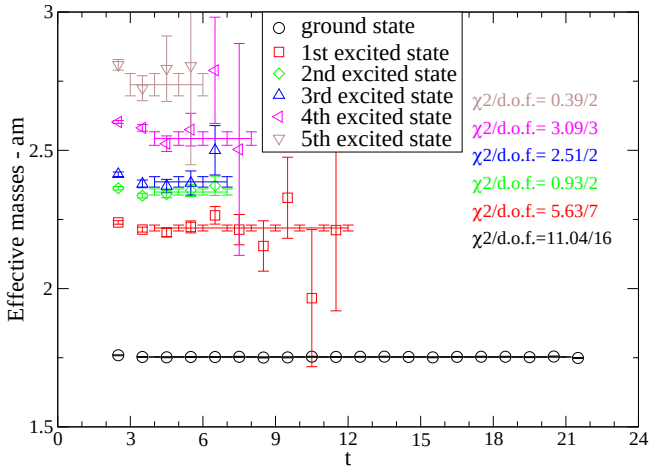

Figure 5.4: Effective masses from a correlation matrix analysis in the T_1^{--} channel. The ground state corresponds to the J/ψ. The first excited state is the $\psi(2S)$. To identify the other states we would need more data.

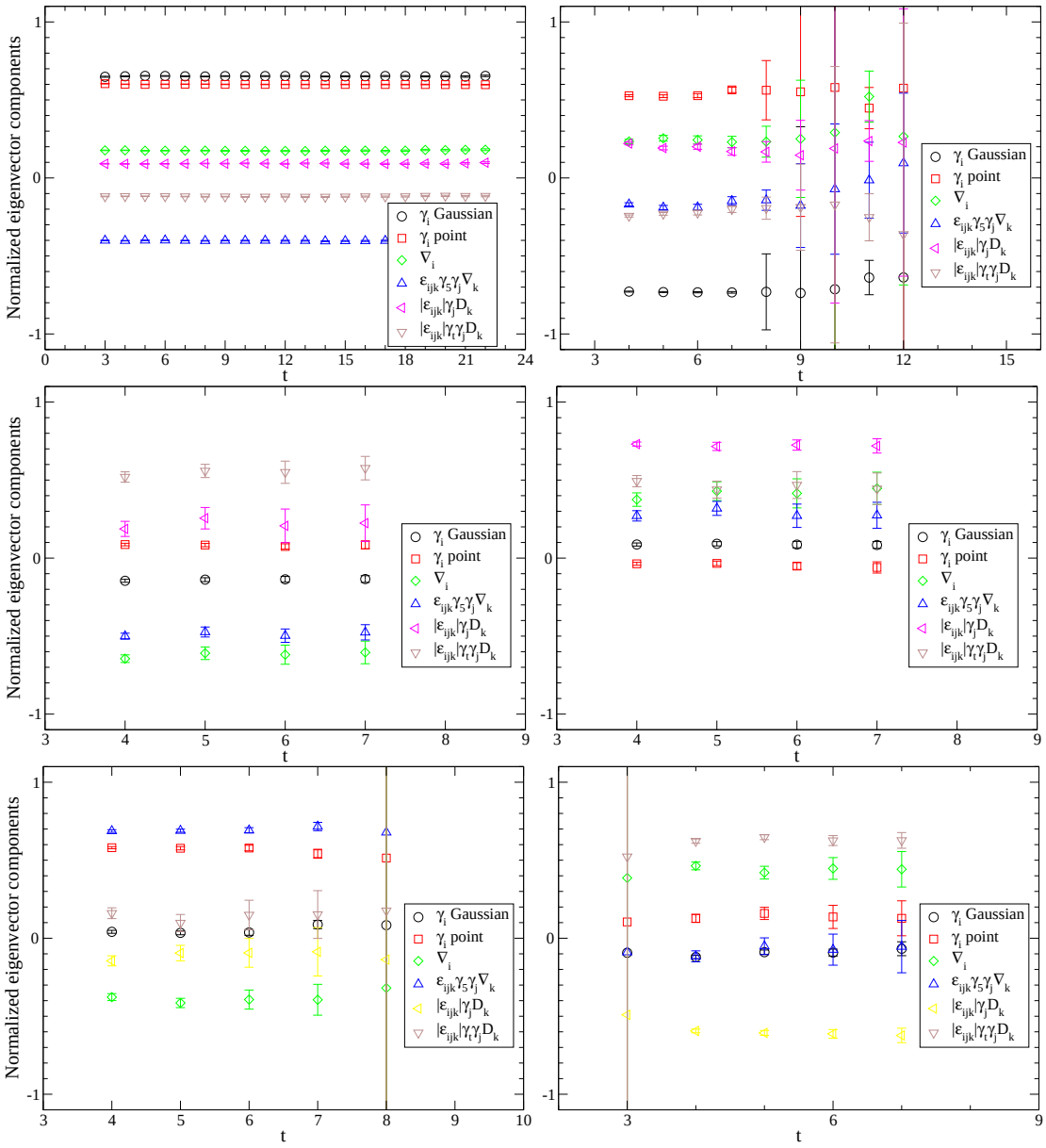

Figure 5.5: Eigenvectors corresponding to the six lowest energy levels in the T_1^{--} channel. All plateaus are stable (within error bars) in the range the masses have been fit. The states are displayed from left to right and from top to bottom, starting with the ground state on the left-hand side of the top row.

can fit six states, although the highest one may not be reliable. To obtain the fit ranges displayed in Figure 5.4, we took a look at the components of the eigenvectors for all six states displayed. The result of this can be seen in Figure 5.5. For our fit ranges we observe stable plateaus in all eigenvector components. While a larger submatrix would be desirable, some of our interpolators just contribute more noise and not more signal. Notice that the $Y(4260)$ mentioned in 5.1 is in this channel. As at least one of the energy levels we see here is likely a state with spin 3 (or maybe even a scattering state), a substantial increase in quality of the data on the finer lattices would be needed to identify this state.

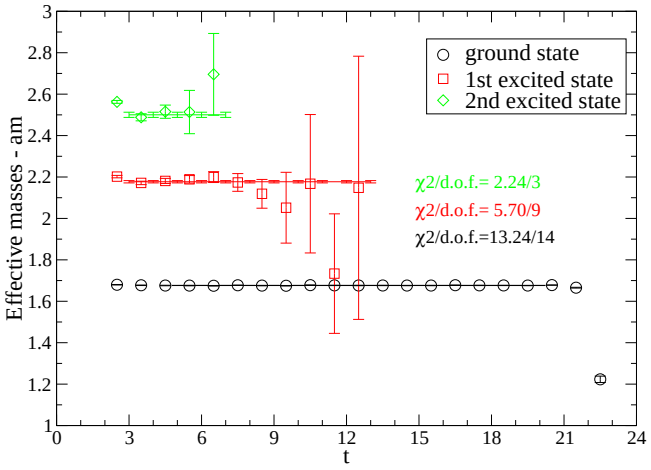

Figure 5.6: Effective mass plot for the lowest three states in the A_1^{-+} channel. The ground state in this channel can readily be identified with the η_c and the first excited state corresponds to the $\eta_c(2S)$.

Next, let us turn our attention to the η_c channel. Figure 5.6 shows fits for the three lowest states in this channel. On finer lattices even more energy levels may be obtainable but as the quality of the fourth mass plateau is very bad we restrict the fits to the three lowest energies. As mentioned, the ground state in this channel corresponds to the η_c and the first excited state is readily identified as the $\eta_c(2S)$. The third state may or may not correspond to the $X(3940)$. We will present a rough comparison of energy levels with the pattern of experimental states in the next section.

Another experimental state of interest is the $X(3872)$, which most likely has quantum numbers 1^{++}. Figure 5.7 shows an effective mass plot for this channel. The ground state can be identified as the χ_{c1} and if the $X(3872)$ is a regular quarkonium state it should correspond to the first excited state. Currently the systematic uncertainty for a fit of the second excitation is rather large and we obtain the best signal from a correlation matrix with just three interpolators.

The $Z(3920)$ is now commonly viewed as the first radial excitation in the χ_{c2} channel. There are two lattice irreducible representations (see Table 3.1 in Chapter 3) which both contain the continuum spin 2 states. While the next lowest spin in the E representation is spin 4, the T_2 representation may also couple to spin 3 states. Unfortunately, the results from our current data are less than conclusive as there is still an error in the data from the E representation and we therefore had to prune the correlation matrix in this channel to just two interpolators. Doing the same in the T_2 channel leads to unrealistically high values for the first excited state, while adding more interpolators brings down the energy level corresponding to the first excited state. We will show both values in our overview plot in Section 5.3.3, but we want to remind the reader about the preliminary nature of these results. Figure 5.8 shows a comparison of the effective masses obtained for the J^{++} channel from both representations.

For the exotic channels, the signals are usually very weak. In the A_1^{+-}, the T^{-+} and the E^{+-} channels indications for exotic excitations can be seen but, as the plateaus are very short, we will only show some of the diagonal correlators to illustrate the quality of the data. On finer lattices, fits to these states should become much more reliable. Figure 5.9 shows diagonal correlators for the T_1^{-+} and A_1^{+-} channels. In both of those

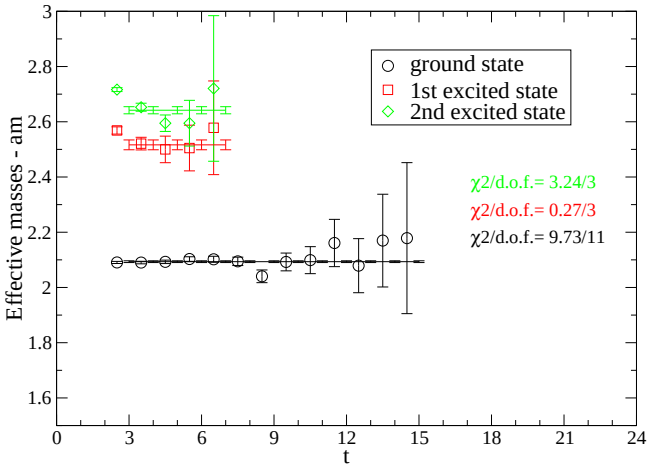

Figure 5.7: Effective masses for the three lowest energy levels in the T_1^{++} channel. The ground state in this channel corresponds to the η_c while the first excitation may correspond to the $X(3872)$.

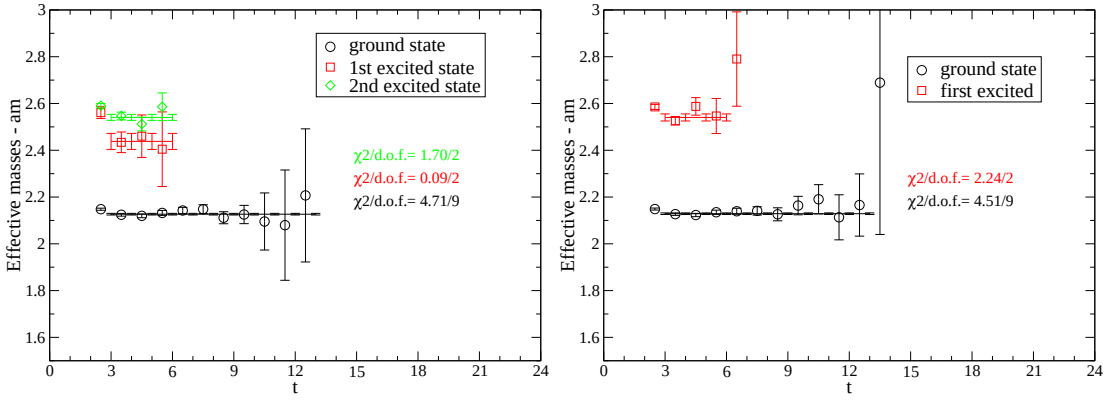

Figure 5.8: Effective masses for the T_2^{++} and the E^{++} representations. For a description of the data please refer to the text.

channels a signal can most likely be identified with an exotic, as the lowest-spin non-exotic contamination due to breaking of continuum rotational invariance would have quantum numbers 4^{-+} and contribute to the T_1 representation. Such an admixture of a non-exotic spin 4 state can however not be fully excluded at this stage. While there is only one correlator with a good signal in the A_1^{+-} channel, there are multiple good correlators in the T_1^{-+} channel.

In addition to the results discussed so far, we can extract various non-exotic spin 2 and spin 3 ground states as well as a couple of higher energy levels whose interpretation is not clear. We will present some data in the next section and postpone a more comprehensive analysis.

5.3.3 Mass splittings

Before we present an overview of our results compared to the physical charmonium excitations, we want to remind the reader that there are a number of steps missing for

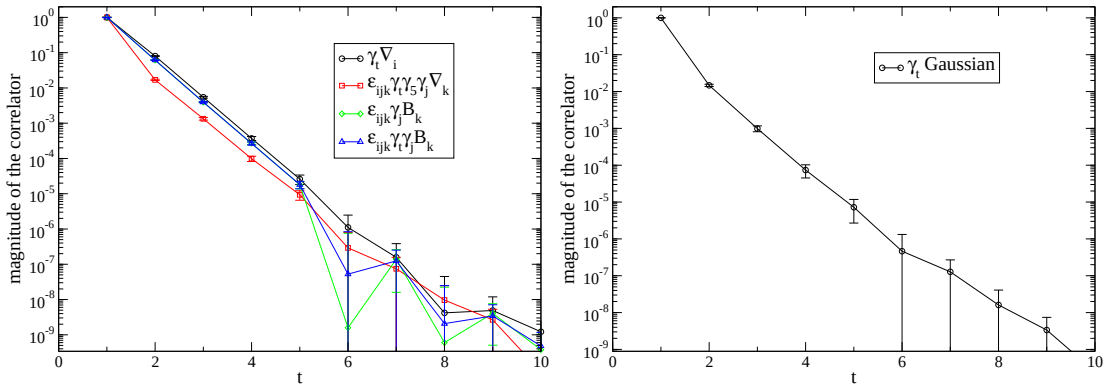

Figure 5.9: Diagonal correlators for two of the exotic channels. On the left-hand side four different correlators in the T_1^{-+} channel are shown while we display a single diagonal correlator for the A_1^{+-} channel on the right-hand side.

a thorough investigation. We will discuss those in 5.4.

While discretization effects for the meson rest masses (sometimes also referred to as the *pole masses*) are large, some of these effects drop out when considering energy differences between rest masses [146]. In a similar spirit to [134, 135, 136], we therefore plot energy differences to the spin averaged $1S$ mass $\left(3M_{j/\Psi} + M_{\eta_C}\right)/4$. Figure 5.10 shows a plot of the energy levels in the non-exotic channels discussed in the previous section. In addition, the T_1^{+-} channel containing the h_c is also included. The experimental states including their errors are denoted by black boxes. In most cases, the errors from the experimental determination are smaller than the box. Comparing the ground states to the results from [136] shows a nice agreement. The small differences probably stem from the lack of a chiral extrapolation in our preliminary data. This fact may also lead to artificially small error bars, as the data usually gets noisier towards the chiral limit.

In addition to the ground states we plot all other energy levels in the respective channel. Apart from regular excitations, these may also include states of higher continuum spin and scattering states. As a general trend, the excited states turn out to be too high. This is especially visible with states above the $D\bar{D}$ threshold, where we expect a stronger effect of a chiral extrapolation. Some of the energy levels most likely correspond to states of a higher continuum spin. To investigate this further, we plot the ground states in the non-exotic A_2 channels in Figure 5.11. A naïve comparison of energies suggests possible spin 3 states in the J/Ψ, h_c and in the χ_{c2} channels, which we will have to investigate more thoroughly in the future. As far as our physics objectives described in Section 5.1 are concerned, there is a good chance to determine properties of the states in question. One exception is the $Y(4260)$ in the 1^{--} channel. Even assuming that this state is either a regular charmonium or a hybrid state, we already noticed that at least one spin 3 state can be found in this channel. This shows that an unambiguous identification of this state will be very complicated.

5.3.4 Comparing our results to the literature

In addition to the studies from the Fermilab-MILC collaboration, the ground states in various channels have also been determined by the HPQCD collaboration using HISQ fermions on MILC lattices [147]. Also the χQCD collaboration studied the charmonium spectrum in quenched QCD using overlap quarks [148].

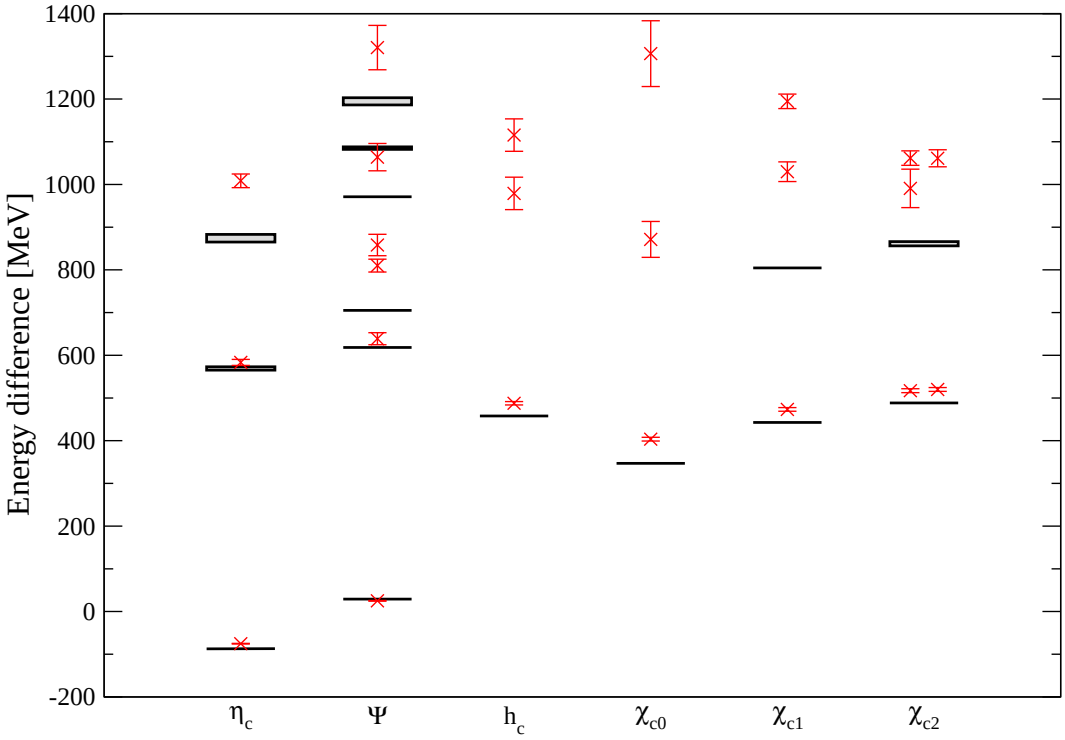

Figure 5.10: Energy levels obtained from our lattice simulation compared to experimental states (black boxes). Most experimental errors are smaller than the box. Note that no definite spin assignment of lattice data has been made. It is likely that some of the excitations displayed are either spin 3 or spin 4 ground states. The two different data sets for the χ_{c2} are from the T_2 (left) and the E representation (right). For a discussion please refer to the text.

As previously mentioned, Dudek *et al.* [86] studied the spectrum of excited charmonium on a single quenched ensemble. In general our results are of a similar quality for most of the channels of interest. In addition to smeared derivative sources, the authors of [86] also use local derivative sources without any Gaussian smearing in the construction. This makes their basis larger for some of the higher spin channels. At the same time, our construction without an explicit symmetrization is computationally less expensive. Having established that our method works, we can extend our approach in the future. We will outline a possible program in the next section.

Calculations of excited charmonium on dynamical lattices have also been presented by Ehmann and Bali [149, 145]. In [149] they obtain first excited states in various channels and observe a pattern similar to the results presented in the previous section, with excitations in general coming out too high.

5.4 Outlook

So far, we calculated a large set of regular and hybrid charmonium interpolators on a single ensemble of gauge configurations. For a comprehensive study, the program outlined in Section 2.7 remains to be done. We will need to repeat our calculations for multiple sea quark masses to perform an extrapolation in the light quark mass. The authors of [135, 136] find that the dependence of the ground states on the light quark

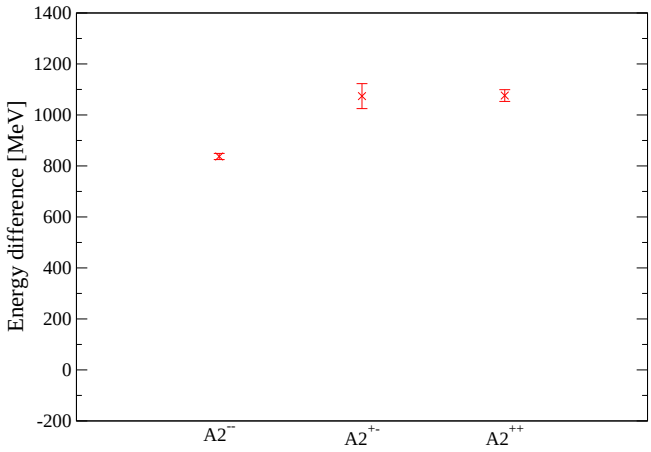

Figure 5.11: Ground states in the A_2 representation, corresponding to states of spin 3. To our knowledge there are no spin 3 states known experimentally.

masses is rather mild and they use simple linear fits for the extrapolations. For excited states, a larger discrepancy might be observed, especially for states close to or above multi-particle thresholds. In addition, calculations at multiple lattice spacings will have to be performed to investigate discretization effects. When changing the lattice spacing, we will need to retain a similar spatial extent of our quark sources and sinks. We comment further on this in Appendix B. Notice, that multiple lattice spacings might also be useful to identify the continuum spins of excitations, as the overlap to other spin states should be suppressed by powers of the lattice spacing for all our interpolators [86]. Finally, one should also investigate finite volume effects. This last step will be necessary to make sure that we obtain the correct picture in the presence of scattering states. Also, some of the higher excitations may need a substantially larger volume than the ground states. Fortunately, the large repository of gauge configurations generated by the MILC collaboration should enable us to perform these extrapolations in a controlled manner. In addition to calculations on further ensembles, an improved action for heavy quarks which includes interactions of dimension 6 and 7 has been presented in [150]. While this approach should be especially beneficial for simulations of bottomonium, it would also be useful to use this action for future calculations of the excited state spectrum of charmonium.

Chapter 6

The spectrum of light-quark baryons

Within the BGR Collaboration, the ground and excited state spectrum of baryons has been studied within the quenched approximation [151, 85] and, more recently, also on dynamical CI configurations [6, 7, 5]. In this chapter, we describe the baryon interpolators used for quenched and dynamical spectroscopy on CI lattices. We present results for baryon ground states and our emphasis will be on channels where we would like to determine the axial charges G_A. In particular, this chapter serves as the basis for the discussion of nucleon and hyperon axial charges in Chapter 7. In addition, we will briefly comment on a general issue which has been a topic of vital discussions in recent years: The determination of the first excited state of the nucleon, the *Roper resonance*.

A local interpolator for the nucleon has the following form

$$O_N = \epsilon_{abc}\,\Gamma_1\,u_a\,\left(u_b^T\,\Gamma_2\,d_c - d_b^T\,\Gamma_2\,u_c\right)\,. \tag{6.1}$$

Exchanging light quarks for strange quarks we obtain interpolators for the Σ and Ξ baryons

$$O_\Sigma = \epsilon_{abc}\,\Gamma_1\,u_a\,\left(u_b^T\,\Gamma_2\,s_c - s_b^T\,\Gamma_2\,u_c\right)\,, \tag{6.2}$$

$$O_\Xi = \epsilon_{abc}\,\Gamma_1\,s_a\,\left(s_b^T\,\Gamma_2\,u_c - u_b^T\,\Gamma_2\,s_c\right)\,. \tag{6.3}$$

Table 6.1 shows the relevant Dirac structures for nucleon-type interpolators. All three types couple only to the spin $\frac{1}{2}$ states, but they have have different diquark structures: Interpolators χ_1 and χ_3 contain a scalar diquark (which is sometimes also labeled "good" diquark as there is a pronounced attractive interaction for scalar diquarks), while interpolator χ_2 contains a pseudoscalar diquark. Interpolators χ_1 and χ_3 couple mainly to the

Name	Γ_1	Γ_2
χ_1	$\mathbb{1}$	$C\gamma_5$
χ_2	γ_5	C
χ_3	$i\mathbb{1}$	$C\gamma_t\gamma_5$

Table 6.1: Nucleon-type interpolators (for N, Σ, Ξ) from [85] as used for the analysis of dynamical CI configurations. C denotes the charge conjugation.

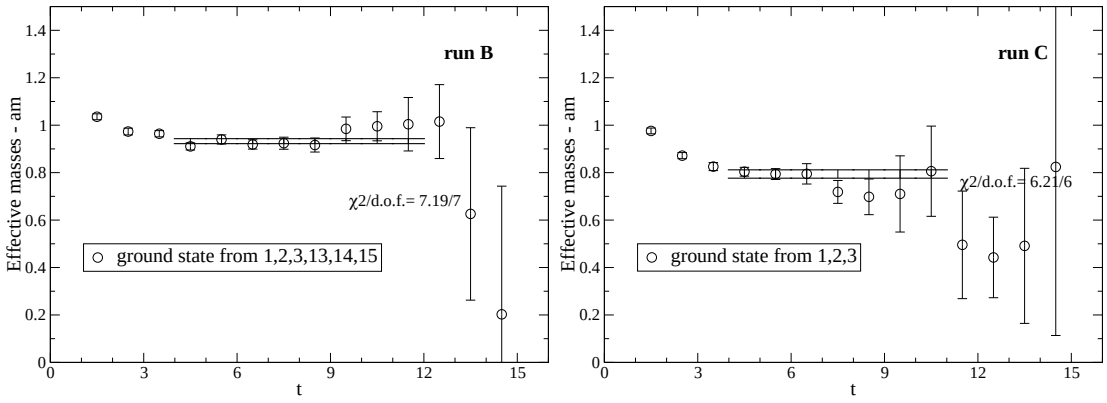

Figure 6.1: Nucleon effective masses for dynamical CI runs B (left-hand side) and C (right-hand side). In addition to the data, results from fits to the eigenvalues of the generalized eigenvalue problem are displayed.

nucleon ground state, interpolator χ_2 predominantly to excited states of both positive and negative parity [151, 85]. For a more detailed discussion please refer to [151].

For the delta-baryon the following interpolator is considered:

$$O_{\Delta,k} = \epsilon_{abc}\, u_a \, \left(u_b^T \, C \, \gamma_k \, u_c\right) \ , \quad k = 1,\, 2,\, 3 \ . \tag{6.4}$$

This interpolator has overlap with both spin $\frac{1}{2}$ and spin $\frac{3}{2}$ states [85], which necessitates a spin $\frac{3}{2}$ projection for the Rarita-Schwinger field, given in our case by

$$P^{\frac{3}{2}}_{\mu\nu}(p) = \delta_{\mu\nu} - \frac{1}{3}\gamma_m u \gamma_n u - \frac{1}{3p^2}\left(\gamma \cdot p \gamma_\mu p_\nu + \gamma_\nu p_\mu \gamma \cdot p\right) \ . \tag{6.5}$$

All interpolators are projected to both positive and negative parity using the projection operators $P^{\pm} = \frac{1}{2}\left(\mathbb{1} \pm \gamma_t\right)$. Data from both branches is subsequently folded to enhance the signal. In addition to the different spin structure, we use Jacobi-smeared sources of two widths with approximately Gaussian shape to create a larger basis of interpolators. For details of the sources used in baryon spectroscopy with CI quarks please refer to [85] and to Appendix C.

6.1 Results for nucleon and delta baryons

Let us start our discussion with the nucleon, where the best signal can be obtained. Figure 6.1 shows effective masses of the nucleon ground state from runs B and C, using the interpolators indicated in the legends[1]. In addition to the data, we display the error bands resulting from correlated fits in the range indicated by the black lines. In both cases the correlated fits lead to a reasonable χ^2/d.o.f., which we indicate in the figure. Excited state contributions to the nucleon ground state are clearly visible at small separations in Euclidean time and correlated fits starting at $t < 4$ will lead to a bad χ^2. This plays a role in the discussion of our preliminary results for the axial charge G_a in Chapter 7, where we will need to ensure that contributions from excited states are sufficiently suppressed. We would like to point out that single diagonal correlators show even much larger contributions from higher energy states.

[1]For an explanation of the numbers see Table VI in [5].

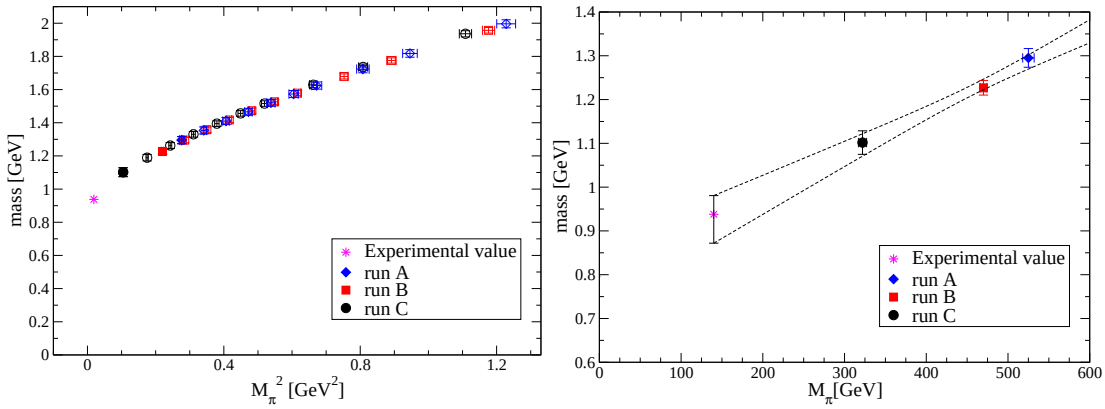

Figure 6.2: Nucleon masses from dynamical CI runs. On the left-hand side we display our results for run A-C including partially quenched data (open symbols) compared to the nucleon ground state (magenta star). On the right-hand side we use a purely empirical fit form, which is linear in the pion mass. For a discussion of this unusual approach please refer to the text. The data has been obtained from a matrix of interpolators 1, 2, 3, 13, 14, 15 for all three runs.

In Figure 6.2, we display the results of our eigenvalue fits for all three dynamical CI runs, including partially quenched data. While the left panel shows the results plotted over M_π^2, the right panel shows just the dynamical points plotted over M_π. In [152, 153] it was noticed that lattice data for the nucleon from several groups is described surprisingly well by a simple fit linear in the pion mass. We checked if this observation is true for our data as well and the corresponding plot, including a linear fit, is shown in the right panel of Figure 6.2. While more data is needed to constrain the fit, our current results show a similar trend.

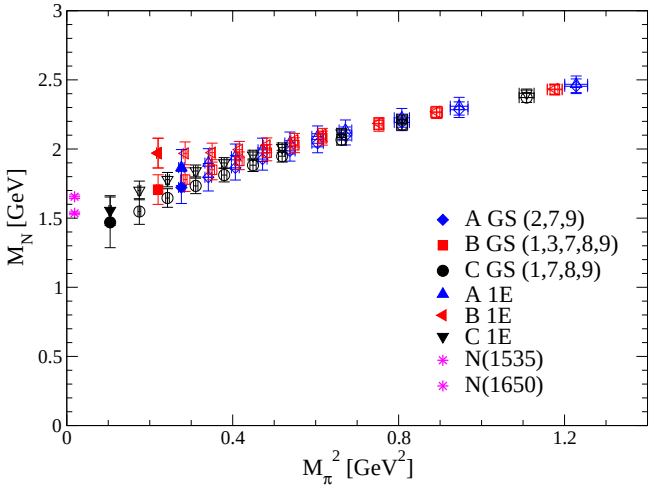

Figure 6.3: The energy levels corresponding to the lowest (GS) and first excited (1E) states in the negative parity nucleon channel from runs A-C compared to the $N(1535)$ and $N(1650)$. Partially quenched data is indicated by open symbols. The data is taken from the talk corresponding to [8].

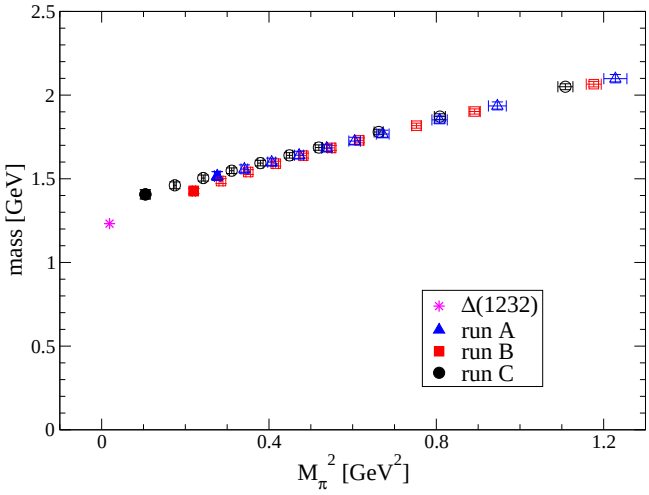

Figure 6.4: Masses of the Δ^{++} from dynamical CI runs. We display our results for run A-C including partially quenched data (open symbols) compared to the $\Delta(1232)$ (magenta star). The data has been obtained from a matrix of interpolators 1, 2, 3, 4 for all three runs.

Let us now turn our attention to the negative parity nucleon channel. Figure 6.3 shows some recent results for the two lowest energy levels presented in the talk corresponding to [8]. In general, effective mass plateaus for the negative parity states are noisy and the possible fit range is very limited. As we were not able to use the same combination of interpolators for each run, different combinations have been used. Typically, fits can be performed in the Euclidean time interval $3 \leq t \leq 7$. At larger Euclidean times, contributions from the positive parity nucleon state and possibly also from back-to-back scattering states [154] are present, which leaves only a narrow window for a fit. Due to the bad quality of our mass plateaus and our experience with the positive parity states, we did not attempt a calculation of the axial charge of negative parity nucleon states in Chapter 7. We will briefly comment on a possible improvement in that chapter.

In addition to the nucleon, we also take a look at the delta resonance. In Figure 6.4 we present the results. While the statistical errors are in general slightly larger than for the nucleon and the fit ranges are a little bit shorter, reasonable fits can be obtained for various combinations of interpolators with different quark smearing. From this point of view, a determination of the axial charge G_a should be feasible. Before we move on to our results for hyperons, we will make some brief remarks on determinations of the Roper resonance from lattice QCD.

6.1.1 The Roper resonance from lattice QCD

In this section, we would like to briefly comment on the current status of extracting the Roper resonance from lattice simulations. In quenched simulations with CI fermions [151, 83, 85], the first excited state in the positive parity nucleon channel was systematically too high. In particular, the state corresponding to the negative parity $N(1535)$ was observed with a smaller mass than the first excited state in the nucleon channel, although the experimental Roper resonance, or $N(1440)$, has a substantially lighter mass. While several studies using the variational method found this reverse level ordering [151, 83, 85, 155, 156, 87], the authors of [71, 76] identified a positive parity state which, within

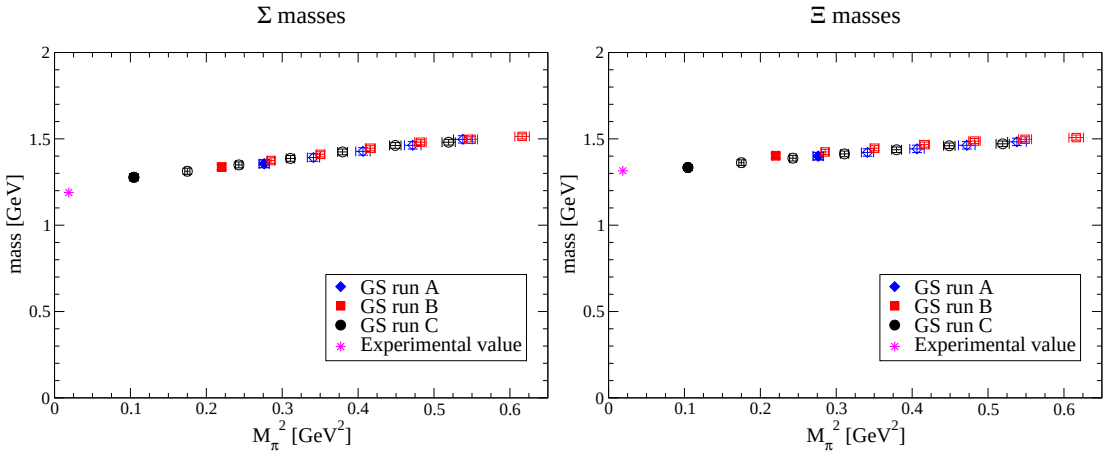

Figure 6.5: Masses of the Σ and Ξ hyperons from dynamical CI runs. We display our results for run A-C including partially quenched data (open symbols) compared to the experimental ground states (magenta stars). The data has been obtained from a matrix of interpolators 1, 2, 3, 13, 14, 15 for all three runs.

large statistical errors, rapidly approaches the Roper resonance at light quark masses. Recently, Mahbub *et al.* [93] observed a similar behavior with the variational method using a large basis of Gaussian smeared interpolators.

It would be desirable to confirm this behavior using the variational method on dynamical ensembles. In [90], results from anisotropic lattices with 2 flavors of light quarks have been reported. In their range of pion masses, the first positive parity excited state has a substantially larger mass than the negative parity states corresponding to the $N(1535)$ and the $N(1650)$. Our data for the excitations in the nucleon channel is rather noisy and an extraction of the first positive parity nucleon excitation is somewhat ambiguous. In particular, while the results for mesons and for baryon ground states from all three dynamical runs show consistent results, the situation is different for some of the excited states, including the positive parity nucleon channel. While this may just be a problem of statistics, dynamical results from a single ensemble should always be taken with a grain of salt. For a thorough analysis, multiple dynamical points are needed and more than one volume and lattice spacing are desirable.

6.2 Results for Σ and Ξ hyperons

In addition to hadrons which are made from light up and down quarks alone, we also studied mesons and baryons containing strange quarks. For this thesis, we restrict our presentation to data for the ground states of the Σ and Ξ hyperons. Figure 6.5 shows masses for these baryons. The results for the Σ show a reasonable agreement with experiment. Like in the nucleon case, an extrapolation linear in m_π^2 would lead to results slightly larger than the physical ground state. For the Ξ such a simple extrapolation leads to results in agreement with the experimentally observed ground state. As our strange valence quark masses have been determined through the mass of the Ω baryon, the spectrum results for the octet hyperons are a nice cross-check for this determination. This concludes the chapter on baryon spectroscopy and we will use these results from baryon two-point functions in the next chapter, where baryon axial charges are determined.

Chapter 7

Baryon axial charge from lattice QCD

The axial charge of the nucleon, or more precisely the ratio $\frac{G_a(q^2=0)}{G_v(q^2=0)}$ has been determined to a high precision from neutron β decay, $\frac{G_a(0)}{G_v(0)} = 1.2695(29)$ [15]. In general, the axial form factor $G_{a,BB'}$ for an octet baryon is given by

$$\langle B|A_\mu(q)|B\rangle = \bar{u}_B(p')\left(\gamma_\mu\gamma_5 G_{a,BB'}(q^2) + \gamma_5 q_\mu \frac{G_p(q^2)}{2M_B}\right) u_B(p)\mathrm{e}^{-iq\cdot x} \ , \qquad (7.1)$$

where G_p is the induced pseudoscalar form factor. The axial charge is defined as the value of the axial form factor at zero momentum transfer $G_{a,BB'}(q^2 = 0)$. In the following, we will omit the indices B and B' when referring to the nucleon. For the nucleon in the chiral limit, the Goldberger-Treiman relation [157] connects the axial charge to the pion decay constant f_π, the pion-nucleon coupling constant $g_{\pi NN}$ and the nucleon mass M_N

$$G_a = \frac{f_\pi g_{\pi NN}}{M_N} \ . \qquad (7.2)$$

Away from the chiral limit, this relation is still approximately fulfilled. If one assumes the conservation of the vector current (which is the case for mass-degenerate light quarks $m_u = m_d$), also referred to as CVC, the nucleon axial charge is also related to the polarized quark distributions in the proton: $G_a = \Delta u - \Delta d$ [158]. In an isovector combination, disconnected contributions will cancel, making high-precision lattice computations feasible. As pointed out in [159], this is also related in a direct way to the fraction of the nucleon spin arising from the spin of the quarks.

The χPT expressions relevant to the nucleon axial charge have been calculated in references [160, 161], where finite volume effects are taken into consideration. While a recent simulation with domain wall fermions [162] finds considerable finite volume effects and scaling in $m_\pi L$, volume effects calculated in χPT lead to differing conclusions. Trying to attribute this difference to excited state contaminations arising from finite separation in Euclidean time, Tiburzi [163] estimates the effects of such contaminations and suggests that they would lead to an over-estimation of G_a rather than an under-estimation. He also suggests to study G_a using the variational method. Lattice results for the nucleon axial charge have furthermore been presented in [164] and [154]. For a recent review, please refer to the review by Renner [165].

So far, only one group has reported results on the axial couplings of sigma and cascade hyperons [166]. The corresponding Chiral Perturbation Theory calculations can be found

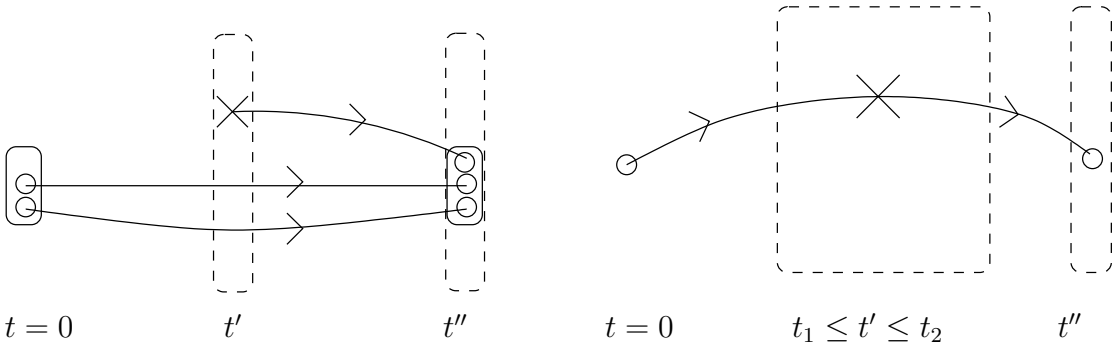

Figure 7.1: Different possibilities for the calculation of sequential quark propagators. On the left-hand side, sequential sources are built from specific diquark propagators, while on the right-hand side, the propagators are calculated for each possible insertion separately. Please refer to the text for additional comments. For an illustration of the full baryon three-point function see Figure 7.2.

in [167, 168]. In [169] input from experiment and lattice QCD is used to determine the unknown parameters in the χPT expansion and predict the mass dependence and values of the axial charges in the chiral limit.

In the next section, we will explain the setup for calculations of baryon axial charges using CI fermions and the variational method. We will then move on and present results from lattice calculations of the axial charges of the nucleon and of Σ and Ξ hyperons. In the final part of this chapter, we will comment on our results and make some remarks about further quantities of interest.

7.1 Details of our calculational setup

Assuming mass-degenerate up and down quarks[1], the conservation of the vector current enables us to only consider the non-flavor changing current insertion [158]

$$\begin{aligned} 2A^3_\mu &= \left(A^u_\mu - A\mu^d\right) \ , \\ A^u_\mu &= \bar{u}\gamma_\mu\gamma_5 u \ , \\ A^d_\mu &= \bar{d}\gamma_\mu\gamma_5 d \ , \end{aligned} \tag{7.3}$$

in which u denotes an up quark and d denotes a down quark. In the following, we will show how three-point functions with insertions like those in Equation 7.3 can be evaluated on the lattice.

7.1.1 Sequential quark-propagators

For the calculation of three-point functions on the lattice we will use so-called *sequential propagators*. In [158], two methods for the calculation of sequential quark propagators are presented. Figure 7.1 illustrates these two approaches. *A priori* it is not clear which approach needs less computations for our objective. Therefore, we briefly summarize the main features of each approach for the example of nucleon interpolators. For an illustration of the full baryon three-point function please refer to Figure 7.2.

[1]This is an assumption which is fulfilled only approximately in Nature. For the status of light-quark mass determinations please refer to the Review of Particle Physics [15].

Sequential sources from diquark propagators

This possibility is illustrated on the left-hand side of Figure 7.1. The sequential sources are constructed from *diquark propagators*. The diquarks are built from regular quark propagators calculated on smeared sources. Depending on the details of the basis, a certain number of sequential sources will be needed.

- For nucleon-type interpolating fields we would like to use the basis introduced in Chapter 6, which has been successfully applied to baryon spectroscopy. Each combination of interpolators χ_1, χ_2 and χ_3 forms new diquark propagators and therefore results in a new set of sequential propagators. Even if we restrict ourselves to positive parity using χ_1 and χ_3 alone, there are still 4 possible combinations.

- For each different quark smearing appearing in the sequential propagators, a new set of sequential propagators is needed. Notice that two different quark smearings already lead to 32 combinations in the most general case[2] of 8 different baryon smearings. This number could be reduced to 4 by only allowing an overall narrow or wide smearing for each quark in the baryon.

- Each new sink momentum will require new sequential sources. As we are only interested in the axial charge G_a (i.e. $q^2 = 0$), this is not an issue in our case. For a study of form factors at non-vanishing momentum transfer, this limits the number of accessible momenta.

- In the case of the nucleon we need two sets of sequential propagators, one for an up-quark-removed diquark and one for a down-quark-removed diquark.

- If we are only interested in certain current insertions, we can reduce the number of open Dirac indices on the diquark-propagators by applying the appropriate projection operators at the sink [158]. In our case, we are interested in the vector and axial-vector current insertions. This again leaves us with two distinct sets of sequential propagators.

In addition, a part or even the whole set of sequential propagators will have to be recalculated whenever the contractions needed for the calculation of a new observable are different. In our case this is relevant for the calculation of the axial charge of Σ and Ξ hyperons. We will now take a look at a second possibility which does not have this disadvantage.

Sequential sources from single quark propagators

On the right-hand side of Figure 7.1, the sequential propagators are constructed from a single quark propagator using the appropriate current insertion and a specific momentum transfer.

- For each type of quark smearing at the source, a new set of sequential propagators is needed.

- For each different current insertion, a new set of sequential propagators is needed.

[2] A factor 4 comes from the source and a factor 8 from the sink, where the sequential propagator contains three quark lines.

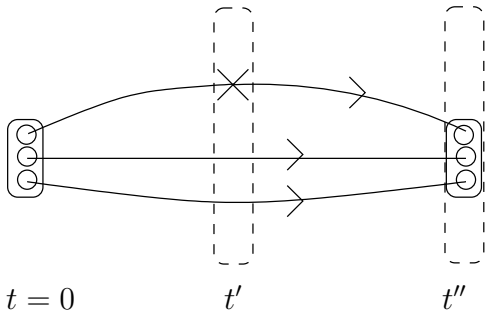

Figure 7.2: Illustration of the full baryon three-point function.

- For each momentum transfer q^2, a new set of sequential propagators is needed. In our case this is no issue, as the only momentum transfer we are interested in is $q^2 = 0$. In the more general case of form factors at non-vanishing momentum transfer, sequential sources from single propagators become very expensive and are effectively no longer an option.
- For each insertion timeslice, new sequential propagators will be needed. For a symmetric source-sink construction one expects a plateau at insertions which are separated sufficiently far from both the source and the sink location. One can therefore restrict possible insertion locations to a few timeslices.

From this discussion, it is obvious, that which approach is computationally cheaper depends on the physics objective. In our case, we want to use two different insertions and two widths of smearing for three different interpolator types. As we are using a rather coarse lattice, a small number of insertion timeslices should be enough. Therefore, even just considering the nucleon case, the second approach using sequential sources from single quark propagators is slightly cheaper. Moreover, these propagators can subsequently be used for other hadrons and for the calculation of transition form factors. As an added bonus, this method will enable us to systematically investigate the effect of moving source and sink closer together, as the sink location remains variable with this method. In [163], the expectation that contaminations from excited states lead to an overestimation of G_a has been expressed. Varying the sink location at fixed source location, thereby reducing the separation between the source/sink and insertion timeslices, will help us to investigate the effects of excited states on the determination of the axial charge of the nucleon. We will comment further on this in Section 7.4. In principle, also the sink momentum can be varied at fixed momentum transfer.

7.1.2 Renormalization constants and vector charges

To relate lattice operators, which receive a finite renormalization, to their continuum counterparts, we need to estimate the renormalization factors Z_Γ of the bilinear currents in question. In general, we have to multiply the lattice result G_Γ^{lat} by the appropriate renormalization factor to obtain values that can be compared with results extracted from experiments

$$G_\Gamma^{phys} = Z_\Gamma G_\Gamma^{lat},$$

which are typically given in the *modified minimal subtraction* ($\overline{MS}$) renormalization scheme.

Run	Z_V bilinears	Z_V 3-pt functions
A	0.818(2)	0.803(2)
B	0.826(1)	0.792(2)
C	0.829(1)	0.77(1)

Table 7.1: Values of the vector renormalization constant Z_V from [170] compared to the estimates from nucleon three-point functions. For details on run A-C please refer to Appendix C.

For dynamical CI fermions, these renormalization constants have been estimated using local bilinear quark field operators in [170]. It would however be useful to have an independent estimation of these constants from a different method. In the case of the vector current, one can estimate the constant Z_V by calculating the vector charge G_V defined in analogy with (7.1) via

$$\langle B|V_\mu(q)|B\rangle = \bar{u}_B(p')\left(\gamma_\mu G_V(q^2) + q_\nu \sigma_{\nu\mu}\frac{G_T(q^2)}{2M_B}\right)u_B(p)\mathrm{e}^{-iq\cdot x}\ , \tag{7.4}$$

as $G_V(q^2 = 0)$. This quantity has to be 1 in the continuum, as it is related to the electric charge of the proton in the limit of equal quark masses [158].

For lattice fermions with exact chiral symmetry (i.e. Neuberger's Overlap fermions [31, 32], see also 2.5.1), the axial vector renormalization constant Z_A and the vector renormalization constant Z_V have to be equal. For lattice fermions which only fulfill the Ginsparg-Wilson relation approximately (see Section 2.5), there should be small deviations from this. To obtain an independent estimate of Z_V, we use a ratio of two-point over three-point functions

$$R^{(k)} = \frac{\sum_l \sum_m \psi_l^{(k)} C(t)_{lm} \psi_m^{(k)}}{\sum_i \sum_j \psi_i^{(k)} T_V(t,t')_{ij} \psi_j^{(k)}} = Z_V\ ,$$

where $C(t)$ is the matrix of two-point correlation functions and $T_V(t,t')$ is the matrix of three-point correlators with a vector insertion. The eigenvectors ψ are the ones obtained from a variational analysis of $C(t)$. We then compare with the preliminary estimates from [170]. Table 7.1 lists the respective values from both local quark bilinears and from our determination. While the two methods seem to agree within $2-3\%$ for runs A and B, there is a rather large discrepancy between both values from run C. Notice also that two different methods for the determination of the renormalization constants are presented in [170] which only agree after a chiral extrapolation of the results is performed. At the same time, the ratio $\frac{Z_A}{Z_V}$ determined from the values in [170] is almost identical for both methods used and also stable under chiral extrapolation of the results.

In our determination of the axial charge from run C, we will encounter what we suspect to be large finite volume effects. Notice that the value of Z_V obtained from the nucleon three-point functions might be plagued by the same effects. As we can not calculate Z_A from baryon three-point functions, we therefore always use the ratio $\frac{Z_A}{Z_V}$ from [170]. These renormalization constants from local bilinear currents are currently our best choice. In the next section, we discuss in detail which ratios we measure on the lattice to obtain the renormalized axial charge G_a.

7.2 Nucleon axial charge from dynamical CI fermions

The usual approach in the literature [158, 162] is to extract the nucleon axial charge from ratios of G_A over G_V

$$G_A = \frac{Z_A}{Z_V} \frac{T_A^3(t,t')}{T_V^4(t,t')} \,, \tag{7.5}$$

using single correlation functions built from either smeared quarks or gauge fixed box or wall sources. This approach has the advantage that some of the systematic errors entering the lattice determination will cancel. Figure 7.3 shows an example from 50 configurations of run C for ratios of diagonal correlators obtained from our smeared quark sources. We plot results from all interpolators of types χ_1 and χ_2. While the results from different interpolators agree within their statistical errors and stable plateaus are observed for each correlator, the errors on such a small number of configurations are rather large.

To make full use of our variational basis, we apply Equation (3.10) to this problem to obtain an expression for G_A:

$$G_A = \frac{Z_A}{Z_V} \frac{\sum_i \sum_j \psi_i^{(k)} T_A^3(t,t')_{ij} \psi_j^{(k)}}{\sum_l \sum_m \psi_l^{(k)} T_V^4(t,t')_{lm} \psi_m^{(k)}} \,. \tag{7.6}$$

Figure 7.4 shows the plateau for the axial charge of the nucleon from runs B and C extracted from such a ratio. The horizontal lines denote the results from a linear fit in the displayed range. Notice that we observe a plateau in the full range of points we calculated. For all three ensembles, we choose timeslice 9 for the position of the sink. This corresponds to a source-sink separation of roughly 1.2 fm. For run B, we currently only have data for insertion timeslices 5 to 9. Instead of assuming that the central value at 5 is the physical one, we perform a linear fit to all three values displayed.

We compare our data to recent results from domain wall fermions [162] in Figure 7.5. The upper plot shows the results for G_a plotted over the square of the pion mass m_π^2. While results at large pion masses lead to values close to the experimental value, the result from run C deviates substantially from this behavior. The same is true for the

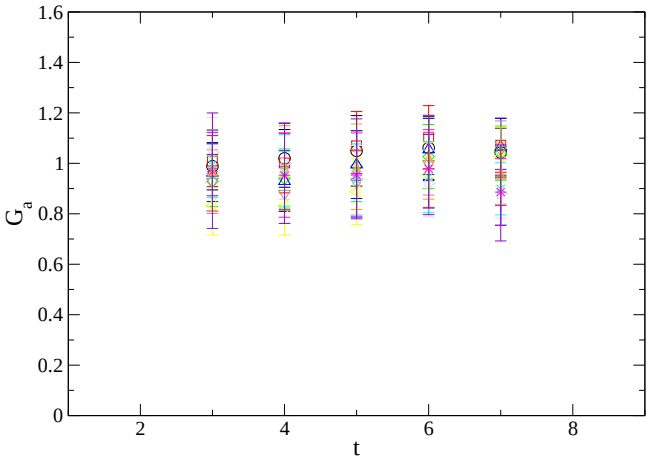

Figure 7.3: Ratios of diagonal correlators (from Equation (7.5)) for nucleon interpolators χ_1 and χ_3 and various combinations of Gaussian quark smearing.

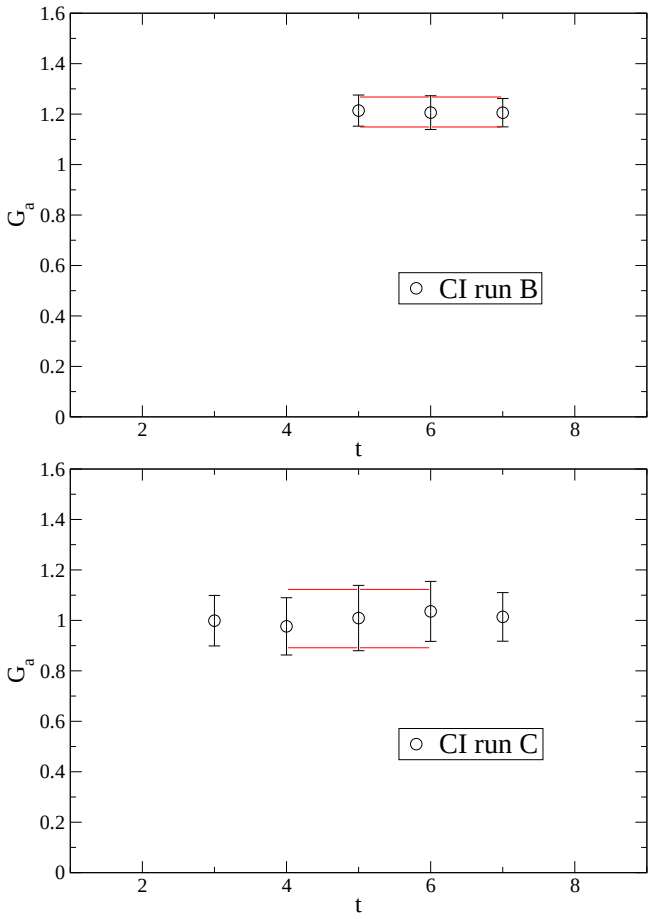

Figure 7.4: Example plots to illustrate typical plateaus observed with a variational basis for a source-sink separation of $\approx 1.2\,\mathrm{fm}$. In the upper plot, data from run B is shown, while in the lower plot the results from run C can be seen.

domain wall data and this behavior seems to be a universal feature associated with finite volume effects [162, 165]. In the lower part of the figure we therefore plot the results for G_a over $M_\pi L$, where L corresponds to the spatial extent of the lattice. This plot can be directly compared to Figure 3 of [162].

Before we move on to calculations for hyperons, let us briefly comment on the sink-dependence of our results. While results from run A and B are rather insensitive to the sink location in the region explored (timeslices 9-13)[3], a systematic shift upwards can be observed for run C when reducing the distance between the source and the sink from 1.2 fm to 0.9 fm. We want to point out that this does not affect the quality of the plateau which still stretches over the entire region of insertion times. Taking a look at the nucleon two point functions, contributions from excited state to the ground state of the variational analysis are visible up to timeslice 4. This is an indication that excited states may indeed be responsible for measuring a larger value of G_a if excited state contributions are not sufficiently suppressed. However, with our current accuracy from just 50 configurations, the statistical errors from our preliminary dataset are by far too large to make a stronger and more quantitative statement. We plan to revisit this once

[3]We observe no systematic shifts as we change the sink location. At the same time, the errors increase as the source-sink separation is increased.

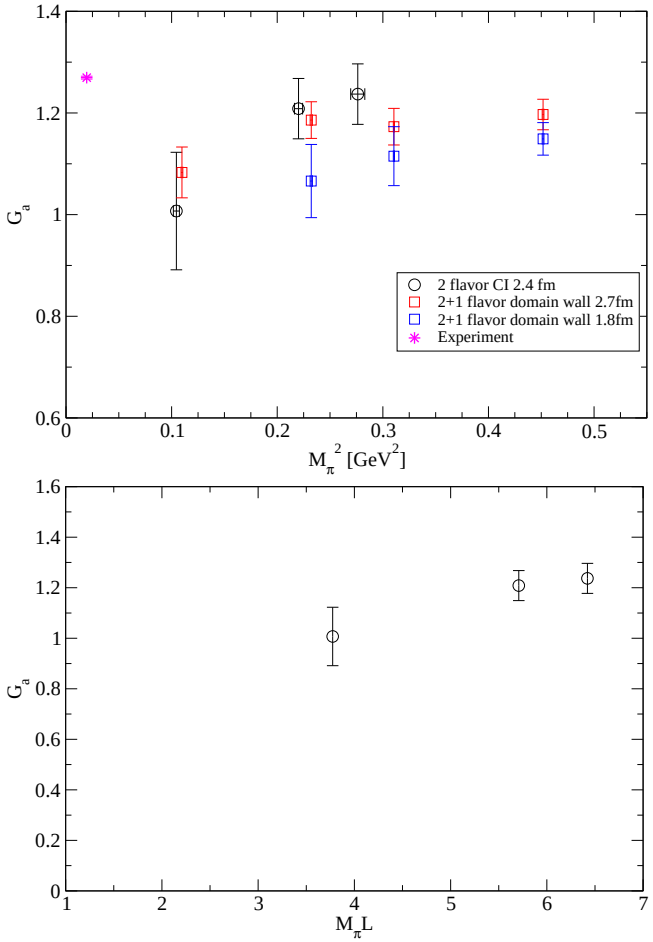

Figure 7.5: We compare the results for G_a to a recent determination from domain wall fermions. Our data is labeled as "2 flavor CI". Results from 2+1 flavor domain wall fermions are taken from Yamazaki et al. [162]. In the upper plot, we plot the results over m_π^2. Towards lower quark masses finite volume effects are clearly visible. In the lower plot we display our data in units of $M_\pi L$.

our statistics allows less ambiguous fits at multiple separations in Euclidean time.

7.3 Hyperon axial charges

In this section we will present results for a calculation of hyperon axial charges. For the Σ and Ξ hyperons we adopt the following definitions:

$$\left\langle \Sigma^+ | A_\mu^3 | \Sigma^+ \right\rangle - \left\langle \Sigma^- | A_\mu^3 | \Sigma^- \right\rangle = G_{\Sigma\Sigma} \bar{u}^\nu \gamma_\mu \gamma_5 u^\nu \ , \tag{7.7}$$

$$\left\langle \Xi^0 | A_\mu^3 | \Xi^0 \right\rangle - \left\langle \Xi^- | A_\mu^3 | \Xi^- \right\rangle = G_{\Xi\Xi} \bar{u}^\nu \gamma_\mu \gamma_5 u^\nu \ . \tag{7.8}$$

Again, no disconnected contributions appear in the isovector quantities and the calculation proceeds similar to the nucleon case. In particular, no additional sequential propagators are needed for these quantities.

Figure 7.6 shows our results for the axial charge of the Σ hyperon. We compare our data to [166] and we can see a quantitative agreement in the full range of masses. Unlike

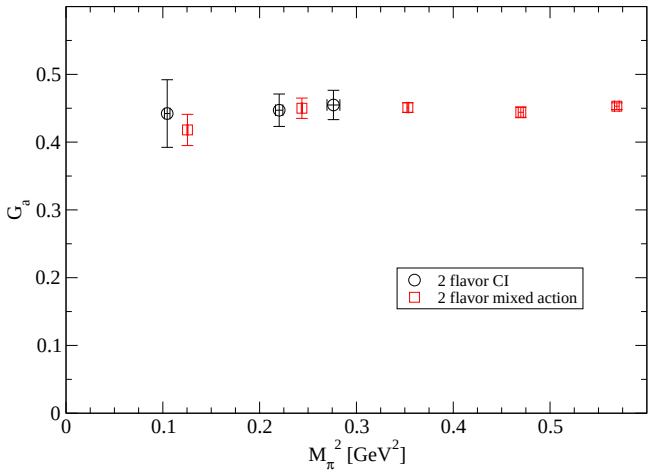

Figure 7.6: Results for the axial charge of the Σ hyperon compared to the mixed action results by Lin and Orginos [166].

in the nucleon, no decrease is observed towards the chiral limit. Our purely statistical errors on the preliminary dataset of 50 configurations are still rather large but can be substantially reduced by using our full statistics.

Figure 7.7 shows a similar plot for the Ξ hyperon. Again the data agrees nicely with the results from [166]. In this case our value corresponding to the smallest pion mass shows a slight decrease towards the chiral limit, but the error bars are large and this may be an effect from our limited statistics.

7.4 Summary and outlook

We have presented preliminary results from a calculation of baryon axial charges using a full variational basis to efficiently suppress contaminations from excited states. We used a basis of baryon interpolators with different Dirac structures and two different smearing widths for the quarks. The results are in good agreement with the literature and we obtain clear plateaus for ratios calculated with the method of [91]. Provided the signal for the states in question is strong enough, this method can also be applied to several other quantities of interest. In this section we discuss a few possible applications.

- **Axial charge of the delta baryon:** The conventional definition [171] of the axial charge of the Δ resonance is given by

$$\left\langle \Delta^{++}|A_\mu^3|\Delta^{++}\right\rangle - \left\langle \Delta^{-}|A_\mu^3|\Delta^{-}\right\rangle = G_{\Delta\Delta}\bar{u}^\nu(p)\gamma_\mu\gamma_5 u(p)^\nu \ , \tag{7.9}$$

  where $u(p)^\nu$ is a Rarita Schwinger field. As has been pointed out in [171], it is therefore enough to calculate the connected part of $\langle\Delta^{++}|\bar{u}\gamma_\mu\gamma_5 u|\Delta^{++}\rangle$ to determine $G_{\Delta\Delta}$ on the lattice[4]. This can be done without the need for any additional sequential propagators.

- **Axial charges for negative parity nucleon states:** Takahashi and Kunihiro [154] calculated the axial charges of negative parity nucleon states. More specific,

[4]Notice that this is only sensible as long as the delta resonance can not decay on the lattice. As the Δ resonance decays via a p-wave decay, this is the case for most current lattice simulations.

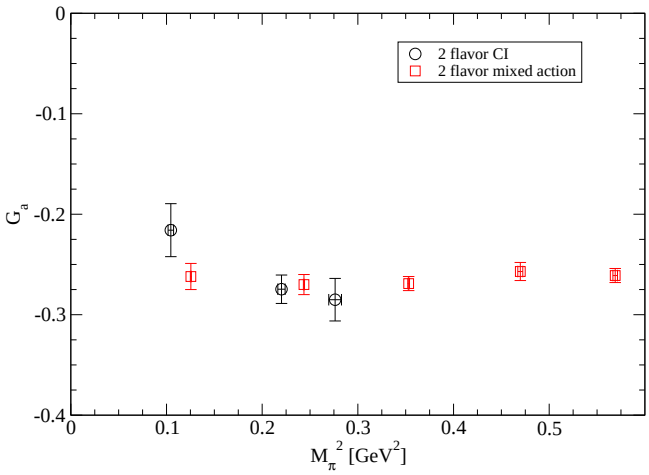

Figure 7.7: Results for the axial charge of the Ξ hyperon compared to the mixed action results by Lin and Orginos [166].

they investigated the axial charges of the $N(1535)$ and the $N(1650)$. While they found a value consistent with zero for the $N(1535)$, they found a value of roughly 0.5 within large errors for the $N(1650)$. This is interesting as values much smaller than 1 are expected under the assumption of effective chiral restoration for excited states [172]. As the axial charges of these states can not be measured in experiment, indirect evidence from the smallness of decays into $N\pi$ is presented in [172]. The lattice offers an opportunity to extract the axial charges directly. Unfortunately, plateaus for the negative parity Nucleon are very short and an extraction with our current data is at best ambiguous. Implementing different boundary conditions as used in [154] may potentially serve to overcome this issue.

- **Transitions :** In addition, our sequential quark propagators could for example be used to calculate three-point functions for the N-Δ or Σ-Λ transitions. So far the only determination we are aware of concerns the axial Nucleon-Delta transition form factor [173].

In general, the method we use can also be applied to three-point functions involving excited states, provided that the signal is good enough to ensure the necessary separation between the source/sink and the current insertion. In addition, the method from [106] discussed in Section 3.7 seems promising for the calculation of baryon three-point functions as expensive sequential quark propagators are not needed anymore, once all propagators are calculated from both the source and the sink timeslice.

Chapter 8

Conclusions and Outlook

In this thesis, the variational method was used to determine properties of both ground and excited state hadrons. For each of the projects presented in the previous chapters, we constructed a suitable basis of interpolating fields for the states of interest. In the case of ground states, the variational basis helps to isolate contaminations from excitations, which leads to effective mass plateaus starting at smaller distances in Euclidean time. This is especially beneficial for channels where the signal is noisy and plateaus are short. As detailed conclusions have been provided in most chapters, we just summarize the most important findings and provide a short outlook.

In Chapter 4 we constructed derivative quark sources and applied them to the spectroscopy of isovector mesons. For this project, we used quenched and dynamical lattices with two flavors of Chirally Improved fermions generated within the BGR Collaboration. We demonstrated that these sources improve the overlap with both ground states and low-lying excitations, depending on the channel. Here, we specifically want to point out their usefulness for the scalar and pseudovector channels. In addition, states of higher spins can be extracted with these sources and we provided some encouraging results for spin 2 mesons. As a possible extension of this project, baryon interpolators could be constructed with the same derivative sources. This is a rather straight-forward procedure and would not require any further expensive calculations. In general, our analysis on dynamical CI configurations would benefit from both, more dynamical ensembles and a higher statistics for current ensembles. As there are several indication for finite volume effects in our data from CI runs (see also Chapter 7), calculations in a larger volume would be useful. We are currently creating further ensembles of dynamical gauge configurations and are planning to extend some of the current runs to reduce the statistical uncertainties. Ultimately, multiple lattice spacings should be used and an extrapolation to the the continuum limit will need to be performed.

In Chapter 5 we used a large basis of regular and hybrid charmonium interpolators for an exploratory study of charmonium excitations. We identified states of interest in Section 5.1 and demonstrated that these physics objectives can be studied with our approach. In particular, the dynamical results we obtain are competitive with previous quenched results. We can now use the large number of gauge configurations created by the MILC collaboration to systematically control the extrapolations needed for a comparison with experiment. Previous systematic studies have mostly been restricted to ground states. Studies using the variational method have either used quenched gauge configuration or have lacked the necessary extrapolations.

So far, we were concerned mainly with the determination of hadron masses. In Chapters 6 and 7, we calculated the the baryon correlators needed for an extraction of axial

charges. We demonstrated that our method efficiently suppresses contaminations from excited states and we presented preliminary results for the axial charge of the nucleon and of Σ and Ξ hyperons. To our knowledge, this is the first time that the variational method has successfully been applied to extract axial charges. We also outlined other directions of research and are currently extending our calculations to a larger statistics.

In Section 3.7 we briefly described a recently proposed method [106] which seems quite promising for several of our projects. We would like to investigate this approach and combine it with some of the methods used in this thesis. In our opinion, this new method may be especially well suited for studies of baryon form factors. A subset of propagators needed for such a project can also be used for the simpler case of meson spectroscopy or studies of meson three-point functions. We believe these projects would be good starting points for incorporating the new techniques.

Excited state spectroscopy is a challenging and active topic of research for lattice theorists and impressive progress has been made in recent years. I hope that the projects presented in this thesis will stimulate further research and thereby contribute a small share to the advancement of the field.

Appendix A

Interpolators for mesons and baryons

A.1 Tables of interpolators for light-quark spectroscopy

In this appendix, we collect tables of interpolators used for the different projects. For the construction of the quark sources from which those interpolators are build, please refer to Section 3.6.2. In the case of the two-dimensional (E) and the two three dimensional representations (T_1 and T_2), all correlators are summed over the independent components.

A.1.1 Meson interpolators with smeared CI quarks

Here we present the meson interpolators used on quenched and dynamical CI configurations. All lattice interpolators may also couple to states with higher angular momentum J [99, 86], as discussed in 3.5. We denote Gaussian smeared quarks by subscripts n and w standing for narrow and wide smearing of u and d quarks. The subscript ∂_i denotes derivative smearing in the i-direction. Where they appear, repeated indices i are summed over the spatial directions 1,2,3. The time direction is 4 and the corresponding Dirac matrix is γ_4. Where necessary, we explicitly show the (anti)symmetrizations needed to obtain the proper charge conjugation for the corresponding neutral mesons.

Tables A.1 and A.2 show the interpolators used for the spin 0 (A_1 representation) and spin 1 (T_1 representation) mesons. Notice that the numbers have been chosen such that interpolators from [3] which have been used in 4.2 and new interpolators used in 4.3 can all be found in the tables presented here. For a given component i of the interpolators involving the Levi-Civita Tensor ϵ_{ijk}, the indices j and k run over the two non-vanishing entries which are summed. Again the final results for interpolators are summed over all directions i.

Table A.3 shows the interpolators in the T_2 representation which are used in 4.3 for the spectroscopy of spin 2 mesons. Notice that we omitted the appropriate symmetrization here. As an example, $|\epsilon_{ijk}|\overline{u}_{\partial_k}\gamma_j\gamma_4 d_w$ has to be read as $|\epsilon_{ijk}|\,(\overline{u}_{\partial_k}\gamma_j\gamma_4 d_w - \overline{u}_w\gamma_j\gamma_4 d_{\partial_k})$.

Table A.4 lists the interpolating fields from the E representation used for the analysis of spin 2 mesons. Just like for the case of the T_2 representation, we again omit the symmetrization in this list. The non-vanishing coefficients Q_{ijk} for the interpolators in

Number	$1\,0^{++}$	$1\,0^{-+}$
1	$\overline{u}_n d_n$	$\overline{u}_n \gamma_5 d_n$
2	$\overline{u}_n d_w$	$\overline{u}_n \gamma_5 d_w - \overline{u}_w \gamma_5 d_n$
3	$\overline{u}_w d_w$	$\overline{u}_w \gamma_5 d_w$
4		$\overline{u}_n \gamma_4\gamma_5 d_n$
5		$\overline{u}_n \gamma_4\gamma_5 d_w$
6		$\overline{u}_w \gamma_4\gamma_5 d_w$
7	$\overline{u}_{\partial_i} \gamma_i d_n - \overline{u}_n \gamma_i d_{\partial_i}$	$\overline{u}_{\partial_i} \gamma_i\gamma_5 d_n + \overline{u}_n \gamma_i\gamma_5 d_{\partial_i}$
8	$\overline{u}_{\partial_i} \gamma_i d_w - \overline{u}_w \gamma_i d_{\partial_i}$	$\overline{u}_{\partial_i} \gamma_i\gamma_5 d_w + \overline{u}_w \gamma_i\gamma_5 d_{\partial_i}$
9	$\overline{u}_{\partial_i} \gamma_i\gamma_4 d_n - \overline{u}_n \gamma_i\gamma_4 d_{\partial_i}$	$\overline{u}_{\partial_i} \gamma_i\gamma_4\gamma_5 d_n - \overline{u}_n \gamma_i\gamma_4\gamma_5 d_{\partial_i}$
10	$\overline{u}_{\partial_i} \gamma_i\gamma_4 d_w - \overline{u}_w \gamma_i\gamma_4 d_{\partial_i}$	$\overline{u}_{\partial_i} \gamma_i\gamma_4\gamma_5 d_w - \overline{u}_w \gamma_i\gamma_4\gamma_5 d_{\partial_i}$
11	$\overline{u}_{\partial_i} d_{\partial_i}$	$\overline{u}_{\partial_i} \gamma_5 d_{\partial_i}$
12		$\overline{u}_{\partial_i} \gamma_4\gamma_5 d_{\partial_i}$

Table A.1: List of spin 0 meson interpolators (A_1 representation). The numbers in the first column together with the quantum numbers IJ^{PC} label the interpolators uniquely.

the E-representation are given by

$$Q_{111} = \frac{1}{\sqrt{2}} \qquad Q_{122} = -\frac{1}{\sqrt{2}} \ ,$$
$$Q_{211} = -\frac{1}{\sqrt{6}} \qquad Q_{222} = -\frac{1}{\sqrt{6}} \qquad Q_{233} = \frac{2}{\sqrt{6}} \ .$$

For completeness, we also list the interpolators for exotic mesons. Table A.5 shows a list of interpolators with derivative sources which we calculated on our dynamical ensembles.

Number	$1\,1^{--}$	$1\,1^{++}$	$1\,1^{+-}$
1	$\overline{u}_n\gamma_k d_n$	$\overline{u}_n\gamma_k\gamma_5 d_n$	
2	$\overline{u}_n\gamma_k d_w - \overline{u}_w\gamma_k d_n$	$\overline{u}_n\gamma_k\gamma_5 d_w - \overline{u}_w\gamma_k\gamma_5 d_n$	
3	$\overline{u}_w\gamma_k d_w$	$\overline{u}_w\gamma_k\gamma_5 d_w$	
4	$\overline{u}_n\gamma_k\gamma_4 d_n$		$\overline{u}_n\gamma_k\gamma_4\gamma_5 d_n$
5	$\overline{u}_n\gamma_k\gamma_4 d_w - \overline{u}_w\gamma_k\gamma_4 d_n$		$\overline{u}_n\gamma_k\gamma_4\gamma_5 d_w - \overline{u}_w\gamma_k\gamma_4\gamma_5 d_n$
6	$\overline{u}_w\gamma_k\gamma_4 d_w$		$\overline{u}_w\gamma_k\gamma_4\gamma_5 d_w$
7	$\overline{u}_{\partial_k} d_n - \overline{u}_n d_{\partial_k}$	$\overline{u}_{\partial_k}\gamma_5 d_n + \overline{u}_n\gamma_5 d_{\partial_k}$	$\overline{u}_{\partial_k}\gamma_5 d_n - \overline{u}_n\gamma_5 d_{\partial_k}$
8	$\overline{u}_{\partial_k} d_w - \overline{u}_w d_{\partial_k}$	$\overline{u}_{\partial_k}\gamma_5 d_w + \overline{u}_w\gamma_5 d_{\partial_k}$	$\overline{u}_{\partial_k}\gamma_5 d_w - \overline{u}_w\gamma_5 d_{\partial_k}$
9	$\overline{u}_{\partial_k}\gamma_4 d_n + \overline{u}_n\gamma_4 d_{\partial_k}$	$\overline{u}_{\partial_k}\gamma_4\gamma_5 d_n + \overline{u}_n\gamma_4\gamma_5 d_{\partial_k}$	$\overline{u}_{\partial_k}\gamma_4\gamma_5 d_n - \overline{u}_n\gamma_4\gamma_5 d_{\partial_k}$
10	$\overline{u}_{\partial_k}\gamma_4 d_w + \overline{u}_w\gamma_4 d_{\partial_k}$	$\overline{u}_{\partial_k}\gamma_4\gamma_5 d_w + \overline{u}_w\gamma_4\gamma_5 d_{\partial_k}$	$\overline{u}_{\partial_k}\gamma_4\gamma_5 d_w - \overline{u}_w\gamma_4\gamma_5 d_{\partial_k}$
11	$\overline{u}_{\partial_i}\gamma_k d_{\partial_i}$	$\overline{u}_{\partial_i}\gamma_k\gamma_5 d_{\partial_i}$	
12	$\overline{u}_{\partial_i}\gamma_k\gamma_4 d_{\partial_i}$		$\overline{u}_{\partial_i}\gamma_k\gamma_4\gamma_5 d_{\partial_i}$
13	$\epsilon_{ijk}\,(\overline{u}_{\partial_k}\gamma_j\gamma_5 d_n - \overline{u}_n\gamma_j\gamma_5 d_{\partial_k})$	$\epsilon_{ijk}\,(\overline{u}_{\partial_k}\gamma_j d_n - \overline{u}_n\gamma_j d_{\partial_k})$	
14	$\epsilon_{ijk}\,(\overline{u}_{\partial_k}\gamma_j\gamma_5 d_w - \overline{u}_w\gamma_j\gamma_5 d_{\partial_k})$	$\epsilon_{ijk}\,(\overline{u}_{\partial_k}\gamma_j d_w - \overline{u}_w\gamma_j d_{\partial_k})$	
15		$\epsilon_{ijk}\,(\overline{u}_{\partial_k}\gamma_j\gamma_4 d_n - \overline{u}_n\gamma_j\gamma_4 d_{\partial_k})$	
16		$\epsilon_{ijk}\,(\overline{u}_{\partial_k}\gamma_j\gamma_4 d_w - \overline{u}_w\gamma_j\gamma_4 d_{\partial_k})$	

Table A.2: List of spin 1 meson interpolators in the T_1 representation. The numbers in the first column together with the quantum numbers IJ^{PC} label the interpolators uniquely. For the vector and pseudovector channels the index k can have values $k = 1, 2, 3$.

Number	2^{--}	2^{-+}	2^{++}
1	$\lvert\epsilon_{ijk}\rvert\overline{u}_{\partial_k}\gamma_j\gamma_5 d_n$	$\lvert\epsilon_{ijk}\rvert\overline{u}_{\partial_k}\gamma_j\gamma_4\gamma_5 d_n$	$\lvert\epsilon_{ijk}\rvert\overline{u}_{\partial_k}\gamma_j d_n$
2	$\lvert\epsilon_{ijk}\rvert\overline{u}_{\partial_k}\gamma_j\gamma_5 d_w$	$\lvert\epsilon_{ijk}\rvert\overline{u}_{\partial_k}\gamma_j\gamma_4\gamma_5 d_w$	$\lvert\epsilon_{ijk}\rvert\overline{u}_{\partial_k}\gamma_j d_w$
3			$\lvert\epsilon_{ijk}\rvert\overline{u}_{\partial_k}\gamma_j\gamma_4 d_n$
4			$\lvert\epsilon_{ijk}\rvert\overline{u}_{\partial_k}\gamma_j\gamma_4 d_w$

Table A.3: Interpolators for spin 2 mesons belonging to the T_2 irreducible representation of the octahedral group. Repeated indices are summed over. We omit the symmetrization here but a symmetrization similar to the spin 0 and spin 1 cases is also performed.

Number	2^{--}	2^{-+}	2^{++}
1	$Q_{ijk}\overline{u}_{\partial_k}\gamma_j\gamma_5 d_n$	$Q_{ijk}\overline{u}_{\partial_k}\gamma_j\gamma_t\gamma_5 d_n$	$Q_{ijk}\overline{u}_{\partial_k}\gamma_j d_n$
2	$Q_{ijk}\overline{u}_{\partial_k}\gamma_j\gamma_5 d_w$	$Q_{ijk}\overline{u}_{\partial_k}\gamma_j\gamma_t\gamma_5 d_w$	$Q_{ijk}\overline{u}_{\partial_k}\gamma_j d_w$
3		$Q_{ijk}\overline{u}_{\partial_j}\gamma_5 d_{\partial_k}$	$Q_{ijk}\overline{u}_{\partial_k}\gamma_j\gamma_4 d_n$
4		$Q_{ijk}\overline{u}_{\partial_j}\gamma_4\gamma_5 d_{\partial_k}$	$Q_{ijk}\overline{u}_{\partial_k}\gamma_j\gamma_4 d_w$
5			$Q_{ijk}\overline{u}_{\partial_j} d_{\partial_k}$

Table A.4: Interpolators for spin 2 mesons belonging to the E irreducible representation of the octahedral group. Repeated indices are summed over. Again, a symmetrization of the interpolators as described in the text is implied for equal quark masses.

Number	0^{--}	1^{-+}	2^{+-}
1	$\overline{u}_{\partial_k}\gamma_i\gamma_4\ d_n$	$\overline{u}_{\partial_k}\gamma_t d_n$	$Q_{ijk}\overline{u}_{\partial_j}\gamma_t d_{\partial_k}$
2	$\overline{u}_{\partial_k}\gamma_i\gamma_4\ d_w$	$\overline{u}_{\partial_k}\gamma_t d_w$	
3		$\epsilon_{ijk}\overline{u}_{\partial_k}\gamma_j\gamma_t\gamma_5 d_n$	
4		$\epsilon_{ijk}\overline{u}_{\partial_k}\gamma_j\gamma_t\gamma_5 d_w$	

Table A.5: Interpolators with derivatives whose lowest contributing quantum numbers are exotic. We list those lowest quantum numbers only. The interpolator for the 2^{+-} exotics belongs to the E representation. Repeated indices are summed over. The symmetrization has been omitted for clarity.

Appendix B

Correlators for charmonium spectroscopy

In this section, we provide some details about the basis of interpolators used in Chapter 5. As parameters σ and N for the Gaussian smearing of Equation 5.1 we chose $\sigma = 2.2a$ and 20 smearing steps. For the derivative sources, we implemented a general n-point form and experimented with different possibilities. In the end we opted for a derivative using a split of two lattice points (in each direction) instead of just a single site displacement. For both smearing types, we tested several combinations of parameters on a small number of configurations. While different smearing parameters for different sources may be slightly better, we opted for a compromise, thereby cutting down on computer time for the calculations. When extending these calculations to several lattice spacings, we will keep the physical extent of our sources constant. To achieve that, we will have to scale up the number of smearing steps needed for the Gaussian smearing and we will have to use a larger displacement for the derivatives. Notice that, in addition to the quark smearing, we apply 15 steps of 3D APE-smearing with a staple weight of 0.1 to the gauge links used to construct the quark sources.

In the following, we list tables of interpolators for each irreducible representation. The smearing types ∇_i, $\mathbb{D}$ and $\mathbb{B}$ are defined in Equation 5.4. The names of the interpolators in the tables are also used for the figures in Chapter 5.

J^{--}	J^{+-}	J^{-+}	J^{++}
$\gamma_5\gamma_i\nabla_i$	$\gamma_5\gamma_i\mathbb{B}_i$	γ_5	$\mathbb{1}$
	γ_t	$\gamma_t\gamma_5$	$\gamma_i\nabla_i$
		$\gamma_t\gamma_5\gamma_i\nabla_i$	$\gamma_t\gamma_i\nabla_i$
		$\gamma_i\mathbb{B}_i$	$\gamma_t\gamma_5\gamma_i\mathbb{B}_i$
		$\gamma_t\gamma_i\mathbb{B}_i$	

Table B.1: Interpolators belonging to the A_1 representation containing $J = 0, 4, \ldots$. Repeated indices are summed over. Interpolators without derivatives are used with both point and Gaussian sources and sinks.

J^{--}	J^{+-}	J^{-+}	J^{++}
γ_i	$\gamma_t\gamma_5\gamma_i$	$\gamma_t\nabla_i$	$\gamma_5\gamma_i$
$\gamma_t\gamma_i$	$\gamma_5\nabla_i$	$\varepsilon_{ijk}\gamma_t\gamma_5\gamma_j\nabla_k$	$\varepsilon_{ijk}\gamma_j\nabla_k$
∇_i	$\gamma_t\gamma_5\nabla_i$	$\varepsilon_{ijk}\gamma_j\mathbb{B}_k$	$\varepsilon_{ijk}\gamma_t\gamma_j\nabla_k$
$\varepsilon_{ijk}\gamma_5\gamma_j\nabla_k$	$\lvert\varepsilon_{ijk}\rvert\gamma_t\gamma_5\gamma_j\mathbb{D}_k$	$\varepsilon_{ijk}\gamma_t\gamma_j\mathbb{B}_k$	$\lvert\varepsilon_{ijk}\rvert\gamma_5\gamma_j\mathbb{D}_k$
$\lvert\varepsilon_{ijk}\rvert\gamma_j\mathbb{D}_k$	$\mathbb{B}_i$		$\gamma_t\mathbb{B}_i$
$\lvert\varepsilon_{ijk}\rvert\gamma_t\gamma_j\mathbb{D}_k$	$\varepsilon_{ijk}\gamma_5\gamma_j\mathbb{B}_k$		$\varepsilon_{ijk}\gamma_t\gamma_5\gamma_j\mathbb{B}_k$
$\gamma_5\mathbb{B}_i$			
$\gamma_t\gamma_5\mathbb{B}_i$			

Table B.2: Interpolators belonging to the T_1 representation containing $J = 1, 3, 4, 5, \ldots$. Repeated indices are summed over. Interpolators without derivatives are used with both point and Gaussian sources and sinks.

J^{--}	J^{+-}	J^{-+}	J^{++}
$\lvert\varepsilon_{ijk}\rvert\gamma_5\gamma_j\nabla_k$	$\gamma_t\mathbb{D}_i$	$\lvert\varepsilon_{ijk}\rvert\gamma_t\gamma_5\gamma_j\nabla_k$	$\lvert\varepsilon_{ijk}\rvert\gamma_j\nabla_k$
$\gamma_5\gamma_j\mathbb{A}$	$\lvert\varepsilon_{ijk}\rvert\gamma_5\gamma_j\mathbb{B}_k$	$\gamma_5\mathbb{D}_i$	$\lvert\varepsilon_{ijk}\rvert\gamma_t\gamma_j\nabla_k$
		$\gamma_t\gamma_5\mathbb{D}_i$	$\mathbb{D}_i$
		$\lvert\varepsilon_{ijk}\rvert\gamma_j\mathbb{B}_k$	$\lvert\varepsilon_{ijk}\rvert\gamma_t\gamma_5\gamma_j\mathbb{B}_k$
		$\lvert\varepsilon_{ijk}\rvert\gamma_t\gamma_j\mathbb{B}_k$	$\gamma_i\mathbb{A}$
		$\gamma_t\gamma_5\gamma_i\mathbb{A}$	$\gamma_t\gamma_i\mathbb{A}$

Table B.3: Interpolators belonging to the T_2 representation containing $J = 2, 3, 4, 5, \ldots$. Repeated indices are summed over.

J^{--}	J^{+-}	J^{-+}	J^{++}
$Q_{ijk}\gamma_5\gamma_j\nabla_k$	$Q_{ijk}\gamma_t\gamma_5\gamma_j\mathbb{D}_k$	$Q_{ijk}\gamma_t\gamma_5\gamma_j\nabla_k$	$Q_{ijk}\gamma_j\nabla_k$
$Q_{ijk}\gamma_j\mathbb{D}_k$	$Q_{ijk}\gamma_5\gamma_j\mathbb{B}_k$	$Q_{ijk}\gamma_j\mathbb{B}_k$	$Q_{ijk}\gamma_t\gamma_j\nabla_k$
$Q_{ijk}\gamma_t\gamma_j\mathbb{D}_k$		$Q_{ijk}\gamma_t\gamma_j\mathbb{B}_k$	$Q_{ijk}\gamma_5\gamma_j\mathbb{D}_k$
			$Q_{ijk}\gamma_t\gamma_5\gamma_j\mathbb{B}_k$

Table B.4: Interpolators belonging to the E representation containing $J = 2, 4, 5, \ldots$. Repeated indices are summed over.

J^{--}	J^{+-}	J^{-+}	J^{++}
$\gamma_i \mathbb{D}_i$	$\gamma_t\gamma_5\gamma_i \mathbb{D}_i$	$\gamma_t \mathbb{A}$	$\gamma_5\gamma_i \mathbb{D}_i$
$\gamma_t\gamma_i \mathbb{D}_i$	$\gamma_5 \mathbb{A}$		
$\mathbb{A}$	$\gamma_t\gamma_5 \mathbb{A}$		

Table B.5: Interpolators belonging to the A_2 representation containing $J = 3, 6, \ldots$. Repeated indices are summed over.

Appendix C

Parameters for the dynamical CI runs

Here we present the relevant parameters for the dynamical CI runs on which all observables have been determined. For a table of CI coefficients for dynamical simulations, please refer to the appendix of reference [5]. Table C.1 lists the lattice spacing a as well as the quark mass[1] m_{AWI} and the pseudoscalar meson mass for each run. Notice that the lattice spacing for our ensemble with the lightest pion mass is roughly 4% smaller than for the other two runs, resulting in a spatial volume which is close to 2.3 fm.

Run	a [fm]	$a/r_{0,\mathrm{exp}}$	$a\,m_{AWI}$	m_{AWI} [MeV]	m_π [MeV]
A	0.1507(17)	0.3139(35)	0.0327(3)	42.8(4)	525(7)
B	0.1500(12)	0.3126(24)	0.0259(2)	34.1(2)	470(4)
C	0.1440(12)	0.3000(24)	0.0111(2)	15.3(4)	322(5)

Table C.1: Run parameters for dynamical CI runs on a $16^3 \times 32$ lattice.

Run	κ_n	N_n	κ_w	N_w
A	0.212	17	0.184	63
B	0.222	15	0.184	68
C	0.223	15	0.184	70

Table C.2: Smearing parameters for dynamical CI runs A-C. Indices n and w stand for narrow and wide Gaussians. Parameters were chosen to keep the width of the Gaussians approximately constant (in physical units) between different runs.

Table C.2 lists the smearing parameters κ and N used for the Gaussian quark sources introduced in 3.6.2. The derivative sources and sinks are always created on top of the Gaussian wide sources, which have been tuned to double the width of the narrow sources (for runs A-C). The gauge links for the creation of the quark sources are obtained from the original gauge links[2] by applying three levels of 3D HYP smearing with parameters

[1] Calculated from the axial ward identity, see [5].

[2] Our Dirac operator contains one level of stout smearing which is always applied.

$\alpha_1 = 0.8$ and $\alpha_2 = 0.4$. The values have been chosen as a compromise between parameters which maximize the average plaquette and parameters which maximize the minimal plaquettes.

Appendix D

Sequential sources for baryon axial charges

For the calculation of baryon three-point functions, a large number of sequential propagators [158] have to be calculated. Making use of Krylov space solvers for multiple right-hand sides which use information about the lowest eigenpairs to accelerate the convergence of subsequent right-hand sides (for *Deflation algorithms* working directly with the non-hermitian Dirac matrix D see [174, 175, 176]) is most useful for such a calculation.

In this appendix, we present some results obtained with our own implementation of the incremental EigCG solver suggested by Stathopoulos and Orginos [108]. The strength of the algorithm is that it gathers and consecutively improves information about the lowest eigenpairs while solving linear systems. This information is used to deflate all subsequent systems, resulting in large speedups for the Conjugate Gradient (CG) used in the algorithm. The authors of [108] report overall speedups of 4 or more when comparing the EigCG algorithm to a traditional CG.

In the following, we present some plots that show the performance of the algorithm in a practical application, namely the calculation of sequential quark sources needed to determine baryon axial charges. We compare the performance to both a simple CG and to the BiCGStabM algorithm [177]. The latter is used for the calculation of source-to-all propagators which are used in the determination of hadron masses in Chapters 4 and 6.

EigCG is based on a Conjugate Gradient. Therefore, we work with the hermitian positive definite matrix A instead of the Dirac matrix D. We would like to gather eigenpairs

$$\begin{aligned} AV &= \Lambda V \ , \\ A &= D^\dagger D \ , \end{aligned}$$

of this matrix. These eigenpairs are then used to accelerate the convergence for subsequent systems by using

$$x_{0,i} = V\Lambda^{-1}V^\dagger b_i \ , \tag{D.1}$$

as an initial guess (this part is known as InitCG). After a certain number of initial iterations the convergence will not improve significantly anymore. At this point the EigCG part of the algorithm is exchanged for a mixed precision CG.

Figure D.1 shows how eigenvector deflation improves the convergence of subsequent systems already while incrementally improving and expanding the number of eigenpairs

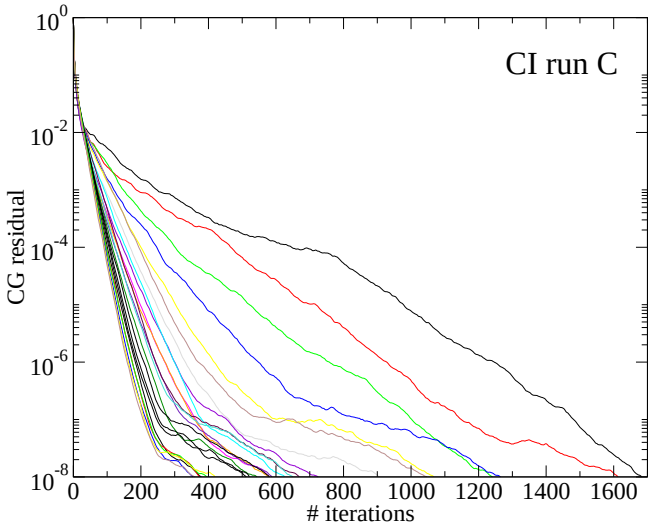

Figure D.1: Solving the 24 first right-hand-sides using the EigCG-algorithm [108] for an example configuration of Run C. Significant speedups can be observed compared to the first system, which is representative for the behavior using a simple CG algorithm.

gathered. In Figure D.2, the accuracy of the lowest 200 eigenpairs after solving 24 linear systems is shown for all three runs.

We now compare the performance of EigCG with subsequent mixed-precision[1] InitCG to the performance of inverters used for other CI projects. To obtain comparable data, we use similar conditions for the three cases[2].

	Run A	Run B	Run C
EigCG(10,100)+InitCG	233	240	256
InitCG	208	210	216
CG	706	870	1688
BiCGStabM	187	229	501
Overall speedup compared to CG	3.0	3.6	6.6
Overhead from EigCG routines	1.6%	1.6%	1.3%

Table D.1: Comparison of different inverters for solving 264 (Run A and B) and 288 linear systems respectively. The numbers listed are the average numbers of iterations needed to solve one right-hand side. EigCG(10,100)+InitCG refers to an average of both the initial EigCG and the subsequent InitCG phases. InitCG lists the average number of iterations for the second phase only. For all inverters, two matrix-vector multiplications per iteration are needed. The last row shows the percentage of walltime spent in routines particular to EigCG.

[1] See [53] for a description of a mixed precision inverter with iterative refinement.

[2] In the case of BiCGStabM the final accuracy was slightly lower due to a different stopping criterion. A full comparison would have to include this effect. With the same accuracy the iteration numbers for BiCGStabM would have been a few percent higher.

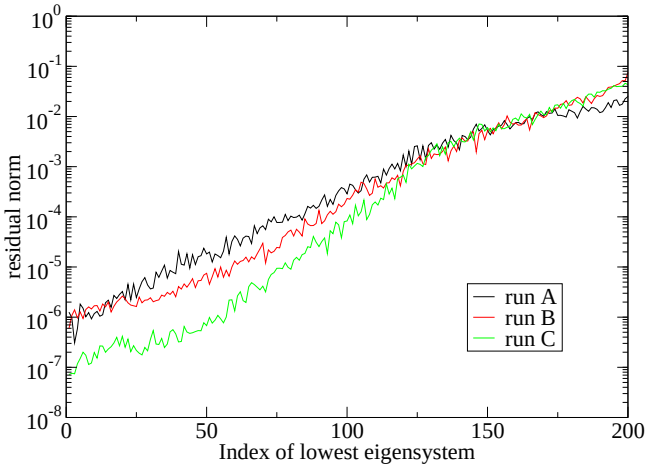

Figure D.2: Residual norm for the 200 lowest eigenpairs after the first 24 right-hand sides have been solved using the EigCG algorithm. Data from all three runs are shown.

Table D.1 shows results for all three runs comparing the performance of EigCG to a conventional CG and to BiCGStabM. Clearly, for the number of right-hand sides considered, EigCG is superior to CG, while the additional overhead from EigCG is completely negligible in our case. Notice that the number of iterations needed to obtain a solution is almost independent of the pion mass in our range of parameters, demonstrating the main advantage of deflation algorithms. Unfortunately, a comparison to the BiCGStabM algorithm is much less favorable in our situation. For run A the number of iterations with a double-precision version of BiCGStabM are even less. We however would like to point out that these numbers can not be directly compared, as we compare the mixed-precision InitCG with the double-precision BiCGStabM and as the desired accuracy has been set slightly different due to a different stopping criterion. The speedup from the use of a mixed precision version compared to a double precision version is roughly 1.5.

Recently, a version of EigCG based on the BiCG algorithm instead of the simple CG has been presented in [176]. As our Dirac operator is γ_5-hermitian, a J-hermitian version of the BiCG algorithm is preferred. For the second phase, the BiCGStab algorithm [178] can be used. While the authors of [176] state that the incremental part does not work quite as well as for the EigCG, the results from EigBiCG+InitBiCGStab are always better than those for the undeflated BiCGStab. This suggests that we could profit from this inverter for runs with a larger pion mass (run A and B). So far, we have not implemented this algorithm.

Acknowledgments

I would like to thank Erek Bilgici, Martina Blank, Tommy Burch, Julia Danzer, Gernot Eichmann, Leonid Glozman, Andreas Krassnigg, Ludmila Levkova, Klaus Lichtenegger, Axel Maas, Kai Schwenzer and Martin Schwinzerl for countless discussions. My special thanks go to Markus Limmer and Georg Engel who worked with me on the dynamical CI project. I am sure I sometimes stressed your patience with yet another silly idea.

Particularly, I would like to express my gratitude to my advisor Prof. Christof Gattringer, whose enthusiasm extended beyond physics and who was able to restore my mood with his optimism whenever I lacked motivation. Equally, I would like to express my gratitude to Prof. Christian B. Lang who answered many of my questions, whether related or unrelated to our projects.

I extent my gratitude to Prof. Carleton DeTar for his hospitality during my research stay at the University of Utah in 2008. He ensured that this visit was very productive and implemented all of our ideas as part of the MILC code suite. Related to this visit, I would also like to thank the members of the MILC Collaboration for their hospitality during their summer meeting.

I would like to thank Sasa Prelovsek for a fruitful collaboration and for sharing many of her ideas with me. I hope to continue these discussions in the future.

I also would like to thank my parents Burgunde Mohler and Gernot Mohler for their enormous support during all these years of studies.

Last but not least, special thanks go to my wife and love Julianna for her continuous support without which I would have lost (the rest) of my sanity. I know you endured a lot during the long time we lived separated and I dedicate this thesis to you.

I also would like to acknowledge financial support by the “Fonds zur Förderung der wissenschaftlichen Forschung in Österreich” (under FWF DK W1203-N08) and by COSY-FFE Projekt 41821486 (COSY-105). The data for the CI projects were generated on computers at the Leibniz Rechenzentrum, Garching and at the ZID, Graz.

Bibliography

[1] C. Michael, *Adjoint sources in lattice gauge theory.*, *Nucl. Phys.* **B259** (1985) 58.

[2] M. Lüscher and U. Wolff, *How to calculate the elastic scattering matrix in two-dimensional quantum field theories by numerical simulation.*, *Nucl. Phys.* **B339** (1990) 222–252.

[3] C. Gattringer, L. Y. Glozman, C. B. Lang, D. Mohler, and S. Prelovsek, *Derivative sources in lattice spectroscopy of excited mesons*, *Phys. Rev.* **D78** (2008) 034501, [arXiv:0802.2020].

[4] C. Gattringer, L. Y. Glozman, C. B. Lang, D. Mohler, and S. Prelovsek, *Meson spectroscopy with derivative quark sources*, *PoS* **LAT2007** (2007) 123, [arXiv:0709.4456].

[5] C. Gattringer *et al.*, *Hadron Spectroscopy with Dynamical Chirally Improved Fermions*, *Phys. Rev.* **D79** (2009) 054501, [arXiv:0812.1681].

[6] R. Frigori *et al.*, *Dynamical Chirally Improved Quarks: First Results for Hadron Masses*, *PoS* **LAT2007** (2007) 114, [arXiv:0709.4582].

[7] C. Gattringer *et al.*, *Spectroscopy with dynamical Chirally Improved quarks*, *PoS* **LATTICE2008** (2008) 093, [arXiv:0809.4514].

[8] Engel, Georg and Gattringer, Christof and Lang, Christian B. and Limmer, Markus and Schäfer, Andreas, *Excited hadrons in $n_f = 2$ QCD*, *PoS* **LATTICE2009** (2009) 088. To be published.

[9] S. Prelovsek and D. Mohler, *A lattice study of light scalar tetraquarks*, *Phys. Rev.* **D79** (2009) 014503, [arXiv:0810.1759].

[10] Engel, Georg and Gattringer, Christof and Glozman, L. Ya. and Lang, Christian B. and Limmer, Markus and Schäfer, Andreas, *Baryon axial charges from chirally improved fermions - first results*, *PoS* **LATTICE2009** (2009) 135. To be published.

[11] K. G. Wilson, *CONFINEMENT OF QUARKS*, *Phys. Rev.* **D10** (1974) 2445–2459.

[12] K. Jansen, *Lattice QCD: a critical status report*, *PoS* **LATTICE2008** (2008) 010, [arXiv:0810.5634].

[13] **PACS-CS** Collaboration, S. Aoki *et al.*, *2+1 Flavor Lattice QCD toward the Physical Point*, arXiv:0807.1661.

[14] Dürr, S. and others, *Ab Initio Determination of Light Hadron Masses*, *Science* **322** (2008) 1224–1227, [arXiv:0906.3599].

[15] **Particle Data Group** Collaboration, C. Amsler *et al.*, *Review of particle physics*, *Phys. Lett.* **B667** (2008) 1.

[16] S. Duane, A. D. Kennedy, B. J. Pendleton, and D. Roweth, *Hybrid Monte Carlo*, *Phys. Lett.* **B195** (1987) 216–222.

[17] V. Kiselev, Y. Shnir, and A. Tregubovich, *Introduction to Quantum Field Theory*. Crc Pr Inc, 2000.

[18] C. Gattringer and C. B. Lang, *Quantum Chromodynamics on the Lattice - an Introductory Presentation*. Springer-Verlag Berlin, Heidelberg, New York, 2009.

[19] Lüscher, M. and Weisz, P., *Computation of the Action for On-Shell Improved Lattice Gauge Theories at Weak Coupling*, *Phys. Lett.* **B158** (1985) 250.

[20] M. Lüscher and P. Weisz, *On-shell improved lattice gauge theories*, *Commun. Math. Phys.* **97** (1985) 59.

[21] H. B. Nielsen and M. Ninomiya, *Absence of Neutrinos on a Lattice. 1. Proof by Homotopy Theory*, *Nucl. Phys.* **B185** (1981) 20.

[22] H. B. Nielsen and M. Ninomiya, *Absence of Neutrinos on a Lattice. 2. Intuitive Topological Proof*, *Nucl. Phys.* **B193** (1981) 173.

[23] P. H. Ginsparg and K. G. Wilson, *A Remnant of Chiral Symmetry on the Lattice*, *Phys. Rev.* **D25** (1982) 2649.

[24] Lüscher, Martin, *Exact chiral symmetry on the lattice and the Ginsparg- Wilson relation*, *Phys. Lett.* **B428** (1998) 342–345, [hep-lat/9802011].

[25] D. B. Kaplan, *A Method for simulating chiral fermions on the lattice*, *Phys. Lett.* **B288** (1992) 342–347, [hep-lat/9206013].

[26] V. Furman and Y. Shamir, *Axial symmetries in lattice QCD with Kaplan fermions*, *Nucl. Phys.* **B439** (1995) 54–78, [hep-lat/9405004].

[27] **RBC-UKQCD** Collaboration, C. Allton *et al.*, *Physical Results from 2+1 Flavor Domain Wall QCD and SU(2) Chiral Perturbation Theory*, *Phys. Rev.* **D78** (2008) 114509, [arXiv:0804.0473].

[28] P. Hasenfratz and F. Niedermayer, *Perfect lattice action for asymptotically free theories*, *Nucl. Phys.* **B414** (1994) 785–814, [hep-lat/9308004].

[29] P. Hasenfratz *et al.*, *Progress using generalized lattice Dirac operators to parametrize the fixed-point QCD action*, *Nucl. Phys. Proc. Suppl.* **94** (2001) 627–635, [hep-lat/0010061].

[30] **BGR** Collaboration, C. Gattringer *et al.*, *Quenched spectroscopy with fixed-point and chirally improved fermions*, *Nucl. Phys.* **B677** (2004) 3–51, [hep-lat/0307013].

[31] H. Neuberger, *Exactly massless quarks on the lattice*, *Phys. Lett.* **B417** (1998) 141–144, [hep-lat/9707022].

[32] H. Neuberger, *More about exactly massless quarks on the lattice*, *Phys. Lett.* **B427** (1998) 353–355, [hep-lat/9801031].

[33] R. G. Edwards, U. M. Heller, and R. Narayanan, *A study of chiral symmetry in quenched QCD using the overlap-Dirac operator*, *Phys. Rev.* **D59** (1999) 094510, [hep-lat/9811030].

[34] N. Cundy, *New solutions to the Ginsparg-Wilson equation*, *Nucl. Phys.* **B802** (2008) 92–105, [arXiv:0802.0170].

[35] **JLQCD** Collaboration, T. Kaneko *et al.*, *JLQCD's dynamical overlap project*, *PoS* **LAT2006** (2006) 054, [hep-lat/0610036].

[36] **JLQCD** Collaboration, H. Matsufuru *et al.*, *Improvement of algorithms for dynamical overlap fermions*, *PoS* **LAT2006** (2006) 031, [hep-lat/0610026].

[37] **JLQCD** Collaboration, S. Aoki *et al.*, *Two-flavor QCD simulation with exact chiral symmetry*, *Phys. Rev.* **D78** (2008) 014508, [arXiv:0803.3197].

[38] N. Cundy, *Current status of dynamical overlap project*, *Nucl. Phys. Proc. Suppl.* **153** (2006) 54–61, [hep-lat/0511047].

[39] N. Cundy *et al.*, *Numerical methods for the QCD overlap operator. IV: Hybrid Monte Carlo*, *Comput. Phys. Commun.* **180** (2009) 26–54, [hep-lat/0502007].

[40] Cundy, Nigel and Krieg, Stefan and Lippert, Thomas and Schäfer, Andreas, *Dynamical overlap fermions with increased topological tunnelling*, *PoS* **LAT2007** (2007) 030, [arXiv:0710.1785].

[41] Cundy, Nigel and Krieg, Stefan and Lippert, Thomas and Schäfer, Andreas, *Topological tunneling with Dynamical overlap fermions*, *Comput. Phys. Commun.* **180** (2009) 201–208, [arXiv:0803.0294].

[42] T. A. DeGrand and S. Schaefer, *Physics issues in simulations with dynamical overlap fermions*, *Phys. Rev.* **D71** (2005) 034507, [hep-lat/0412005].

[43] T. A. DeGrand and S. Schaefer, *Chiral properties of two-flavor QCD in small volume and at large lattice spacing*, *Phys. Rev.* **D72** (2005) 054503, [hep-lat/0506021].

[44] Z. Fodor, S. D. Katz, and K. K. Szabo, *Dynamical overlap fermions, results with HMC algorithm*, *Nucl. Phys. Proc. Suppl.* **140** (2005) 704–706, [hep-lat/0409070].

[45] G. I. Egri, Z. Fodor, S. D. Katz, and K. K. Szabo, *Topology with dynamical overlap fermions*, *JHEP* **01** (2006) 049, [hep-lat/0510117].

[46] C. Gattringer, *A new approach to ginsparg-wilson fermions*, *Phys. Rev.* **D63** (2001) 114501, [hep-lat/0003005].

[47] C. Gattringer, I. Hip, and C. B. Lang, *Approximate ginsparg-wilson fermions: A first test*, *Nucl. Phys.* **B597** (2001) 451–474, [hep-lat/0007042].

[48] D. H. Weingarten and D. N. Petcher, *Monte Carlo Integration for Lattice Gauge Theories with Fermions*, *Phys. Lett.* **B99** (1981) 333.

[49] S. A. Gottlieb, W. Liu, D. Toussaint, R. L. Renken, and R. L. Sugar, *Hybrid Molecular Dynamics Algorithms for the Numerical Simulation of Quantum Chromodynamics*, *Phys. Rev.* **D35** (1987) 2531–2542.

[50] W. Ortner, *Dynamical Chirally Improved Fermions in Lattice QCD*. PhD thesis, Karl-Franzens-Universität Graz, 2006.

[51] M. Hasenbusch, *Speeding up the Hybrid-Monte-Carlo algorithm for dynamical fermions*, *Phys. Lett.* **B519** (2001) 177–182, [hep-lat/0107019].

[52] R. C. Brower, T. Ivanenko, A. R. Levi, and K. N. Orginos, *Chronological inversion method for the Dirac matrix in hybrid Monte Carlo*, *Nucl. Phys.* **B484** (1997) 353–374, [hep-lat/9509012].

[53] Dürr, S. and others, *Scaling study of dynamical smeared-link clover fermions*, *Phys. Rev.* **D79** (2009) 014501, [arXiv:0802.2706].

[54] I. P. Omelyan, I. M. Mryglod, and R. Folk *Comput. Phys. Commun.* **151** (2003) 272.

[55] J. C. Sexton and D. H. Weingarten, *Hamiltonian evolution for the hybrid Monte Carlo algorithm*, *Nucl. Phys.* **B380** (1992) 665–678.

[56] K. Jansen, A. Shindler, C. Urbach, and U. Wenger, *HMC algorithm with multiple time scale integration and mass preconditioning*, *PoS* **LAT2005** (2006) 118, [hep-lat/0510064].

[57] Lüscher, M., *Volume Dependence of the Energy Spectrum in Massive Quantum Field Theories. 1. Stable Particle States*, *Commun. Math. Phys.* **104** (1986) 177.

[58] Lüscher, Martin, *Two particle states on a torus and their relation to the scattering matrix*, *Nucl. Phys.* **B354** (1991) 531–578.

[59] Lüscher, Martin, *Signatures of unstable particles in finite volume*, *Nucl. Phys.* **B364** (1991) 237–254.

[60] Colangelo, Gilberto and Dürr, Stephan and Haefeli, Christoph, *Finite volume effects for meson masses and decay constants*, *Nucl. Phys.* **B721** (2005) 136–174, [hep-lat/0503014].

[61] M. Gell-Mann, R. J. Oakes, and B. Renner, *Behavior of current divergences under SU(3) x SU(3)*, *Phys. Rev.* **175** (1968) 2195–2199.

[62] A. Hasenfratz, R. Hoffmann, and S. Schaefer, *Reweighting towards the chiral limit*, *Phys. Rev.* **D78** (2008) 014515, [arXiv:0805.2369].

[63] J. Gasser and H. Leutwyler, *Chiral Perturbation Theory to One Loop*, *Ann. Phys.* **158** (1984) 142.

[64] J. Gasser and H. Leutwyler, *Chiral Perturbation Theory: Expansions in the Mass of the Strange Quark*, *Nucl. Phys.* **B250** (1985) 465.

[65] **RBC** Collaboration, E. E. Scholz, *Physical results from 2+1 flavor Domain Wall QCD*, *PoS* **LATTICE2008** (2008) 095, [arXiv:0809.3251].

[66] **ETM** Collaboration, P. Boucaud *et al.*, *Dynamical twisted mass fermions with light quarks*, *Phys. Lett.* **B650** (2007) 304–311, [hep-lat/0701012].

[67] **European Twisted Mass** Collaboration, B. Blossier *et al.*, *Light quark masses and pseudoscalar decay constants from Nf=2 Lattice QCD with twisted mass fermions*, *JHEP* **04** (2008) 020, [arXiv:0709.4574].

[68] R. Sommer, *A New way to set the energy scale in lattice gauge theories and its applications to the static force and alpha-s in SU(2) Yang-Mills theory*, *Nucl. Phys.* **B411** (1994) 839–854, [hep-lat/9310022].

[69] C. Aubin *et al.*, *Light hadrons with improved staggered quarks: Approaching the continuum limit*, *Phys. Rev.* **D70** (2004) 094505, [hep-lat/0402030].

[70] M. Asakawa, T. Hatsuda, and Y. Nakahara, *Maximum entropy analysis of the spectral functions in lattice qcd*, *Prog. Part. Nucl. Phys.* **46** (2001) 459–508, [hep-lat/0011040].

[71] K. Sasaki, S. Sasaki, and T. Hatsuda, *Spectral analysis of excited nucleons in lattice QCD with maximum entropy method*, *Phys. Lett.* **B623** (2005) 208–217, [hep-lat/0504020].

[72] H. Suganuma, K. Tsumura, N. Ishii, and F. Okiharu, *Tetra-Quark Resonances in Lattice QCD*, *Prog. Theor. Phys. Suppl.* **168** (2007) 168–172, [arXiv:0707.3309].

[73] M. S. Cook and H. R. Fiebig, *Mass spectrum of 1-+ exotic mesons from lattice QCD*, *Phys. Rev.* **D74** (2006) 094501, [hep-lat/0609010].

[74] Y. Chen *et al.*, *The sequential empirical bayes method: An adaptive constrained-curve fitting algorithm for lattice qcd*, hep-lat/0405001.

[75] N. Mathur *et al.*, *Scalar mesons a0(1450) and sigma(600) from lattice QCD*, *Phys. Rev.* **D76** (2007) 114505, [hep-ph/0607110].

[76] N. Mathur *et al.*, *Roper resonance and S(11)(1535) from lattice QCD*, *Phys. Lett.* **B605** (2005) 137–143, [hep-ph/0306199].

[77] G. Lepage *et al.*, *Constrained curve fitting*, *Nucl. Phys. Proc. Suppl.* **106** (2002) 12–20, [hep-lat/0110175].

[78] G. T. Fleming, *What can lattice qcd theorists learn from nmr spectroscopists?*, in *QCD and numerical Analysis III*, pp. 143–152, 2004. hep-lat/0403023.

[79] H.-W. Lin and S. D. Cohen, *Lattice qcd beyond ground states*, arXiv:0709.1902 [hep-lat].

[80] G. T. Fleming, S. D. Cohen, H.-W. Lin, and V. Pereyra, *Excited-State Effective Masses in Lattice QCD*, arXiv:0903.2314.

[81] G. M. von Hippel, R. Lewis, and R. G. Petry, *Using evolutionary algorithms to extract field theory mass spectra*, *PoS* **LATTICE2007** (2007) 043, [arXiv:0710.0014 [hep-lat]].

[82] R. G. Petry, D. Harnett, R. Lewis, and R. M. Woloshyn, *Exploring the meson spectrum with twisted mass lattice QCD*, arXiv:0803.4141.

[83] **Bern-Graz-Regensburg** Collaboration, T. Burch *et al.*, *Spatially improved operators for excited hadrons on the lattice*, *Phys. Rev.* **D70** (2004) 054502, [hep-lat/0405006].

[84] T. Burch *et al.*, *Excited hadrons on the lattice: Mesons*, *Phys. Rev.* **D73** (2006) 094505, [hep-lat/0601026].

[85] T. Burch *et al.*, *Excited hadrons on the lattice: Baryons*, *Phys. Rev.* **D74** (2006) 014504, [hep-lat/0604019].

[86] J. J. Dudek, R. G. Edwards, N. Mathur, and D. G. Richards, *Charmonium excited state spectrum in lattice QCD*, *Phys. Rev.* **D77** (2008) 034501, [arXiv:0707.4162 [hep-lat]].

[87] S. Basak *et al.*, *Lattice qcd determination of patterns of excited baryon states*, *Phys. Rev.* **D76** (2007) 074504, [arXiv:0709.0008 [hep-lat]].

[88] S. Basak *et al.*, *Lattice QCD determination of states with spin 5/2 or higher in the spectrum of nucleons*, hep-lat/0609052.

[89] A. C. Lichtl, *The Spectral Structure of Correlator Matrices*, *PoS* **LATTICE2007** (2007) 118, [arXiv:0711.4072 [hep-lat]].

[90] J. M. Bulava *et al.*, *Excited State Nucleon Spectrum with Two Flavors of Dynamical Fermions*, *Phys. Rev.* **D79** (2009) 034505, [arXiv:0901.0027].

[91] Burch, Tommy and Hagen, Christian and Lang, Christian B. and Limmer, Markus and Schäfer, Andreas, *Excitations of singly beautiful hadrons*, *Phys. Rev.* **D79** (2009) 014504, [arXiv:0809.1103].

[92] Burch, Tommy and Hagen, Christian and Hetzenegger, Martin and Schäfer, Andreas, *Low and high spin mesons from $N_f = 2$ Clover-Wilson lattices*, *Phys. Rev.* **D79** (2009) 114503, [arXiv:0903.2358].

[93] M. S. Mahbub *et al.*, *Isolating the Roper Resonance in Lattice QCD*, arXiv:0906.5433.

[94] B. Blossier, G. von Hippel, T. Mendes, R. Sommer, and M. Della Morte, *Efficient use of the Generalized Eigenvalue Problem*, *PoS* **LATTICE2008** (2008) 135, [arXiv:0808.1017].

[95] D. Toussaint and W. Freeman, *Sample size effects in multivariate fitting of correlated data*, arXiv:0808.2211.

[96] R. C. Johnson, *ANGULAR MOMENTUM ON A LATTICE*, *Phys. Lett.* **B114** (1982) 147.

[97] **Lattice Hadron Physics (LHPC)** Collaboration, S. Basak *et al.*, *Clebsch-gordan construction of lattice interpolating fields for excited baryons*, *Phys. Rev.* **D72** (2005) 074501, [hep-lat/0508018].

[98] S. Basak *et al.*, *Group-theoretical construction of extended baryon operators in lattice qcd*, *Phys. Rev.* **D72** (2005) 094506, [hep-lat/0506029].

[99] **UKQCD** Collaboration, P. Lacock, C. Michael, P. Boyle, and P. Rowland, *Orbitally excited and hybrid mesons from the lattice*, *Phys. Rev.* **D54** (1996) 6997–7009, [hep-lat/9605025].

[100] S. Güsken *et al.*, *Nonsinglet axial vector couplings of the baryon octet in lattice qcd*, *Phys. Lett.* **B227** (1989) 266.

[101] C. Best *et al.*, *Pion and rho structure functions from lattice qcd*, *Phys. Rev.* **D56** (1997) 2743–2754, [hep-lat/9703014].

[102] X. Liao and T. Manke, *Excited charmonium spectrum from anisotropic lattices*, hep-lat/0210030.

[103] C. Morningstar and M. J. Peardon, *Analytic smearing of SU(3) link variables in lattice QCD*, *Phys. Rev.* **D69** (2004) 054501, [hep-lat/0311018].

[104] A. Hasenfratz and F. Knechtli, *Flavor symmetry and the static potential with hypercubic blocking*, *Phys. Rev.* **D64** (2001) 034504, [hep-lat/0103029].

[105] G. Engel. Private communication.

[106] M. Peardon *et al.*, *A novel quark-field creation operator construction for hadronic physics in lattice QCD*, arXiv:0905.2160.

[107] J. Foley *et al.*, *Practical all-to-all propagators for lattice QCD*, *Comput. Phys. Commun.* **172** (2005) 145–162, [hep-lat/0505023].

[108] A. Stathopoulos and K. Orginos, *Computing and deflating eigenvalues while solving multiple right hand side linear systems in Quantum Chromodynamics*, arXiv:0707.0131.

[109] G. Curci, P. Menotti, and G. Paffuti, *Symanzik's improved lagrangian for lattice gauge theory*, *Phys. Lett.* **B130** (1983) 205. Errata **B135**, 516 (1984).

[110] C. Gattringer, R. Hoffmann, and S. Schaefer, *Setting the scale for the luescher-weisz action*, *Phys. Rev.* **D65** (2002) 094503, [hep-lat/0112024].

[111] W. A. Bardeen, A. Duncan, E. Eichten, N. Isgur, and H. Thacker, *Chiral loops and ghost states in the quenched scalar propagator*, *Phys. Rev.* **D65** (2001) 014509, [hep-lat/0106008].

[112] W. A. Bardeen, E. Eichten, and H. Thacker, *Chiral lagrangian parameters for scalar and pseudoscalar mesons*, *Phys. Rev.* **D69** (2004) 054502, [hep-lat/0307023].

[113] T. Burch, C. Gattringer, L. Y. Glozman, C. Hagen, and C. B. Lang, *Variational method for lattice spectroscopy with ghosts*, *Phys. Rev.* **D73** (2006) 017502, [hep-lat/0511054].

[114] **RBC** Collaboration, S. Prelovsek and K. Orginos, *Quenched scalar meson correlator with domain wall fermions*, *Nucl. Phys. Proc. Suppl.* **119** (2003) 822–824, [hep-lat/0209132].

[115] S. Prelovsek, C. Dawson, T. Izubuchi, K. Orginos, and A. Soni, *Scalar meson in dynamical and partially quenched two-flavor qcd: Lattice results and chiral loops*, *Phys. Rev.* **D70** (2004) 094503, [hep-lat/0407037].

[116] C. McNeile, *Hard hadron spectroscopy*, *PoS* **LATTICE2007** (2007) 019, [arXiv:0710.0985 [hep-lat]].

[117] K. Jansen, C. McNeile, C. Michael, C. Urbach, and f. t. E. Collaboration, *Meson masses and decay constants from unquenched lattice QCD*, arXiv:0906.4720.

[118] W. Detmold, K. Orginos, M. J. Savage, and A. Walker-Loud, *Kaon Condensation with Lattice QCD*, *Phys. Rev.* **D78** (2008) 054514, [arXiv:0807.1856].

[119] **UKQCD** Collaboration, C. McNeile and C. Michael, *Mixing of scalar glueballs and flavour-singlet scalar mesons*, *Phys. Rev.* **D63** (2001) 114503, [hep-lat/0010019].

[120] **UKQCD** Collaboration, C. McNeile and C. Michael, *Properties of light scalar mesons from lattice QCD*, *Phys. Rev.* **D74** (2006) 014508, [hep-lat/0604009].

[121] **UKQCD** Collaboration, A. Hart, C. McNeile, C. Michael, and J. Pickavance, *A lattice study of the masses of singlet 0++ mesons*, *Phys. Rev.* **D74** (2006) 114504, [hep-lat/0608026].

[122] A. Hasenfratz. Private communication.

[123] J. N. Hedditch *et al.*, 1^{-+} *exotic meson at light quark masses*, *Phys. Rev.* **D72** (2005) 114507, [hep-lat/0509106].

[124] P. C. Bruns and U.-G. Meissner, *Infrared regularization for spin-1 fields*, *Eur. Phys. J.* **C40** (2005) 97–119, [hep-ph/0411223].

[125] R. L. Jaffe, *Multi-Quark Hadrons. 1. The Phenomenology of (2 Quark 2 anti-Quark) Mesons*, *Phys. Rev.* **D15** (1977) 267.

[126] R. L. Jaffe, *Multi-Quark Hadrons. 2. Methods*, *Phys. Rev.* **D15** (1977) 281.

[127] M. G. Alford and R. L. Jaffe, *Insight into the Scalar Mesons from a Lattice Calculation*, *Nucl. Phys.* **B578** (2000) 367–382, [hep-lat/0001023].

[128] M. Loan, Z.-H. Luo, and Y. Y. Lam, *Scalar and Vector 4Q Systems in Anisotropic Lattice QCD*, *Eur. Phys. J.* **C57** (2008) 579, [arXiv:0907.3609].

[129] L. Maiani, F. Piccinini, A. D. Polosa, and V. Riquer, *A new look at scalar mesons*, *Phys. Rev. Lett.* **93** (2004) 212002, [hep-ph/0407017].

[130] Prelovsek, Sasa and others, *Spectroscopy of light tetraquark states*, *PoS* **LATTICE2009** (2009). To be published.

[131] C. W. Bernard *et al.*, *The QCD spectrum with three quark flavors*, *Phys. Rev.* **D64** (2001) 054506, [hep-lat/0104002].

[132] A. Bazavov *et al.*, *Full nonperturbative QCD simulations with 2+1 flavors of improved staggered quarks*, arXiv:0903.3598.

[133] A. X. El-Khadra, A. S. Kronfeld, and P. B. Mackenzie, *Massive Fermions in Lattice Gauge Theory*, *Phys. Rev.* **D55** (1997) 3933–3957, [hep-lat/9604004].

[134] M. di Pierro *et al.*, *Properties of charmonium in lattice QCD with 2+1 flavors of improved staggered sea quarks*, *Nucl. Phys. Proc. Suppl.* **129** (2004) 340–342, [hep-lat/0310042].

[135] S. Gottlieb *et al.*, *Onium masses with three flavors of dynamical quarks*, *PoS* **LAT2005** (2006) 203, [hep-lat/0510072].

[136] **Fermilab Lattice and MILC** Collaboration, S. A. Gottlieb *et al.*, *Update on onium masses with three flavors of dynamical quarks*, *PoS* **LAT2006** (2006) 175.

[137] **Fermilab Lattice** Collaboration, C. E. DeTar and L. Levkova, *Effects of the disconnected flavor singlet corrections on the hyperfine splitting in charmonium*, *PoS* **LAT2007** (2007) 116, [arXiv:0710.1322].

[138] L. Levkova and C. E. DeTar, *Contributions of charm anihilation to the hyperfine splitting in charmonium*, *PoS* **LATTICE2008** (2008) 133, [arXiv:0809.5086].

[139] S.-L. Zhu, *New hadron states*, *Int. J. Mod. Phys.* **E17** (2008) 283–322, [hep-ph/0703225].

[140] S. L. Olsen, *What ' s new with the XYZ mesons?*, arXiv:0801.1153.

[141] **CLQCD** Collaboration, Y. Chen, C. Liu, Y. Liu, J. Ma, and J. Zhang, *Radially excited states of 1P charmonium and X(3872)*, hep-lat/0701021.

[142] **TWQCD** Collaboration, T.-W. Chiu and T.-H. Hsieh, *X(3872) in lattice QCD with exact chiral symmetry*, *Phys. Lett.* **B646** (2007) 95–99, [hep-ph/0603207].

[143] **TWQCD** Collaboration, T.-W. Chiu and T.-H. Hsieh, *Y(4260) on the lattice*, *Phys. Rev.* **D73** (2006) 094510, [hep-lat/0512029].

[144] X.-Q. Luo and Y. Liu, *Gluonic excitation of non-exotic hybrid charmonium from lattice QCD*, *Phys. Rev.* **D74** (2006) 034502, [hep-lat/0512044].

[145] C. Ehmann and G. Bali, *Mixing of charmonia with $D\bar{D}$/$c\bar{u}u\bar{c}$ states*, *PoS* **LATTICE2009** (2009). To be published.

[146] A. S. Kronfeld, *Application of heavy-quark effective theory to lattice QCD. I: Power corrections*, *Phys. Rev.* **D62** (2000) 014505, [hep-lat/0002008].

[147] **HPQCD** Collaboration, E. Follana *et al.*, *Highly Improved Staggered Quarks on the Lattice, with Applications to Charm Physics*, *Phys. Rev.* **D75** (2007) 054502, [hep-lat/0610092].

[148] S. Tamhankar *et al.*, *Charmonium spectrum from quenched QCD with overlap fermions*, *Phys. Lett.* **B638** (2006) 55–60, [hep-lat/0507027].

[149] C. Ehmann and G. Bali, *Charmonium spectrum including higher spin and exotic states*, *PoS* **LAT2007** (2007) 094, [arXiv:0710.0256].

[150] M. B. Oktay and A. S. Kronfeld, *New lattice action for heavy quarks*, *Phys. Rev.* **D78** (2008) 014504, [arXiv:0803.0523].

[151] **Bern-Graz-Regensburg** Collaboration, Brömmel, Dirk and others, *Low lying nucleons from chirally improved fermions*, *Nucl. Phys. Proc. Suppl.* **129** (2004) 251–253, [hep-lat/0309036].

[152] A. Walker-Loud *et al.*, *Light hadron spectroscopy using domain wall valence quarks on an Asqtad sea*, arXiv:0806.4549.

[153] A. Walker-Loud, *New lessons from the nucleon mass, lattice QCD and heavy baryon chiral perturbation theory*, arXiv:0810.0663.

[154] T. T. Takahashi and T. Kunihiro, *Axial charge of N(1535) in lattice QCD with two flavors of dynamical quarks*, *Phys. Rev.* **D78** (2008) 011503, [arXiv:0801.4707].

[155] W. Melnitchouk *et al.*, *Excited baryons in lattice QCD*, *Phys. Rev.* **D67** (2003) 114506, [hep-lat/0202022].

[156] B. G. Lasscock *et al.*, *Even parity excitations of the nucleon in lattice QCD*, *Phys. Rev.* **D76** (2007) 054510, [arXiv:0705.0861].

[157] M. L. Goldberger and S. B. Treiman, *Decay of the pi meson*, *Phys. Rev.* **110** (1958) 1178–1184.

[158] **the RIKEN-BNL-Columbia-KEK** Collaboration, S. Sasaki, K. Orginos, S. Ohta, and T. Blum, *Nucleon axial charge from quenched lattice QCD with domain wall fermions*, *Phys. Rev.* **D68** (2003) 054509, [hep-lat/0306007].

[159] **LHPC** Collaboration, R. G. Edwards *et al.*, *The nucleon axial charge in full lattice QCD*, *Phys. Rev. Lett.* **96** (2006) 052001, [hep-lat/0510062].

[160] S. R. Beane and M. J. Savage, *Baryon axial charge in a finite volume*, *Phys. Rev.* **D70** (2004) 074029, [hep-ph/0404131].

[161] W. Detmold and C. J. D. Lin, *Twist-two matrix elements at finite and infinite volume*, *Phys. Rev.* **D71** (2005) 054510, [hep-lat/0501007].

[162] **RBC+UKQCD** Collaboration, T. Yamazaki *et al.*, *Nucleon axial charge in 2+1 flavor dynamical lattice QCD with domain wall fermions*, *Phys. Rev. Lett.* **100** (2008) 171602, [arXiv:0801.4016].

[163] B. C. Tiburzi, *Time Dependence of Nucleon Correlation Functions in Chiral Perturbation Theory*, *Phys. Rev.* **D80** (2009) 014002, [arXiv:0901.0657].

[164] S. N. Syritsyn *et al.*, *Nucleon Structure with Domain Wall Fermions at a = 0.084 fm*, *PoS* **LATTICE2008** (2008) 169, [arXiv:0903.3063].

[165] D. Renner, *Status and prospects for the calculation of hadron structure from lattice QCD*, *PoS* **LATTICE2009** (2009). To be published.

[166] H.-W. Lin and K. Orginos, *First Calculation of Hyperon Axial Couplings from Lattice QCD*, *Phys. Rev.* **D79** (2009) 034507, [arXiv:0712.1214].

[167] F.-J. Jiang and B. C. Tiburzi, *Chiral Corrections to Hyperon Axial Form Factors*, *Phys. Rev.* **D77** (2008) 094506, [arXiv:0801.2535].

[168] B. C. Tiburzi and A. Walker-Loud, *Hyperons in Two Flavor Chiral Perturbation Theory*, *Phys. Lett.* **B669** (2008) 246–253, [arXiv:0808.0482].

[169] F.-J. Jiang and B. C. Tiburzi, *Hyperon Axial Charges in Two-Flavor Chiral Perturbation Theory*, arXiv:0905.0857.

[170] P. Huber unpublished, 2009.

[171] F.-J. Jiang and B. C. Tiburzi, *Chiral Corrections and the Axial Charge of the Delta*, *Phys. Rev.* **D78** (2008) 017504, [arXiv:0803.3316].

[172] L. Y. Glozman, *Alternative experimental evidence for chiral restoration in excited baryons*, *Phys. Rev. Lett.* **99** (2007) 191602, [arXiv:0706.3288].

[173] C. Alexandrou, G. Koutsou, T. Leontiou, J. W. Negele, and A. Tsapalis, *Axial nucleon and nucleon to Delta form factors and the Goldberger-Treiman relations from lattice QCD*, *Phys. Rev.* **D76** (2007) 094511.

[174] W. Wilcox, *Deflation Methods in Fermion Inverters*, *PoS* **LAT2007** (2007) 025.

[175] A. M. Abdel-Rehim, R. B. Morgan, and W. Wilcox, *Deflated BiCGStab for linear equations in QCD problems*, *PoS* **LAT2007** (2007) 026, [arXiv:0710.1988].

[176] A. M. Abdel-Rehim, A. Stathopoulos, and K. Orginos, *Extending the eigCC algorithm to non-symmetric Lanczos for linear systems with multiple right-hand sides*, Tech. Rep. WM-CS-2009-06, College of William & Mary, 2009.

[177] B. Jegerlehner, *Krylov space solvers for shifted linear systems*, hep-lat/9612014.

[178] H. A. van der Vorst, *BI-CGSTAB: a fast and smoothly converging variant of BI-CG for the solution of nonsymmetric linear systems*, *SIAM J. Sci. Stat. Comput.* **13** (1992), no. 2 631–644.